

Development of three-dimensional physical property imaging
method for layered materials using ultrasound

(超音波を用いた層構造物質の三次元物性量イメージング法の開発)

July, 2021

Doctor of Philosophy (Engineering)

EDO BAGUS PRASTIKA

エド バグス プラスティカ

Toyohashi University of Technology

2021 年 7 月 5 日

Department of Electrical and Electronic Information Engineering 電気・電子情報工学専攻	Student ID 学籍番号	189202
Name 申請者氏名	Edo Bagus Prastika	

Supervisor 指導教員氏名	Naohiro Hozumi 穂積 直裕
----------------------	-------------------------

Abstract
論文要旨(博士)

Title 論文題目	Development of three-dimensional physical property imaging method for layered materials using ultrasound (超音波を用いた層構造物質の三次元物性量イメージング法の開発)
---------------	---

A three-dimensional (3D) physical property imaging using ultrasound is proposed. A focused transducer scans the layered object along x and y direction and the cross-sectional view of the object is obtained. The reflection coefficient is then calculated by deconvoluting all the reflected waveforms. Unlike the conventional B-mode echography where each region (layers) of the object was only indicated by the intensity of the reflected signal (brightness), this study proposes a quantitative observation by converting each time-dependent reflection coefficient into its physical property such as acoustic impedance.

Conventionally, deconvolution is performed by division in frequency domain. However, in practice, the deconvoluted waveform suffers from the instability of baseline. This can be caused by improper spectrum division (noise divided by noise) which will create a spurious in low-frequency components, resulting in a wavy waveform when the result is brought back into time domain. Since the process of acoustic impedance conversion is similar to the integration along time axis, any instability in baseline will lead to the accumulation of error as integration goes deeper, which will appear as an artifact in acoustic impedance image. In addition, as the depth of measurement target gets deeper, the instability in baseline after deconvolution will also become stronger. It can be concluded that deconvolution process becomes an essential aspect in acoustic impedance imaging.

In conjunction with the above problems, this study proposes an improvement in the deconvolution process. Instead of performing deconvolution only in frequency domain, the calculation is also performed in time domain because spectral division is not required and the generation of spurious in low-frequency parts after deconvolution can be avoided. However, since the calculation speed of time domain deconvolution is directly proportional to the number of samples in the waveform, a down-sampling is performed to speed up the calculation process, with the consequence of the waveform having its high-frequency components reduced. The spurious in low-frequency components as the result of frequency domain deconvolution is then replaced by that calculated by time domain deconvolution by specifying a threshold value. This way of calculation will retain the stability of low-frequency components in the spectrum, resulting in a waveform with stable baseline.

The first chapter of this study will discuss about the background and history of microscopic imaging by using ultrasound. The target and motivation as well as the contribution of the thesis will also be described.

The second chapter will discuss about the theoretical preparation of the proposed quantitative acoustic imaging method including the process of acoustic impedance interpretation and the concept of conventional and the proposed time-frequency (dual) domain deconvolution method.

The third chapter will discuss about the application of the proposed signal processing method to human cheek skin observation. As the result, each layer of human cheek skin was visible and could be contrasted by its acoustic parameters, which can be correlated to elasticity.

The fourth chapter will discuss about the requirement to perform a 3D calculation (by performing many times of deconvolution process) so that the calculated acoustic impedance data can be sliced in all cross-sectional direction.

The improvement and optimal condition of dual domain deconvolution when calculating a stack of acoustic impedance images in order to increase the robustness and quickness of the calculation will be discussed. As a result, 3D reconstruction of human cheek skin and a quantitative skin observation based on the difference of ages and its correlation with the generation of wrinkles will be discussed.

The fifth chapter of this study will discuss about the proposed signal processing for observing the dynamism of cultured cells (Glial cells and Fibroblast cells). As a result, the area of culture liquid, cell and substrate could be distinguished based on its acoustic impedance value. In addition, by stacking all the calculated cross-sectional acoustic impedance images, the dynamism of the cell such as the change in height and shape before and after the treatment (fixation by aldehyde) could be tracked.

The sixth chapter of this study will discuss about the application of the proposed acoustic imaging method for coating film monitoring in automotive industry, as an alternative to the conventional observation by using Terahertz light which is expensive. As a result, not only the thickness but the uniformity of each layer could also be assessed by means of its acoustic impedance distribution. In another section of the chapter, the application of the proposed signal processing to the space charge measurement in cross-linked polyethylene (XLPE) cable by using pulsed electro-acoustic (PEA) device will also be discussed. Since the stability of each waveform can be maintained by dual domain deconvolution, the charge intensity, electric field and potential distribution could then be calculated by integrating all the calculated waveform.

It can be concluded that from the above-mentioned applications, the proposed signal processing method is believed to be advantageous and applicable to many ultrasound-based research fields because many of the applications require an integration process along time axis and when stability and quickness of the calculation can be maintained, the analysis result can be interpreted into something more informative and quantitative.

Table of contents

Abstract	i
Table of contents	iii
List of figures	vi
List of tables	ix
Chapter I.....	1
Introduction.....	1
1.1. Background	1
1.2. History of microscopic imaging (by ultrasound microscope)	4
1.3. Types of conventional ultrasound imaging	6
1.4. Recent wideband RF acquisition and imaging	7
1.5. Some industrial applications using acoustic imaging.....	8
1.6. Target of research.....	10
1.7. Motivation and research objective.....	11
1.8. Thesis contributions	12
1.9. Thesis organization.....	13
Chapter II	15
Theoretical Preparation of the Proposed Acoustic Imaging Method	15
2.1. Acoustic impedance interpretation	15
2.2. Elasticity and acoustic impedance.....	17
2.3. Integration along time axis	17
2.4. Frequency domain deconvolution	18
2.5. Time domain deconvolution.....	19
2.6. Time and frequency (dual) domain deconvolution.....	21
Chapter III.....	23
Acoustic Impedance Mapping for Human Cheek Skin Observation	23
3.1. Human cheek skin	23
3.2. Skin property measurement.....	24
3.3. Measurement system	25
3.4. Transducer specification.....	26
3.5. Interpretation into apparent reflection coefficient.....	26
3.6. Acoustic impedance mapping by the proposed dual domain deconvolution	27
3.7. The comparison results between the conventional frequency domain deconvolution and the proposed dual domain deconvolution method	28
3.8. Discussion	30
3.9. Conclusion.....	30
Chapter IV.....	31
Optimal Condition for Dual Domain Calculation (Speed and Preciseness Improvement) Applied to Human Skin Observation	31
4.1. 3D acoustic impedance observation	31
4.2. Down-sampling and its effect to calculation time	32
4.3. Down-sampling and its effect to calculation error	33
4.4. Frequency border of dual domain.....	34

4.5. The appearance of offset in the signal	35
4.6. The comparison of the deconvoluted signal	37
4.7. Kurtosis calculation	38
4.8. 3D skin reconstruction from the calculated acoustic impedance images	41
4.9. The relation between the depth-specific elastic properties and the generation of wrinkles in the skin.....	42
4.10. Discussion	43
4.11. Conclusions	44
Chapter V	45
Precise Cellular-sized Observation by Acoustic Impedance Microscope	45
5.1. Ultrasound imaging for cultured cell observation	45
5.2. The objective of cell observation	46
5.3. System setup.....	47
5.4. Transducer specification.....	48
5.5. Acoustic impedance interpretation	48
5.6. Dual domain deconvolution (cell)	49
5.7. The signal processing result (Glial cell).....	50
5.7.1. Waveform comparison between frequency domain deconvolution and dual domain deconvolution	50
5.7.2. Acoustic impedance comparison between frequency domain deconvolution and dual domain deconvolution.....	51
5.7.3. Analysis of cell structure based on the acoustic impedance image	52
5.8. The signal processing result (Fibroblast cell).....	54
5.8.1. 3D analysis of Fibroblast cell	54
5.8.2. Cell dyeing (staining by DAPI)	56
5.8.3. The change in properties of the cell (height and shape) after some treatment to the cell (fixation).....	58
5.9. Discussion	60
5.9.1. Dual domain deconvolution for cultured cell observation.....	60
5.9.2. 3D analysis and the change in cell properties.....	63
5.10. Conclusion.....	63
5.10.1. Dual domain deconvolution for cultured cell observation.....	63
5.10.2. 3D analysis and the change in cell properties.....	64
Chapter VI.....	65
The Application of Acoustic Property Imaging for Industrial Applications	65
6.1. Coating film monitoring.....	65
6.1.1. System setup	66
6.1.2. Sample	66
6.1.3. Dual domain deconvolution (coating film).....	67
6.1.4. The calculation of time-dependent reflection coefficient	67
6.1.5. The deconvoluted waveform and layers distribution.....	68
6.1.6. Discussion.....	69
6.1.7. Conclusion	69
6.2. Space charge measurement by means of pulse electroacoustic (PEA) method.....	69
6.2.1. System setup	70
6.2.2. Acquired signal.....	71

6.2.3. Dual domain deconvolution (space charge measurement by PEA).....	71
6.2.4. The result of time dependent reflection coefficient by dual domain deconvolution	71
6.2.5. 2D charge distribution along the cable	72
6.2.6. Field analysis	72
6.2.7. Discussion.....	73
6.2.8. Conclusion	73
Chapter VII.....	74
Conclusion and Future Applications	74
7.1. Conclusion.....	74
7.1.1. Acoustic impedance mapping for human cheek skin observation.....	74
7.1.2. Optimal condition for dual domain calculation (speed and preciseness improvement) applied to human skin observation.....	75
7.1.3. Precise cellular-sized observation by acoustic impedance microscope.....	75
7.1.4. The application of the proposed signal processing to other ultrasound-based measurements (industrial applications)	76
7.1.5. Coating film monitoring	76
7.1.6. Space charge measurement by means of pulse electroacoustic (PEA) method.....	77
7.2. Future application.....	77
References	79
Acknowledgement	
List of publications	

List of figures

Figure 1.1. The proposed scanning acoustic microscope system and (b) the acoustic image of polystyrene particles (black bar indicates 100 μm) by Lemons et al in early 1971....	4
Figure 1.2. The acoustic image of binucleate fibroblastic cell (bar indicates 10 μm) by Johnston et al.	5
Figure 1.3. The attenuation and sound speed image by Saijo et al.	5
Figure 1.4. The layout of the proposed system and (b). the acoustic impedance result proposed by Hozumi et al. in 2005.....	5
Figure 1.5. Several types of ultrasound imaging methods and their corresponding frequency for specific imaging applications ⁵²⁾⁻⁵⁵⁾	7
Figure 1.6. The recent application of RF signal acquisition and imaging ^{55),64),65)}	8
Figure 1.7. Localization of fault in semiconductor devices using ultrasound.....	9
Figure 1.8. The measurement setup of space charge measurement in insulation material.....	9
Figure 1.9. Target of quantitative acoustic imaging in this study ^{15),55),70)}	10
Figure 2.1. The process of interpreting each fragment of reflection coefficient into the acoustic impedance.	15
Figure 2.2. The waveform integration and the problem that commonly occur during acoustic impedance interpretation.	18
Figure 2.3. The workflow of frequency domain deconvolution.....	19
Figure 2.4. The generation of transfer matrix from the reference signal.	20
Figure 2.5. The stream of dual domain deconvolution.....	21
Figure 3.1. Layers of the skin ⁷⁴⁾	23
Figure 3.2. The skin measurement by using OCT ⁷⁵⁾	24
Figure 3.3. Elasticity measurement by using cutometer ^{76),77)}	25
Figure 3.4. The measurement system for human cheek skin observation.....	25
Figure 3.5. The properties of the transducer.	26
Figure 3.6. The relation between the target and reference signal.....	26
Figure 3.7. The acoustic impedance distribution of human cheek skin as the result of the proposed time and frequency (dual) domain deconvolution.	28
Figure 3.8. The comparison of the deconvoluted waveform calculated by conventional frequency domain and proposed dual domain deconvolution method.	29
Figure 3.9. The comparison of the cross-sectional acoustic impedance result calculated by conventional frequency domain deconvolution and proposed dual domain deconvolution.	29
Figure 4.1. The skin dataset that is created by stacking all calculated cross-sectional acoustic impedance images.....	31
Figure 4.2. The down-sampling operation and its effect to (a). Calculation time and (b). calculation error.	32
Figure 4.3. The amount of appended low-frequency components into the dual domain calculation.....	34
Figure 4.4. The measurement area of the skin and the existence of offset in the signal.	35
Figure 4.5. The transfer matrix with DC component subjected.	36

Figure 4.6. (Intensity image) The effect of adding a DC component to the result of the deconvoluted waveform.....	37
Figure 4.7. The result of the kurtosis calculation on each deconvoluted waveform.	38
Figure 4.8. The effect of adding DC component and its improvement to the acoustic impedance image.	40
Figure 4.9. (a). The 3D reconstruction of human cheek skin (the shown result was taken from a woman at her 20s); (b). The process of detecting the horny and papillary layer; (c). The horny layer reconstructed from young and old women.....	42
Figure 4.10. The depth of fixed wrinkles correlated with the gap coefficient value ⁷³	42
Figure 5.1. The cross-sectional acoustic impedance image of Glial cell; Hozumi et al.....	46
Figure 5.2. The change in cell after the addition of drug.	46
Figure 5.3. The setup of the system for cultured cell observation.	47
Figure 5.4. (a). Piezo stage for high accuracy scanning and (b). the culture dish.....	47
Figure 5.5. The specification of the transducer.	48
Figure 5.6. The acoustic impedance interpretation when multiple reflections are neglected.	49
Figure 5.7. The comparison of waveforms as the result of both deconvolution methods.....	50
Figure 5.8. The top view of the cell being measured, shown in acoustic impedance and its cross-sectional view on the area sliced by the white cursor.	51
Figure 5.9. The comparison results of the deconvolution and acoustic impedance image. 5.9 (a) and 5.9 (b) are the resulting image from the frequency domain and time-frequency domain deconvolution, respectively. Figure 5.9 (c) and 5.9 (d) are the result of the acoustic impedance image from the frequency domain and time-frequency domain deconvolution, respectively.	51
Figure 5.10. The result of acoustic impedance profile as well as the estimation of the Nucleus position based on the cross-sectional view of the cell by using the frequency domain and time-frequency domain deconvolution.	52
Figure 5.11. The cross-sectional view of the cell 3 sliced at vertical direction and its corresponding result calculated by the fully frequency domain and the time-frequency domain deconvolution.....	53
Figure 5.12. The signal processing result (dual domain deconvolution) of Fibroblast cell.	54
Figure 5.13. Three-dimensional analysis of Fibroblast cell (fresh).....	55
Figure 5.14. Another three-dimensional analysis of Fibroblast cell (fresh).....	55
Figure 5.15. The difference between the cell before and after dyeing process.	56
Figure 5.16. Three-dimensional analysis of Fibroblast cell after staining is performed; The nucleus in light microscope image becomes clearly visible after staining.	57
Figure 5.17. Another three-dimensional analysis of Fibroblast cell (another cell dataset) after staining is performed; The nucleus in the light microscope image becomes clearly visible after staining.....	57
Figure 5.18. The height analysis of the cell calculated from the deconvoluted image.	59
Figure 5.19. The surface graph created from the 2D mapping of the calculated height.	59
Figure 5.20. The change in Fibroblast cell before and after the fixation process in another dataset: (a). Light microscope image and (b). The comparison of cross-sectional acoustic impedance image and its change in shape.	60
Figure 5. 21. The generation of reflection inside the cell.....	61
Figure 5.22. The estimation of dynamic range between the cell and culture liquid.....	62
Figure 6.1. The structure of coating film in car.	65

Figure 6.2.	The coating film assessment by using terahertz light.	65
Figure 6.3.	The system setup of the coating film monitoring.	66
Figure 6.4.	The created sample for the purpose of measurement.....	66
Figure 6.5.	The time dependent reflection coefficient calculated by dual domain deconvolution.	67
Figure 6.6.	The calculated 2D acoustic impedance image of the layers.	68
Figure 6.7.	The measurement system and the PEA measurement cell.....	70
Figure 6.8.	The comparison of the calculated time dependent reflection coefficient.	71
Figure 6.9.	The comparison of the calculated time dependent reflection coefficient.	72
Figure 6.10.	The field calculated by using the result of the proposed method.....	73
Figure 7.1.	The achieved and the future plan of the quantitative acoustic imaging applications ^{89),90)}	78

List of tables

Table 1.1. Several ways of performing non-destructive evaluation and their corresponding characteristics	2
Table 4.1. The calculation time required for each down-sampling level	33
Table 4.2. The kurtosis calculation of 10 different skin datasets with different types of deconvolutions.	39

Chapter I

Introduction

Chapter I will discuss about the background of this research. The chapter starts with the history of ultrasound imaging including its application to observe smaller object (microscopic purpose). In addition, the motivation of the study, the objective of the research and the contribution of the thesis will also be discussed, followed by the thesis organization at the end of the chapter.

1.1. Background

Most of the parts about the history of ultrasound written in this study was taken and revised from some references¹⁾⁻³⁾. The application of ultrasound has covered many aspects in our life. Ultrasound observation for non-destructive inspection has been widely used these days because of its safety (as long as it is used properly), compared with the diagnosis by using X-ray. Table 1.1. shows several ways of performing non-destructive inspection (imaging) using conventional method such as X-ray, optical light, Terahertz, Microwave and ultrasound.




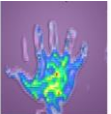

As shown by Table 1.1, X-ray may have a good spatial resolution, however its radiation to biological tissue is destructive so periodical observation is not possible. Optical observation may be safe but it becomes difficult if the target is deep because it requires the light to propagates through the target in order to be visible (transparent). Terahertz (THz) imaging may provide a good spatial resolution, however, some studies showed that Terahertz imaging will cause some changes in DNA^{4),5)}. Microwave imaging, on the other hand, may not cause any change in tissue structure⁶⁾, however, the cost of the hardware may be expensive.

Non-destructive observation by using ultrasound is probably the most flexible among all. Not only that it is practically safe, but the spatial resolution can also be improved by increasing the transducer frequency and performing some modifications in the hardware. In addition, the image can be contrasted by parameters related to the elasticity such as sound speed and acoustic impedance. Several advantages of ultrasound that it is suitable for medical and biological purposes are as follow^{1)-3),7)-10)}:

- a. *Low-risk Radiation.* Ultrasound is considered safe as long as high intensities are not used, which is also becoming the reason why ultrasound medical examination is popular during pregnancy test. The ultrasound observation also allows the repeated examinations of the same patient with minimum risk (according to the declaration and restrictions published by the American Institute for Ultrasound in Medicine (AIUM)).
- b. *High sampling rate.* Since the average speed of sound c in most tissue is approximately 1540 m/s and the common range used in medical examinations is short (0.1 – 25 cm), it required a pretty much short time (microseconds order) to cover that range.
- c. *A single transceiver (transmitter and receiver) transducer can be used.* Because most of ultrasound transducers are compact in shape, a single transducer that can transmit and receive ultrasonic waves can be built. This will increase our flexibility in order to detect many regions.

- d. *Many parameters are measurable.* Since the propagating ultrasound is mainly related to the properties of medium which its travel, many parameters become measurable, such as speed of sound, attenuation, acoustic impedance, dispersion, elasticity, and many more.
- e. *Cheap.* Because of its safety, ultrasound does not require a RF shielded room (such as MRI) or film for imaging (such as X-ray). This makes the observation by using ultrasound is cost-effective.

Table 1.1. Several ways of performing non-destructive evaluation and their corresponding characteristics

	Contrast	Frequency	Spatial resolution	Acquisition	Remarks
X-ray ¹¹⁾ 	<ul style="list-style-type: none"> • Electro-magnetic • Permittivity • Conductivity • Electro-magnetic impedance • Electro-magnetic absorbance 	$> 10^{16} - 10^{20}$ Hz	$< \mu\text{m}$	Spectral	Biologically invasive
Optical ¹²⁾ 		$> 10^{15} - 10^{19}$ Hz	$< \mu\text{m}$		Optical transparency needed. If not, only shallow inspection available
Terahertz (THz) ¹³⁾ 		$> 10^{12}$ Hz	$< \text{mm}$		Long depth of inspection
Microwave ¹⁴⁾ 		$> 10^{10}$ Hz	$< \text{mm}$	Spectral / time domain	Long depth of inspection
Ultrasound ¹⁵⁾ 	<ul style="list-style-type: none"> • Elastic • Sound speed • Acoustic impedance 	40 kHz ~ 1 GHz	$\mu\text{m} \sim \text{mm}$	Spectral / time domain	Large depth Available to optically non-transparent objects

In the past, before many scientists discover the benefit of ultrasound in the field of medicine, most of the application at that time focused on the measurement of speed of sound in water for the purpose of SONAR (*SOund Navigation And Ranging*), started in early 1826 by Jean-Daniel Colladon and Charles Sturm¹⁶⁾. In order to support his data about compressibility of liquids, Colladon determined the speed of sound in water by striking an underwater bell in Lake Geneva and igniting gunpowder. By measuring the interval between these two events from different location at 10 miles away, he calculated the speed of sound in Lake Geneva to be 1435 m/s, which is 3 m/s difference from current calculations¹⁷⁾. Colladon experiment then became the birth of modern acoustic in underwater. Later in 1877, *The Theory of Sound*, which became the

foundation for ultrasound science was published by John William Strutt (or better known as Lord Rayleigh).

In 1880, an important discovery that contributed in the development of ultrasound transducer these days was found by Pierre and Jacques Curie. In their experiment, they found that electric charge was generated when pressure was applied to crystals of quartz. This charge was also directly proportional to the force applied to it. The phenomenon was then called “piezoelectricity”.

In the late 1937, Karl Theodore Dussik who was a psychiatrist and neurologist utilized 1.5 MHz and scanned a human brain. The variations in amplitude of the detected energy were then recorded. The generated images which corresponded to the attenuated area was called “hyper phonograms” and was thought to be the lateral ventricles. By looking at the difference in the wave transmission between normal tissue and tumor, Dussik then stated that the existence of brain tumor may be detected by using ultrasound. However, this statement was then revised by Guttner in 1952 who stated that the images created by Dussik were variations in bone thickness. Following that finding, the United States Atomic Energy Commission reported that ultrasound had no role in detecting the brain tumors⁸⁾.

In 1944, Lynn and Putnam tried to apply the ultrasound in order to test the destruction of brain tissue in animals. They then found that ultrasound caused some tissue damage to the scalp and brain, causing some symptoms such as blindness and death. Other similar studies also caused the destruction in tissue, which then led to the decline of ultrasound application as neurosurgical tool⁸⁾.

The first investigators who report the application of ultrasound (pulse-echo technique) in biological tissue were Ludwig and Struthers. They investigated the speed of sound in beef and extremities of human, which then resulted to the average speed of sound in soft tissue that is around 1540 m/s. They also reported that ultrasound could visualize implanted gallstones in the gallbladders and muscles of dogs. This then became the pioneer for the research conducted by John Julian Wild and Douglas Howry, which then became the most important figures in the history of ultrasound. In 1949, Howry, by working together with W. Roderic Bliss, they build what claimed to be the first B-mode scanner. After several years, Howry attempted to eliminate the extraneous echo and shadows that affect the quality of the ultrasound images. He found that B-mode images only displayed the reflection from the interfaces of tissue that is perpendicular to the ultrasound beam. He also found that highly reflective part in the body such as bone would create shadows that disturbed the deeper structures.

In 1955, Ian Donald, by utilizing A-mode ultrasound machine was able to differentiate various types of tissues in recently excised fibroids and ovarian cysts. In 1958, he then published “Investigation of Abdominal Masses by Pulsed Ultrasound”. Donald contributes in many aspects in ultrasound field, especially in obstetrics and gynecology. He also the first to introduce the biparietal diameter of the fetus and utilized it as an index for the fetal growth, and his contributions were well accepted in the medicine field which then became the pioneer that ultrasound would have a major role in medical diagnostic imaging.

In 1970s and 1980s, the various improvements of ultrasound transducers and machines contributed to the improvement of the ultrasound imaging and helped to expanded the use of the technology. The application of ultrasound for localizing intra-abdominal abscessed was popularized by Leopold and Doust, Kobayashi, Wagai, Cole-Beuglet, Stuber, and Miskin¹⁸⁾¹⁹⁾²⁰⁾²¹⁾. In addition, other division of general surgery such as trauma relied on the

portability of ultrasound for the sake of their patients. In 1971 for the first time, Kristensen reported the application of ultrasound to assess the patient with blunt injury. Asher, then followed by examining the use of ultrasound as a screening modality for suspected splenic rupture. In the middle of 1980, Tiling from Cologne University evaluated the application of ultrasound for thorax, retroperitoneum, and other intra-abdominal organs. Even though most of the ultrasound application and technology were performed in Asia and Europe, currently, the application of ultrasound especially for surgeons became more popular in North America.

By increasing the frequency of the ultrasound by several hundreds of MHz, any object with the size of micrometers can be observed because the resolution will increase, however this is under condition that any other parameters such as attenuation, diffraction and scatterer are considered. In addition, by mechanically move the transducer along x and y direction (scanning), a three-dimensional observation (imaging) can be performed. This way of measurement became the main concept of ultrasound microscope. Recently, by using the reflection coming from the target and the reference material, a two-dimensional view (often called C-mode image) can be obtained and interpreted into something more quantitative such as sound speed, attenuation, thickness and also acoustic impedance^(3),22-28). In biological cell observation, the change in properties of the target (cultured cell) after some treatment such as the addition of drugs can be monitored and assessed quantitatively⁽²⁹⁾⁻³¹⁾. In industrial application, ultrasound is normally used for locating the faults in a product, such as semiconductor devices^(32),33).

1.2. History of microscopic imaging (by ultrasound microscope)

In this study, the physical property of the object will be interpreted into acoustic impedance distribution. Most of acoustic impedance observation utilizes an acoustic impedance microscope. The history of microscopic imaging (by using ultrasound) for observing and visualizing biological matters such as tissues non-invasively, had been started in early 1971 by A. Korpel et al. with 100 MHz transducer and resolution of $25\ \mu\text{m}$ ⁽³⁴⁾. In 1973, Lemons et al. improved the hardware by employing a 400 MHz transducer with a resolution of $3\ \mu\text{m}$ ⁽³⁵⁾. Figure 1.1 illustrates the measurement system proposed by Lemons et al.



Figure 1.1. The proposed scanning acoustic microscope system and (b) the acoustic image of polystyrene particles (black bar indicates $100\ \mu\text{m}$) by Lemons et al in early 1971.

In 1979, Johnston et al. reported successfully observing the intracellular features of fixed cells such as nuclei and nucleoli, mitochondria, and actin cables with a resolution that was comparable to light microscope⁽³⁶⁾, as shown by Figure 1.2. In 1980, Hildebrand et al. reported successfully observing living cell in vitro. Since then, many researchers had attempted to improve many aspects ultrasound microscope, including its quantitiveness⁽³⁷⁾.

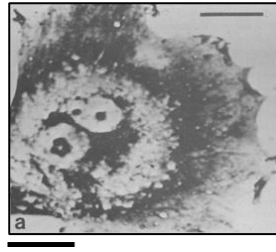


Figure 1.2. The acoustic image of binucleate fibroblastic cell (bar indicates 10 μm) by Johnston et al.

In 1991, Saijo et al. proposed a transmission and reflection mode by utilizing 200 MHz transducer and the attenuation and sound speed of the specimen was successfully obtained³⁸), as shown by Figure 1.3. However, a frequency scan which is performed by switching the frequency resulted in a long measurement time (it took approximately one hour for single measurement). In addition, the device used to maintain the frequency stability tended to complicate the system and also quite expensive.

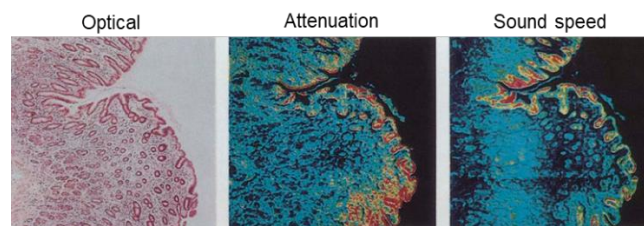


Figure 1.3. The attenuation and sound speed image by Saijo et al.

In 2003, Hozumi et al. proposed an ultrasound sound speed microscope by utilizing a sharp pulse with wide spectrum²⁷), instead of frequency switching as previously proposed by Saijo et al. This also simplified the system and lead to a faster measurement time, with approximately 2 – 3 minutes required for one observation. Then not long after that, in 2005, by using the similar system, Hozumi et al. proposed acoustic impedance mode observation by using acoustic microscope and acoustic impedance view of the cell was successfully obtained³⁹). The acoustic impedance mode was carried out by scanning the object from the bottom of substrate dish which parameters is known, as illustrated by Figure 1.4.



Figure 1.4. The layout of the proposed system and (b). the acoustic impedance result proposed by Hozumi et al. in 2005.

The acoustic impedance mode reduced contaminants in the object because the coupling medium and the transducer were separated by the substrate dish (compared with the sound speed mode). In addition, by referring to the acoustic impedance value of the substrate, the result could be made more quantitative as it is contrasted by an acoustic parameter such as acoustic impedance.

Later in 2014, Kobayashi et al. reported the application of ultrasound microscope with 300 MHz of focused transducer and the acoustic impedance view of cultured cell was successfully obtained⁴⁰⁾. It was also found that the application of drugs such as anti-cancerous drugs to the cell caused some reduction and changes in the trend of acoustic impedance^{30),31),41)}.

It also possible to observe the internal parts of the biological target (such as cell) along the depth direction of the beam (B-Mode) by using ultrasound microscope. However, conventional B-mode echography does not provide sufficient information related to the intracellular properties except that it displays only the intensity of the reflected signal. In recent study (2018), Hozumi et al. reported the success of converting the reflection intensity from the internal part of Glial cell into the distribution of acoustic impedance by converting each frame of reflection coefficient into the distribution of acoustic impedance, and a three-dimensional (3D) cross-sectional view of the cell was successfully obtained^{42),43)}.

1.3. Types of conventional ultrasound imaging

Figure 1.5. shows several types of ultrasound imaging applications based on its variation in frequency. Normally there are two types of imaging that can be produced by looking at the reflected waveform from the target, that is C-mode and B-mode imaging. The axial resolution of both imaging technique is directly proportional to frequency of the transducer. By simply taking the root mean square (RMS) of each scanning point, the C-mode (intensity) view of the target can be obtained. As shown by Figure 1.5, for larger scale of C-mode imaging such as uterus, around 10 MHz frequency is normally employed in the system. As for smaller scale such as the observation of faults in semiconductor devices, around 20 – 45 MHz of frequency is required. As for microscale C-mode imaging such as the cellular observation, the frequency higher than 50 MHz (up to several GHz in current application) is required. For microscopic purpose, normally a focused transducer combined with an XY scanning system are utilized in the system (this system is better known as ultrasonic microscope).

On the other hand, the reflection from layers along the depth direction can be observed by looking at the B-mode (brightness-contrasted) image^{2),3),7),10),44),45)}. In conventional B-mode imaging, the reflected waveform is firstly rectified and its envelope is then detected. This envelope image will display the strength of the reflected signal that comes from the tissue (intensity-contrasted image). The application of B-mode imaging is determined based on its range of frequency. For imaging the surface organ or carotid scan, frequency range up to 10 MHz is normally employed in the system. For smaller object such as intravascular imaging (IVUS) frequency range in between 20 – 45 MHz is required. Recently, the imaging of human skin layers with micrometer scale is performed by using ultrasonic transducer which frequency is higher than 50 MHz. Since human body, semiconductor devices and biological cell basically consists of several layers, they have a three-dimensional (3D) structure⁴⁶⁾⁻⁵¹⁾. This will make B-mode imaging suitable for depth observation because it provides more information related to the structure of the object compared with C-mode imaging.

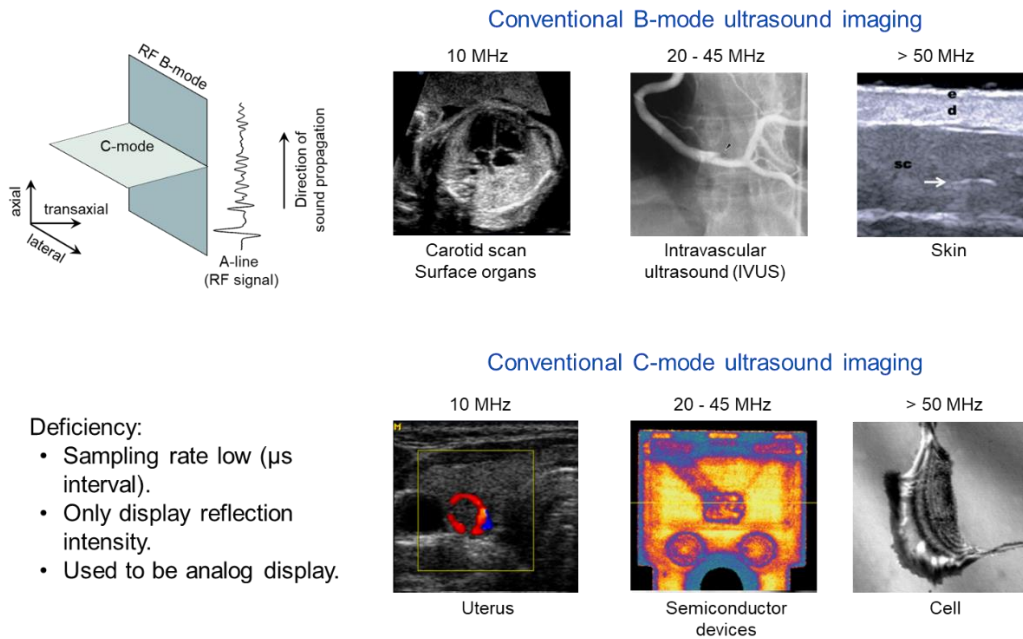


Figure 1.5. Several types of ultrasound imaging methods and their corresponding frequency for specific imaging applications^{52)–55)}.

However, the conventional C-mode and B-mode imaging as shown in Figure 1.5 does not contain much information except the intensity of the reflected signal either in the beam direction (B-mode) or in the interface between the object and the substrate (C-mode). In addition, the conventional measurement device had a low sampling rate and analog display was usually employed for displaying the measurement result which make a further processing is difficult to perform.

1.4. Recent wideband RF acquisition and imaging

Figure 1.6 illustrates the recent application of ultrasound imaging by means of RF signal. Utilizing the current technology, a data acquisition module with frequency sampling up to Giga sampling/s has been available in the market. This will lead to a faster acquisition (measurement) time with sampling rate up to ns of interval and since the waveform is digitized, the acquired data can be stored for further signal processing process.

Recently, various method for improving the quality of B-mode imaging such as noise reduction, contrast enhancement and beam forming have been proposed by some researchers^{56)–63)} In this study, we focus on the quantitative B-mode imaging by using the RF signal obtained from the measurement. The reflection coefficient is then obtained by deconvoluting the signal reflected from the target with the signal reflected from reference material (such as water). However, the conventional frequency domain deconvolution often leads to the instability of the baseline in the deconvoluted signal that is caused by low-frequency spurious in the spectrum. This will create an artifact when the waveform is integrated into the acoustic impedance distribution. Hence, we proposed a solution by performing deconvolution in both time and frequency domain.

The spurious in low-frequency spectrum is then replaced with the spectrum components calculated by time domain deconvolution.

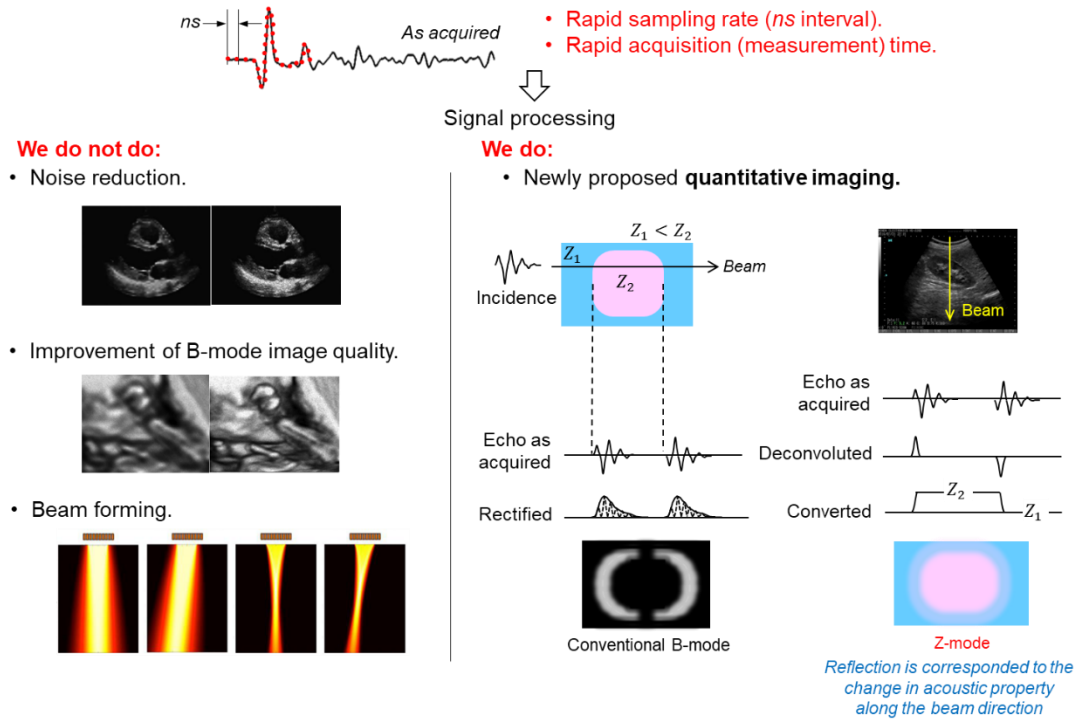


Figure 1.6. The recent application of RF signal acquisition and imaging^{55),64),65)}.

As a result, a cross-sectional image that is contrasted by acoustic impedance can be obtained. Each reflection is now corresponded to the change in acoustic property along the direction of the beam. In addition, the deconvoluted signal will have a better axial resolution (appear as a sharper image) compared with the enveloped one. The improvement of calculation and the analysis based on the result will be briefly discussed in the next chapter of this study.

1.5. Some industrial applications using acoustic imaging

Other examples of acoustic imaging using ultrasound in industrial field are the fault detection in semiconductor devices and the space charge measurement for insulation material. In case of fault localization in semiconductor devices, ultrasound has an advantage that it can propagate through the object (such as integrated circuit/ IC) without decapsulation (removing the mold resin so that it can reach the chip), compared with the conventional measurement by using laser where decapsulation is one of the requirements, as illustrated by Figure 1.7^{32),33)}. By scanning the object, the location of fault can be detected in two-dimensional plane (C-mode image).

This becomes the background of performing ultrasound assessment to other layered structure in industrial field such as the coating film monitoring in automotive industry. Since coating film is composed of several layers with different thickness and materials, the assessment

by using ultrasound will enable us to observe not only the thickness of each layer, but also the uniformity of the distribution in each layer.

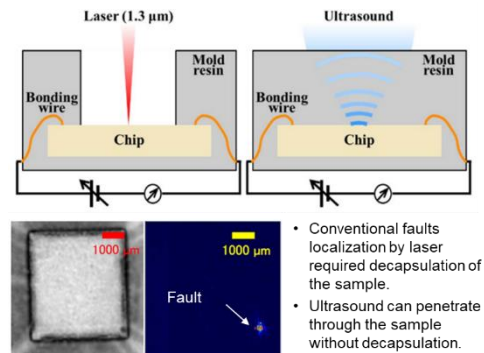


Figure 1.7. Localization of fault in semiconductor devices using ultrasound.

On the other hand, in space charge measurement for insulation material, cross-linked polyethylene is commonly used material in extra high voltage transmission cables and it may generate a significant space charge when exposed to a high DC voltage. The distribution of space charge has a relation with the degradation of insulation material. Normally, a sample which thickness is approximately $500\ \mu\text{m}$ is employed and several kV of high voltage is applied to the sample. The layout of the measurement system is shown by Figure 1.8. The deconvolution process is then applied to the acquired waveform in order to assess the space charge distribution inside the sample. Moreover, by integrating the waveform, the electric field and potential distribution can then be calculated^(66),67).

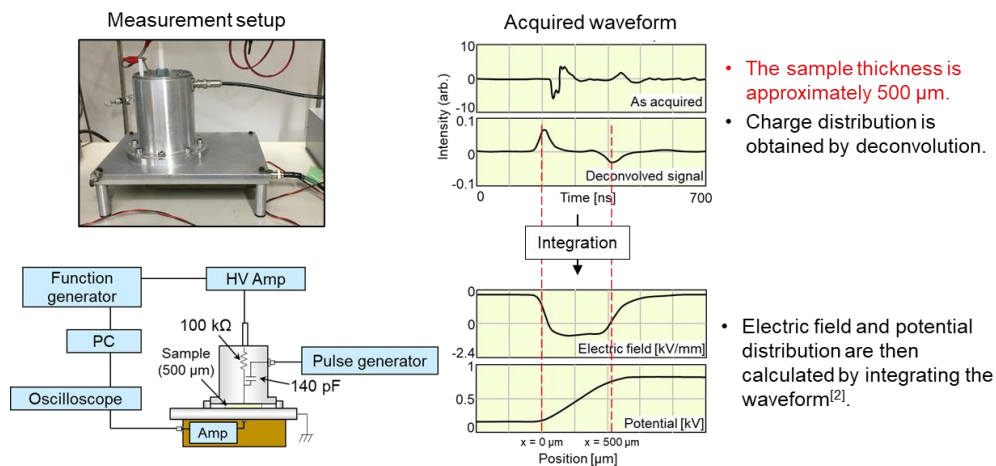


Figure 1.8. The measurement setup of space charge measurement in insulation material.

Since the space charge measurement in insulation material can be carried out with thin sample, it is also possible to apply the similar measurement system for much thicker sample, such as cross-linked polyethylene (XLPE) cable by using the Pulse Electro-acoustic (PEA) device^{(66)–(69)}. In this study, the space measurement in XLPE cable by using PEA device will be carried out

and by using the proposed signal processing method, the charge distribution, electric field and potential distribution will then be calculated.

1.6. Target of research

Several targets for cross-sectional acoustic imaging (by using ultrasound) that is classified as biological and industrial applications are chosen in this study, as illustrated by Figure 1.9. The observation targets are cultured cell, human skin, coating film and power cable. Since the conventional B-mode imaging is reconstructed from the enveloped signal, the axial resolution is poor. In contrast, in the proposed method, the signal is subjected into a deconvolution process so the image is contrasted by the reflection coefficient that comes only from the object, eliminating all the interfering reflections from the system. This will also increase the axial resolution because the detail along the depth direction will be maintained.

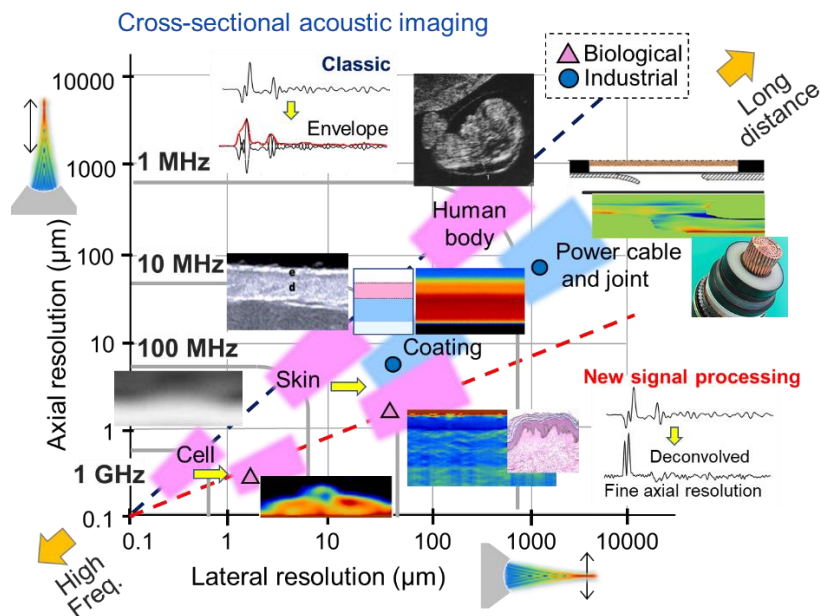


Figure 1.9. Target of quantitative acoustic imaging in this study^{15),55),70)}.

As shown by Figure 1.9, for the purpose of cell imaging, a frequency up to 1 GHz is required. This will result in spatial resolution up to 1 μm and since the target is thin and the conventional B-mode imaging is reconstructed from the enveloped signal, the resolution (sharpness) of the image will be reduced. On the other hand, by deconvoluting the signal, the axial resolution can be improved and in addition, the reflection coefficient can be interpreted based on the elastic property of the target (such as acoustic impedance) so the image will be more informative. For skin observation, the applied frequency for the observation is up to 80 MHz which will result in approximately 10 μm of spatial resolution. Similar with the proposed technique for cell observation, the axial resolution of the skin is also improved by deconvolution process and the generated image is also contrasted by elastic parameter.

As for coating film monitoring, since the depth of the target is almost similar with the skin observation, the applied frequency is also 80 MHz. Since coating film is consisted of layered structure, not only the thickness but also the uniformity of each layer can be assessed. In addition, similar with cell and skin observation, by using the reflection coefficient after deconvolution process, the distribution of each layer in the coating is also displayed by acoustic impedance.

The observation of charge (space charge) distribution inside a cable has a frequency range of 10 – 20 MHz because the depth of the target is long. By scanning process, the reflection along the cable joint can be obtained while applying a high voltage (up to 50 kV) into the cable. By deconvolution process, a two-dimensional (2D) space charge distribution along the cable joint can be observed. In addition, by integrating the waveform, the distribution of electric field, charge and the applied voltage can be obtained and will be discussed more in another chapter of this study.

Unlike the industrial target where the most of the properties of the sample has already been known, the biological target is more difficult because the properties of the sample along the depth direction is unknown. In addition, a thin object such as cultured cell required a high frequency of transducer in order to obtain a good spatial resolution. The spatial resolution is reduced as a lower frequency of transducer is employed (deeper measurement target). Moreover, high frequency measurement required a complicated hardware with high accuracy, which will increase the cost of measurement. However, since the target is very thin, the calculation (signal processing) is quite simple because it has a limited range of depth. In contrast, lower frequency measurement (such as human skin, coating film and power cable) does not require a complicated hardware so the measurement cost tend to be cheaper. However, since the observation target is deep, the signal processing will be more difficult especially when it comes to maintaining the stability of the baseline in the signal. This problem will be discussed in detail in the next chapter of this study.

1.7. Motivation and research objective

The cross-sectional acoustic property imaging will provide more information related to the internal structure of the target (that can be correlated with its elastic parameter, such as acoustic impedance) compared with the conventional C-mode imaging. In addition, by stacking all the calculated cross-sectional images, a three-dimensional observation can be carried out, which enables us to analyze the observed target from any direction.

However, the quality of the image is determined by the stability of the baseline in the deconvoluted waveform because quantitative conversion (such as acoustic impedance and electrical field calculation) requires an integration along the time axis. As the measurement target is deeper, the instability of baseline in the deconvoluted signal will also become stronger and lead to the accumulation of error which will appear as an artifact in the generated image. This makes deconvolution becomes the most essential process in acoustic property imaging.

Deconvolution process is carried out in order to reconstruct/ estimate the reflection coefficient that comes only from the target because it is naturally convoluted with the component of the system transfer function (that is assumed to be the impulse response of the system). Deconvolution process may be pretty complicated to be carried out in time domain, but it is pretty straightforward when the calculation is brought in frequency domain since it is equal to the division process of spectrum components. The conventional deconvolution method is performed by division process of signal coming from the target (target signal) and the signal coming from

the reference material (reference signal) after the waveforms are Fourier transformed. However, division in frequency domain often becomes a problem when the intensity of denominator in the spectrum is less than the noise, which will lead to the process called “noise divided by noise” or “division by zero”. This will make the resulting spectrum becomes really noisy in both low and high frequency parts. The noisy high frequency part of the spectrum may be smoothed by a low-pass filter, however, the noise in low-frequency parts cannot be rejected by simply applying a filter to it. This problem often led to a waveform with a wavy baseline when the result is converted back into the time domain. If this kind of waveform is interpreted into other physical properties (such as acoustic impedance or charge distribution, that is normally done by integration), an accumulation of error will occur especially as the integration goes deeper, which will appear as an artifact in two-dimensional image.

In order to deal with this problem, this study proposes a solution by performing “another” deconvolution in time domain. Since deconvolution in time domain does not take account each component of the spectrum, the instability after deconvolution process can be avoided. The low-frequency part from time domain deconvolution is then combined with the high frequency part from the frequency domain deconvolution, resulting a waveform with maintained both low and high-frequency components.

After the stability of the waveform is maintained, the accumulation of error during the interpretation process (such as acoustic impedance) can be minimized. In addition, the by stacking all the calculated cross-sectional images, the 3D observation can be performed. In this study, the proposed signal processing was also applied to other ultrasound-based (industrial) research fields, such as the coating film monitoring in automotive industry and the observation of space charge on XLPE cable by using Pulse-Electroacoustic (PEA) method and both showed a good result.

1.8. Thesis contributions

This study is expected to be able to contribute to the development process of acoustic property imaging (especially in terms of quantitative cross-sectional B-mode observation by means of acoustic impedance) in both biological and industrial applications. The proposed signal processing method has a contribution in several applications of ultrasound and all of them will be described below.

1. Acoustic impedance mapping for human cheek skin observation:
 - Non-invasive, fast and free-contaminant of observation can be performed.
 - In vivo observation can be performed.
 - The calculated cross-sectional image is more quantitative because it is displayed by its physical properties such as acoustic impedance.
 - The effect of applying skin product to the outer layer of skin such as horny layer can be observed.
 - The observation of each layer of the skin can be performed by means of its acoustic impedance value, which can be correlated with elasticity.
 - By calculating all the cross-sectional acoustic impedance images, the 3D reconstruction of skin layers can be performed. In addition, the change of acoustic impedance in the layers

of the skin and its correlation with the change of ages (young and old) and the generation of wrinkles can be carried out.

2. Precise cellular-sized observation by acoustic impedance microscope:
 - Non-invasive, free contaminants and living observation can all be performed.
 - The cross-sectional image is quantitative because it is contrasted by acoustic impedance.
 - The cell morphology and structure along the beam direction can be observed.
 - Some parts of the cell such as cytoskeleton, nucleus, cytoplasm and its distribution along the beam direction is visible.
 - The cell dynamism can be observed by monitoring the change in cell properties such as height and shape after a treatment is carried out to the cell (fixation by aldehyde).
 - By stacking all the calculated images, the height of the cell can be mapped and the analysis from all cross-sectional direction can be performed.
3. Coating film monitoring by acoustic microscope:
 - The alternative low-cost monitoring method for coating film is carried out.
 - The thickness of each layer can be calculated directly after the deconvolution process.
 - The uniformity distribution of each layer that is contrasted by acoustic impedance can be evaluated.
 - By scanning the coating film, two-dimensional view of the result can be obtained.
4. Space charge measurement by means of ultrasound propagation:
 - Even with the signal taken with low voltage, the distribution of charge inside the XLPE cable can be assessed by using dual domain deconvolution.
 - By scanning the cable, the 2D distribution of the charge inside the cable can be obtained.
 - Since the baseline is stable after deconvolution process, the field distribution could then be calculated by integrating the deconvoluted waveform.

1.9. Thesis organization

This thesis is divided into seven chapters as follows:

Chapter One describes the introduction and the state of art in this thesis.

Chapter Two describes the theoretical preparation of this thesis.

Chapter Three describes the acoustic impedance mapping for human skin observation. The chapter starts with the system setup and the application of dual domain deconvolution for calculating the reflection coefficient from the skin. The result is then converted into the distribution of acoustic impedance and single cross-sectional layer of human cheek skin is successfully obtained.

Chapter Four describes the optimal condition for dual domain deconvolution in order to improve the speed and the preciseness of the analysis. The optimal condition for improving the

quickness and precision of the analysis which includes the discussion about the down-sampling, the compensation by subtracting DC component in the time domain calculation and the border frequency between time and frequency domain will be discussed. As a result, a stack of cross-sectional acoustic impedance images (3D) was successfully calculated.

Chapter Five describes the application of ultrasound microscope for biological cell observation. The signal from cell is deconvoluted by using the signal coming from the reference material (water). The purpose is to observe the dynamism of cultured cell (Glial cell and Fibroblast cell) under ultrasound microscope. The deconvoluted signal is then converted into the distribution of acoustic impedance. Since 3D analysis can be performed, some parts of the cell along the beam direction such as nucleus and cytoskeleton became visible. In addition, the change in cell properties (that is correlated with the dynamism of the cell) such as height and shape after a specific treatment such as aldehyde fixation that was not visible under the light microscope, could be evaluated.

Chapter Six describes about the application of the proposed signal processing method to other ultrasound-based measurement system such as coating film monitoring in automotive industry and space charge measurement by using the pulse electroacoustic (PEA) method. The proposed signal processing is applied to evaluate the thickness and uniformity of each layer in coating film and to monitor the existence of space charge in the acquired signal from XLPE cable. As a result, in terms of coating film monitoring, the parameters such as thickness and uniformity distribution of each layer that is contrasted by acoustic impedance could be obtained. As for the space charge measurement, the distribution of charge intensity, electric field and potential could then be calculated from the deconvoluted space charge signal.

Chapter Seven describes the conclusion for this thesis and the possibility for future study and applications.

Chapter II

Theoretical Preparation of the Proposed Acoustic Imaging Method

This chapter will discuss about the theoretical background and literature used in this study. The chapter begins with the concept of acoustic impedance interpretation, its correlation with elasticity, waveform integration along time axis and the concept of dual domain deconvolution.

2.1. Acoustic impedance interpretation

When the reflection coefficient is obtained by deconvolution, each fragment of the reflection coefficient is interpreted into the distribution of the acoustic impedance. Normally, for acoustic impedance interpretation, the reflection coefficient is assumed to be a lossless transmission line, and an algorithm inspired by Time Domain Reflectometry (TDR) had previously been applied to calculate the acoustic impedance distribution of a cultured cell and human cheek skin along the depth direction^{(42), (43), (71), (72)}. In the previous study, this algorithm took account the multiple reflections inside the object in order to calculate the acoustic impedance of each frame along the assumed transmission line.

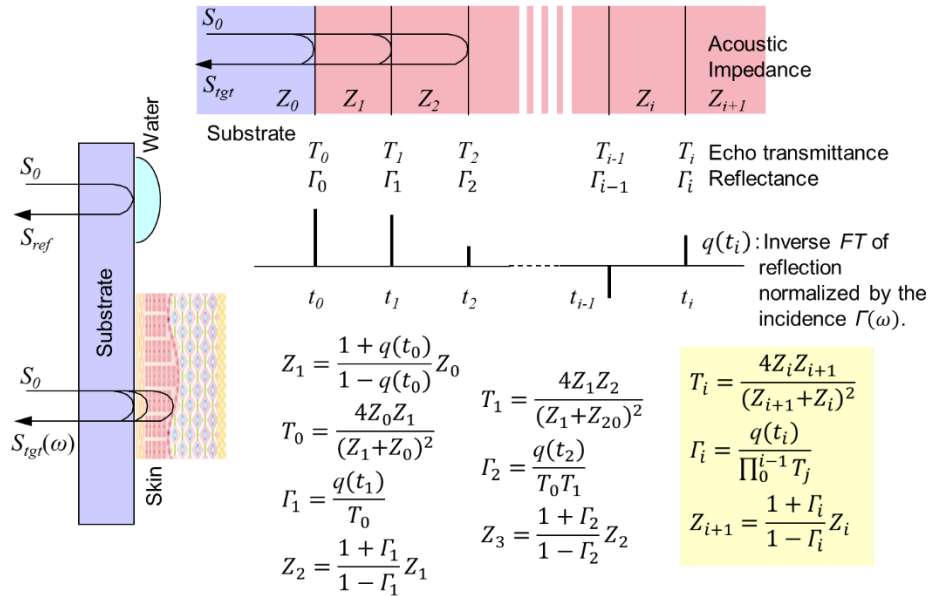


Figure 2.1. The process of interpreting each fragment of reflection coefficient into the acoustic impedance.

In the proposed method, since the multiple reflections inside the tissue is really small, which only contributes to less than 0.01% of the main signal intensity, neglecting them will make

the calculation simpler. Figure 2.1 shows the concept of the calculation when the multiple reflections are neglected by using human skin as the reference. The calculation is started by calculating the first impedance of the frame Z_1 based on the acoustic impedance value of the substrate (Z_0) which is already known and the value of the signal component $q(t_0)$, as expressed by

$$Z_1 = \frac{1+q(t_0)}{1-q(t_0)} \cdot Z_0 \quad (2.1)$$

the next step is calculating the transmittance of the echo signal T_0 , expressed by

$$T_0 = \frac{4Z_0Z_1}{(Z_1 + Z_0)^2} \quad (2.2)$$

as the signal component $q(t_1)$ is reflected at the interface between Z_1 and Z_2 and is detected after being subjected to the round-trip transmittance T_0 , the reflection coefficient Γ_1 can be represented as

$$\Gamma_1 = \frac{q(t_1)}{T_0} \quad (2.3)$$

by using the value of the calculated Z_1 and Γ_1 , the acoustic impedance of the next frame Z_2 can be calculated by

$$Z_2 = \frac{1+\Gamma_1}{1-\Gamma_1} \cdot Z_1 \quad (2.4)$$

similarly, the value of T_1 , Γ_2 and the acoustic impedance on the third frame which is Z_3 can be calculated as

$$T_1 = \frac{4Z_1Z_2}{(Z_1 + Z_2)^2} \quad (2.5)$$

$$\Gamma_2 = \frac{q(t_2)}{T_0T_1} \quad (2.6)$$

$$Z_3 = \frac{1+\Gamma_2}{1-\Gamma_2} \cdot Z_2 \quad (2.7)$$

repeating the process, the acoustic impedance of the whole frame Z_{i+1} can be calculated as

$$T_i = \frac{4Z_i Z_{i+1}}{(Z_{i+1} + Z_i)^2} \quad (2.8)$$

$$\Gamma_i = \frac{q(t_i)}{\prod_0^{i-1} T_j} \quad (2.9)$$

$$Z_{i+1} = \frac{1 + \Gamma_i}{1 - \Gamma_i} \cdot Z_i \quad (2.10)$$

Since the acoustic impedance interpretation process is similar to the integration along time axis, any instability in the deconvoluted waveform will cause an accumulation of error that propagates from front to rear. This is the main reason why the result of the deconvolution will determine the quality of the acoustic impedance image.

2.2. Elasticity and acoustic impedance

In human skin measurement, the relation between the sound speed in tissues and bulk modulus (normally defined as ‘elastic property’) is described as

$$c = \sqrt{(E / \rho)} \quad (2.11)$$

with c is the speed of sound and E is the elastic modulus. ρ is the density of the measured object and normally assumed to be constant in the biological tissues such as skin. This will lead to the speed of sound is directly depend on the elastic property in the skin⁷³.

On the other hand, the relation between acoustic impedance and the elastic property is described as

$$Z = \sqrt{(E * \rho)} \quad (2.12)$$

almost similar with the equation 2.11, here E and ρ represent the elastic modulus and the density of the specific area in the skin, respectively. Since the density ρ is assumed to be constant in all regions in the skin, this will make the acoustic impedance directly depends on the elastic property E of the skin.

2.3. Integration along time axis

During the interpretation process into the acoustic impedance, each fragment of the reflection coefficient after deconvolution process is converted into the distribution of acoustic impedance. The conversion process is similar to the integration along the time axis because the previous fragment is used in order to calculate the next fragment (chain process). However, if the baseline in the deconvoluted signal is unstable, this integration process will cause in an

accumulation of error that increase as the calculation goes deeper, as illustrated by Figure 2.2 with human skin data as the measurement target.

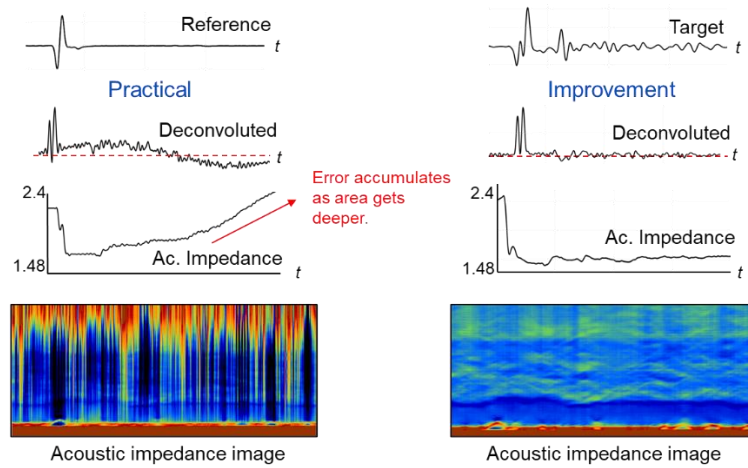


Figure 2.2. The waveform integration and the problem that commonly occur during acoustic impedance interpretation.

As previously described in the previous chapter, the conventional frequency domain will result in the instability of the baseline in the deconvoluted signal. If this unstable (normally appears as a wavy waveform) is integrated, it will cause an error integration and result in the generation of artifact in the acoustic impedance image.

2.4. Frequency domain deconvolution

In cross-sectional acoustic impedance imaging, deconvolution is a crucial process that is performed to reconstruct the reflection coefficient of the target that is naturally convolved with the components from the system transfer function. By assuming that the impulse response of the system is known, deconvolution can be performed. Deconvolution may be too complicated to be performed in time domain, however, it becomes much simpler if the operation is brought into frequency domain because it is equal to the division process of each spectrum components. The process of frequency domain deconvolution is illustrated by Figure 2.3, with measurement target is human cheek skin.

The frequency deconvolution process is started by convolving the target and the reference signal with a window function. The windowed signals are then subjected to Fourier transform and in Fourier domain, the target signal is divided by the reference signal. If the result is directly brought back into time domain, the resulting signal will often be really noisy, with some unwanted DC components that appear as a wavy baseline. A Gaussian filter is normally applied to the result of the deconvoluted signal in order to reduce the amount of unwanted high-frequency components, however, another problem will still exist in the low-frequency part of the resulting signal. This problem can be caused by several factors, such as the improper spectral division in the frequency domain which is caused by the frequency components of the reference signal that is often really small (often called ‘noise divided by noise’ or ‘division by zero’). It will lead to the missing of the necessary low-frequency components or even the creation of the unnecessary ones when the

waveforms are deconvoluted. As a result, the baseline in the deconvoluted signal is often unstable (curvy). This instability will lead to the accumulation of error when the waveform is converted into the acoustic impedance distribution.

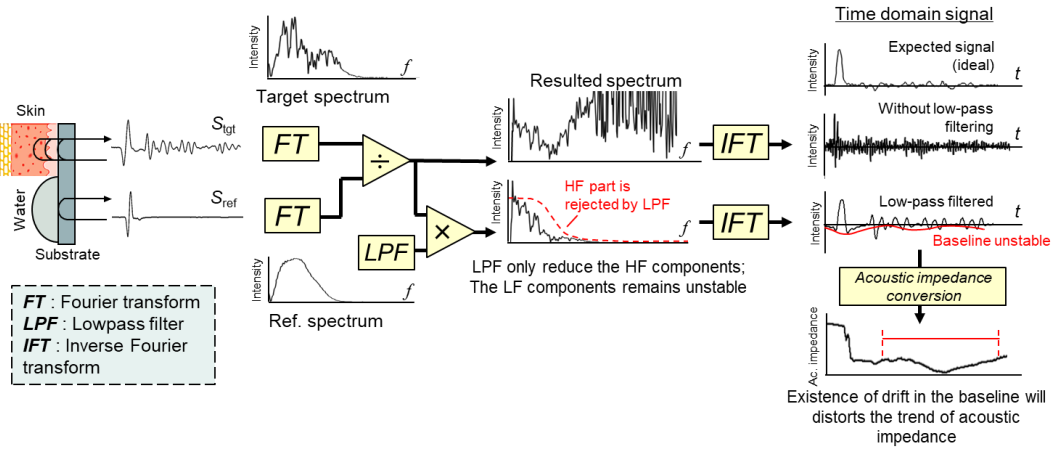


Figure 2.3. The workflow of frequency domain deconvolution.

The concept of the deconvolution in the frequency domain is similar to the application of Wiener filter which works by minimizing the mean square error between the desired input and the known output by using the Linear Time-Invariant (LTI) filtering. However, in order to apply the Wiener filter into the calculation, the estimation of the noise power in the system must be known and taken into account. In the measurement system, the exact estimation of the noise that exists in the waveforms is hard to obtain, so the application of Wiener filter to estimate the reflection coefficient from the skin becomes difficult to perform. Moreover, the problem of the missing or generation of the low-frequency components in the reconstructed signal can never be solved because the exact amount of the affected low-frequency components in the signal is unpredictable, which is why another method of deconvolution that can retain the low-frequency components of the signal is required.

2.5. Time domain deconvolution

Since it is almost impossible to predict the amount of the affected low-frequency components in frequency domain deconvolution, another way of calculation that can maintain the proportion of low-frequency components of the signal is proposed. Instead of performing a calculation in the frequency domain, the deconvolution of both signals is also performed in time domain. Figure 2.4 shows the concept of time domain deconvolution.

The target signal is the convolution between the signal that comes from the substrate and the signal that comes from the skin, and by assuming that the reference signal that comes from water is the impulse response of the system, the output s_{tgt} can be expressed as

$$s_{tgt} = Hs_{input} \quad (2.13)$$

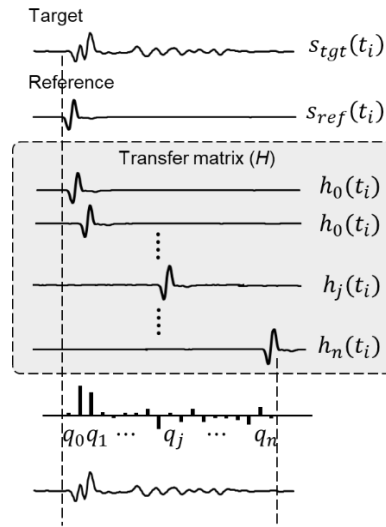


Figure 2.4. The generation of transfer matrix from the reference signal.

where s_{tgt} and s_{input} are the target and input signal, respectively and H is a template matrix that is obtained by shifting the reference signal with the appropriate interval on the time axis, with m and n is the number of shifting interval and the number of impulses, respectively. The form of the templates can be expressed by

$$\begin{aligned}
 & \begin{matrix} h_0(t_0) & \cdots & h_0(t_i) & \cdots & h_0(t_m) \\ \vdots & \ddots & \vdots & & \vdots \\ h_j(t_0) & \cdots & h_j(t_i) & \cdots & h_j(t_m) \\ \vdots & & \vdots & \ddots & \vdots \\ h_n(t_0) & \cdots & h_n(t_i) & \cdots & h_n(t_m) \end{matrix} \\
 H \equiv & \begin{matrix} h_0(t_0) & \cdots & h_0(t_i) & \cdots & h_0(t_m) \\ \vdots & \ddots & \vdots & & \vdots \\ h_j(t_0) & \cdots & h_j(t_i) & \cdots & h_j(t_m) \\ \vdots & & \vdots & \ddots & \vdots \\ h_n(t_0) & \cdots & h_n(t_i) & \cdots & h_n(t_m) \end{matrix} \quad (2.14)
 \end{aligned}$$

and by weighting each component of the matrix with q_j , the combination of the templates can be expressed by

$$s_{tgt}'(t_i) \equiv \sum_{j=0}^n h_j(t_i) q_j \quad (2.15)$$

then each impulse that has a distribution similar with the original signal can be determined by minimizing the square of the error between the target and the templates, as expressed by

$$\sum_{i=0}^m \left\{ s_{tgt}(t_i) - s_{tgt}'(t_i) \right\}^2 = \sum_{i=0}^m \left\{ s_{tgt}(t_i) - \sum_{j=0}^n h_j(t_i) q_j \right\}^2 \quad (2.16)$$

the output will be the distribution of impulse q_j on the time axis that represents the original signal, as expressed by

$$\begin{pmatrix} q_0 \\ \vdots \\ q_j \\ \vdots \\ q_n \end{pmatrix} = (H^T H)^{-1} H^T \begin{pmatrix} s_{tgt}(t_0) \\ \vdots \\ s_{tgt}(t_i) \\ \vdots \\ s_{tgt}(t_m) \end{pmatrix} \quad (2.17)$$

the final output of this time domain deconvolution is a signal with a maintained low-frequency component but poor in the resolution of high frequency components. The signal is also free from unwanted DC components and tend to be more stable.

2.6. Time and frequency (dual) domain deconvolution

The result of frequency domain deconvolution is a signal that is disturbed by a low-frequency spurious but has a good high frequency resolution. On the other hand, performing a down sampling to the signal in the time domain deconvolution will reject the high-frequency components and miss the fine structure of the signal, but the output of the calculation is free from disturbance of the low-frequency spurious.

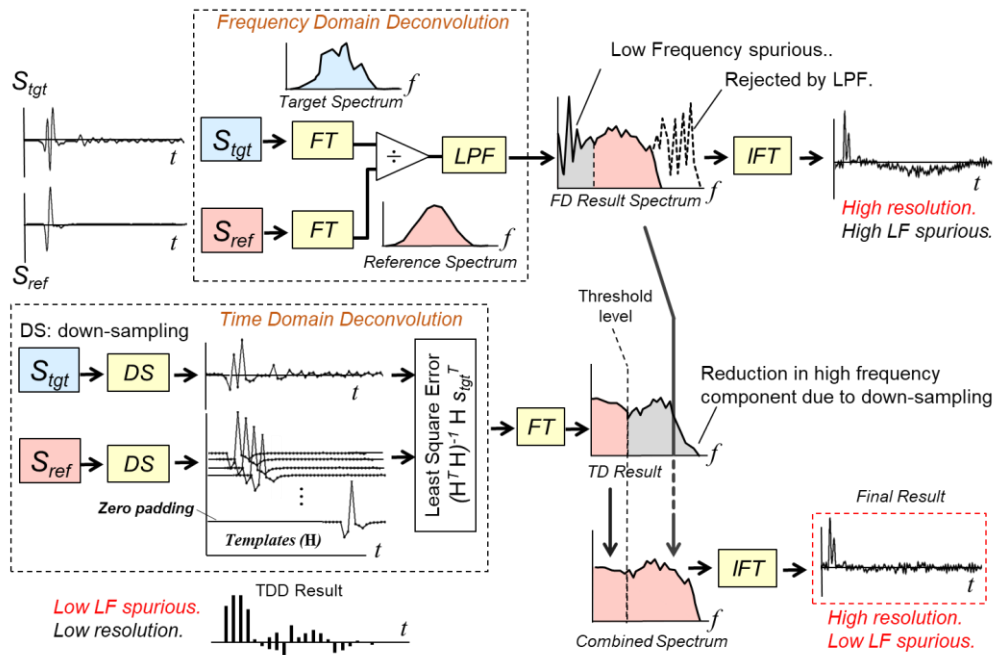


Figure 2.5. The stream of dual domain deconvolution.

Since the two methods still have their own advantages and disadvantages, combining the result of both methods will solve the problem in both domains. Figure 2.5 shows the stream of the time and frequency domain deconvolution. Firstly, the target and the reference signal are deconvolved by the frequency domain deconvolution. The output of the division in the frequency domain is subjected to a low-pass filter in order to reduce the unwanted high-frequency

components. Some spurious, however, still appear in the low-frequency part of the spectrum. If this result is brought back into the time domain, the output will be a signal with high-frequency resolution and a high amount of low frequency spurious. Time domain deconvolution is also performed to both target and reference signals. In terms of time domain deconvolution, the signals are firstly down-sampled by the factor of n in order to increase the calculation speed as well as reducing the amount of unwanted high-frequency components. The templates matrix is then constructed by shifting the reference signal in the time axis by some interval of n . Both the target signal and the templates are then subjected to the least square deconvolution to reconstruct the input signal while minimizing the square of the error. The output of this process is a signal that has a small amount of low-frequency spurious and has a low resolution.

After both calculations in time and frequency domain are done, both results are combined in the frequency domain by a threshold value that determines the amount of low and high-frequency compositions of the signal. The low-frequency part of the signal is obtained from the time domain calculation which is then combined with the high-frequency components from the frequency domain calculation. The final output will be a reconstructed signal with a maintained high-frequency resolution and free from low-frequency spurious.

Chapter III

Acoustic Impedance Mapping for Human Cheek Skin Observation

This chapter will discuss about the application of ultrasound microscope for human cheek skin observation. The chapter begins with the system setup used in the measurement. The supporting components such as the specification of transducer, substrate and the result of analysis will be described. The comparison between the result of the conventional and the proposed method will also be discussed.

3.1. Human cheek skin

The observation of human cheek skin has become popular especially for manufacturer of skin-related products and one of the concerns is the condition of skin face. This is because a healthy skin face contributes in the appearance and confidence of a person, especially for women. There are many produced skin care products that are dedicated to slow-down the aging process of the skin. They normally contain moisturizer in order to plump the skin and conceal the visibility of wrinkles. It has also been a fact that aging process of the skin cannot be stopped but many believes that it can be slowed down by the use of cosmetic products.

The sign that skin has become older is the increasing number of wrinkles and sagging skin. It is also indicated by the change of hair color (normally turns to white). Human skin consists of many layers; however, layers that normally visible after observation by using ultrasound are:

1. Horny layers

Horny layer or stratum corneum is the outermost part of the skin containing dead cells that slough off. This layer is considered to be the hardest layer in the skin.

2. Epidermis

Epidermis contains pigment, skin cells and proteins. It is a waterproof layer which acts like a barrier and determines the skin tone. It also protects the skin from bacteria or infection and regulates the amount of water that is released from the body.

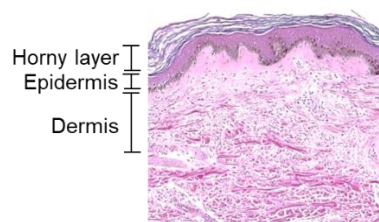


Figure 3.1. Layers of the skin⁷⁴⁾.

3. Dermis

Dermis is the layer located beneath the papillary layer. It contains blood vessels and some other structures such as sweat glands and hair follicles. Figure 3.1 shows the skin structure that consists of Horny layer, epidermis and dermis.

3.2. Skin property measurement

Most of researchers are trying to see the effect of applying skin product into the layers of the skin in order to see the phenomenon behind skin structure and produce the most suitable product for different skin conditions. In order to achieve that, several way of skin studies by utilizing devices such as Optical Coherent Tomography (OCT) and cutometer for assessing the skin parameters such as thickness and elasticity had been proposed⁴⁷⁾. As for skin layer measurement, OCT utilizes an infrared light with approximately 1310 nm of length that is emitted to the skin. the scattered light from the tissue is then captured and filtered by interferometer. The result of OCT measurement is shown by Figure 3.2. As a result, some layers of the skin such as epidermis, dermis dan subcutis becomes visible. By using this result, the shape and the thickness of the observed skin layer can be calculated. However, the quantitiveness of the result is low because the image is only contrasted by intensity of the reflected signal.

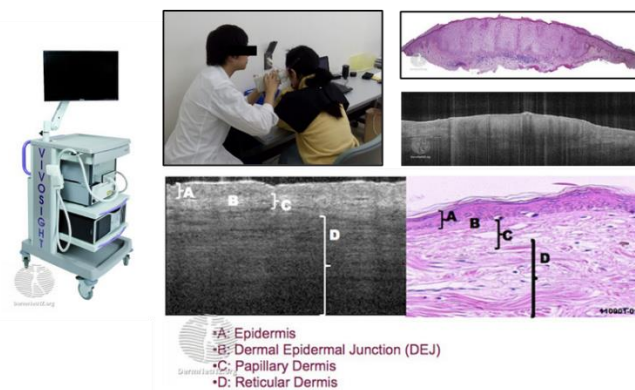


Figure 3.2. The skin measurement by using OCT⁷⁵⁾.

On the other hand, the elasticity measurement of the skin is normally performed by using cutometer, as illustrated by Figure 3.3. Cutometer works by applying negative pressure to the skin (suction) and after some specified time, the skin is released. During the suction process, a light is emitted and the elasticity of each layer are measured at the same time. This will lead to the difficulties of evaluating each layer in the skin because the pressure will affect the properties of the skin during measurement. In addition, the evaluation parameter that can be obtained is limited.

The application of scanning acoustic microscope for observing human skin was carried out by some researchers^{23),48),50),51)}. However, most of them required a sliced skin sample which is invasive. Chean et al. proposed the cross-sectional skin measurement by using ultrasound microscope⁷¹⁾. The subject placed their skin on top of a substrate dish and by mechanical scanning, the cross-sectional view of the skin along the beam direction could be obtained. This enabled us to perform an assessment of skin layers non-invasively and the requirement to slice the object was no longer necessary (living observation is possible). The generated cross-sectional image was

called RF imaging, because the RF signals were displayed as it were. However, this image did not provide sufficient information related to the skin structure because it contained the reflection coefficient from the skin that was overlapped (convoluted) naturally with the components from the transfer function of the system.

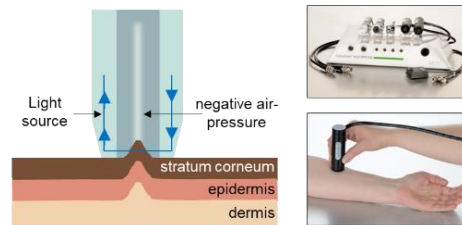


Figure 3.3. Elasticity measurement by using cutometer^{76),77)}.

The reflection that comes only from the skin was then reconstructed by a deconvolution process and by utilizing algorithm similar to Time Domain Reflectometry⁷¹⁾, each fragment of reflection coefficient was then converted into the distribution of acoustic impedance. This acoustic impedance representation was much more meaningful compared to the conventional B-mode imaging because each part of the skin is now contrasted by acoustic parameter which is related to the elasticity of the skin.

3.3. Measurement system

Figure 3.4 illustrates the measurement system for human cheek skin observation. The subject places their face on top of a substrate dish (polystyrene). In order to avoid interference of the air, a distilled water is applied between the skin and the substrate.

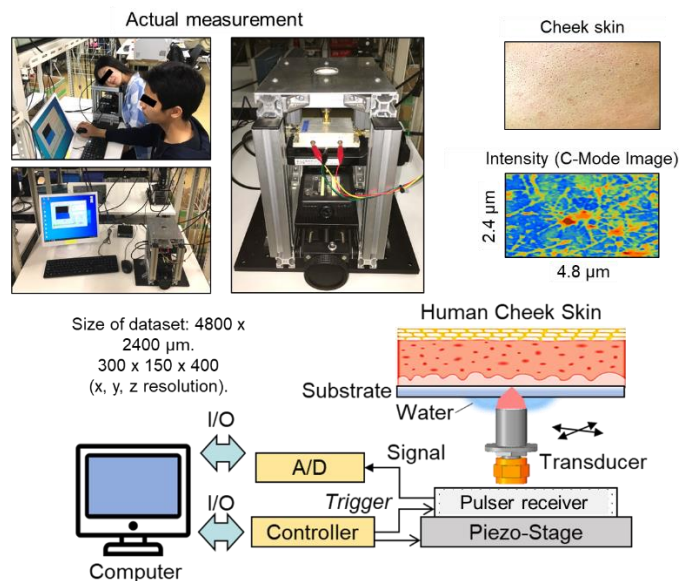


Figure 3.4. The measurement system for human cheek skin observation.

An 80 MHz focused transducer then scans the skin area from the bottom of the substrate, with the scan area of $4.8 \times 2.4 \text{ mm}^2$. The transducer is moved by a mechanical stage that is controlled by a personal computer (PC). A distilled water is used as the coupling medium between the bottom of the substrate and the top of the transducer. The reflection from the object is then captured by the same transducer and the waveform is sent to the PC by an analog to digital (A/D) converter. The waveform contains 400 samples with the sampling interval of 1 ns . A signal comes back from well-defined reference material (water droplet) is used as the reference signal.

3.4. Transducer specification

In human cheek skin measurement, a transducer that generates a focused ultrasonic beam is employed in the measurement. The transducer has a central frequency of 80 MHz with radius of approximately 1.2 mm. The focal length of the transducer is estimated to be 4 mm.

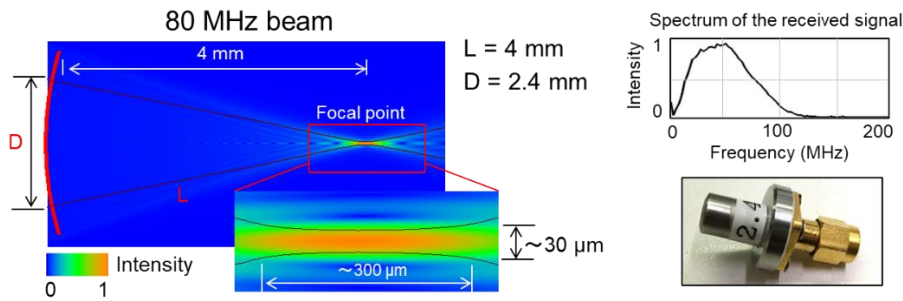


Figure 3.5. The properties of the transducer.

Figure 3.5 shows the transducer employed in the measurement and its acoustic field calculated by sound field analysis^{(24), (25), (78)}. The simulation shows that the transducer has an axial and lateral resolution of approximately $300 \mu\text{m}$ and $30 \mu\text{m}$, respectively. In addition, it shows that the highest intensity is located on the focal point.

3.5. Interpretation into apparent reflection coefficient

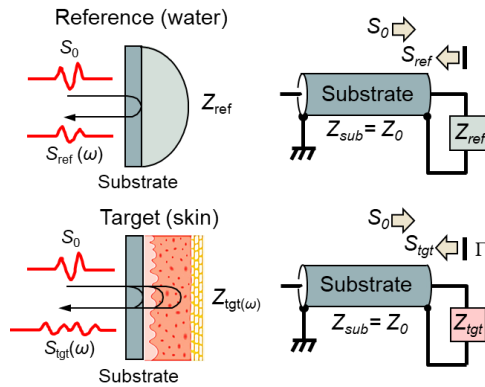


Figure 3.6. The relation between the target and reference signal.

Normally, the reflection coefficient of the target in touch with the same substrate can be determined by deconvolving the target signal $S_{\text{tgt}}(\omega)$ (signal reflected from the interface between the substrate and the skin) with the reference signal S_{ref} (signal reflected from the interface between the substrate and water) in the frequency domain, as illustrated by Figure 3.6.

As the reference signal comes back from a well-defined flat interface it can be recognized as proportional to the impulse response of the measurement system. The relation between target signal $S_{\text{tgt}}(\omega)$ and reference signal S_{ref} can be expressed by

$$\begin{aligned} S_{\text{tgt}}(\omega) &= \frac{Z_{\text{tgt}}(\omega) - Z_{\text{sub}}}{Z_{\text{tgt}}(\omega) + Z_{\text{sub}}} S_0, \\ S_{\text{ref}} &= \frac{Z_{\text{ref}} - Z_{\text{sub}}}{Z_{\text{ref}} + Z_{\text{sub}}} S_0, \end{aligned} \quad (2.18)$$

where $Z_{\text{tgt}}(\omega)$, Z_{ref} , Z_{sub} and S_0 are the acoustic impedance of the target, acoustic impedance of reference, acoustic impedance of the substrate and the transmitted signal, respectively. However, S_0 cannot be obtained by measurement, so it is converted from S_{ref} as expressed by

$$S_0 = \frac{Z_{\text{ref}} + Z_{\text{sub}}}{Z_{\text{ref}} - Z_{\text{sub}}} S_{\text{ref}} \quad (2.19)$$

The reflection coefficient at the surface of the substrate is then performed by deconvolving $S_{\text{tgt}}(\omega)$ with S_{ref} as one-dimensional signal. The reflection coefficient $\Gamma_0(\omega)$ at the substrate surface is expressed by

$$\Gamma_0(\omega) = \Gamma_{\text{tgt}}(\omega) = \frac{S_{\text{tgt}}(\omega)}{S_0} = \frac{Z_{\text{ref}} - Z_{\text{sub}}}{Z_{\text{ref}} + Z_{\text{sub}}} \cdot \frac{S_{\text{tgt}}(\omega)}{S_{\text{ref}}} \quad (2.20)$$

As many reflections are involved in the target signal, the reflection coefficient is time-dependent. As the fluctuation in acoustic impedance in the soft biological tissue is small compared with its absolute value of acoustic impedance, the reflection coefficient at each reflection point would be small as well. Therefore, the existence of multiple reflections can be neglected.

In the interpretation into acoustic impedance profile, the tissue is divided along the depth into many fragments; the thickness of each corresponds to the round traveling time within the sampling interval. In this series of analyses, the sound speed was assumed as 1600 m/s. As the exact sound speed through each fragment cannot be determined, the acoustic impedance profile may be slightly deformed like a regular ultrasound echography.

3.6. Acoustic impedance mapping by the proposed dual domain deconvolution

Figure 3.7 shows the result of the proposed dual domain deconvolution to the human cheek skin dataset. Since time domain calculation does not take account the spectral components in the signal, the generation of unnecessary low frequency components caused by improper spectral

division can be avoided. In addition, since the baseline is free from fluctuation, the accumulation of error that often occur during acoustic impedance interpretation can be avoided. As shown by the acoustic impedance result, the structure of the skin becomes visible and in addition, the layers of the skin such as stratum corneum, epidermis and dermis are each represented by different acoustic impedance value.

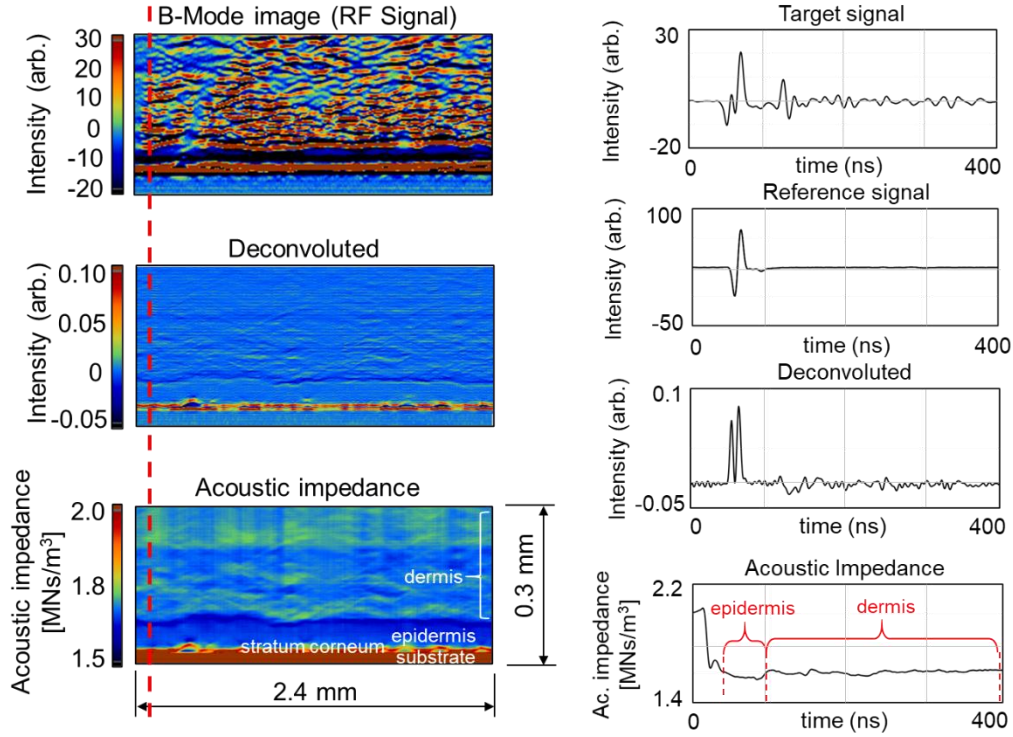


Figure 3.7. The acoustic impedance distribution of human cheek skin as the result of the proposed time and frequency (dual) domain deconvolution.

3.7. The comparison results between the conventional frequency domain deconvolution and the proposed dual domain deconvolution method

Figure 3.8 shows the comparison of the time-dependent reflection coefficient along the beam as well as the result when it is converted into the acoustic impedance distribution. As shown by Figure 3.8 (a), a strong reflection comes back from the interface between the substrate and the Horny layer, the waveform is disturbed by the low-frequency components which appear as a wavy baseline. This disturbance gives a strong influence when the result is converted into the acoustic impedance profile, as shown by Figure 3.8 (b). The proposed method, as shown in Figure 3.8 (c), has a profile that is free from the low-frequency components, in addition, the detail of the skin structure can also still be maintained. When this profile is converted into the distribution of acoustic impedance, as shown by Figure 3.8 (d), the difference of acoustic impedance value between the dermis and the area below the Papillary layer can be seen. The waveform also has a stable shape and a good distribution without any interference of unwanted DC components.

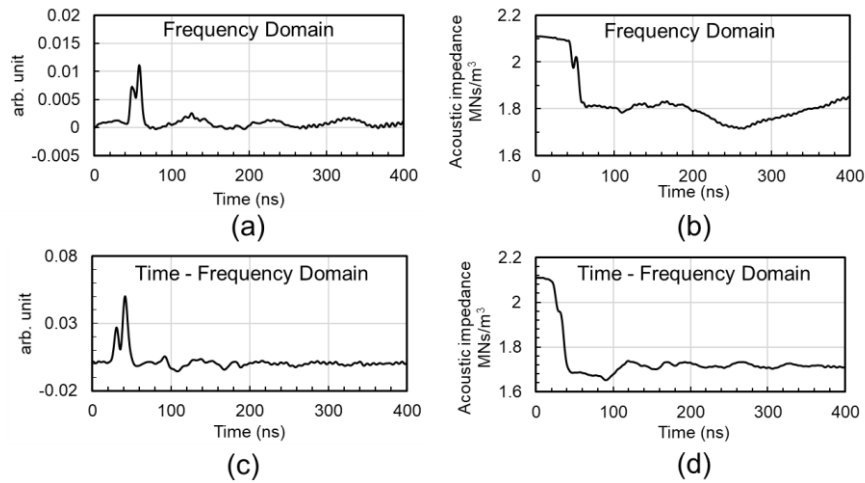


Figure 3.8. The comparison of the deconvoluted waveform calculated by conventional frequency domain and proposed dual domain deconvolution method.

Figure 3.9 shows the comparison between the result of the conventional frequency deconvolution and the proposed time and frequency deconvolution method, when applied to the same data of the human cheek skin.

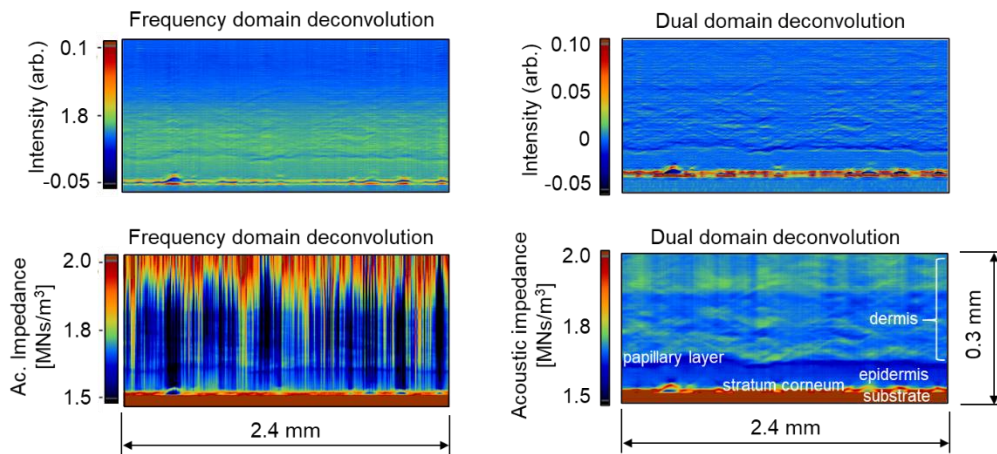


Figure 3.9. The comparison of the cross-sectional acoustic impedance result calculated by conventional frequency domain deconvolution and proposed dual domain deconvolution.

On the result calculated by frequency domain deconvolution method, the structure of the skin cannot clearly be seen since the image contains a lot of artifacts and high-frequency components that are caused by the improper frequency deconvolution process. The difference of acoustic impedance value between the area under the Papillary layer and the dermis also cannot be distinguished from the resulting image. This condition is completely different compared with the result of the time and frequency (dual) domain deconvolution method, where the structure of the skin can clearly be seen and the image is almost free from strong artifacts and high-frequency components.

3.8. Discussion

As shown by cross-sectional result of dual domain deconvolution, the detail and some layers of the skin structure especially on the dermis area can clearly be seen by using the proposed method. It also shows that the area between the Horny layer (Stratum Corneum) and the papillary layer has a lower acoustic impedance value compared to the area of dermis. This has a good agreement with the fact that the area under the dermis is filled with cells such as keratinocytes, while the dermis area which has a higher acoustic impedance value consists of elastin and collagen, which is harder in terms of structure^{46),74),79),80)}. In the previous research⁷¹⁾, in order to make the structure of the skin from the acoustic impedance image clearer, a differential type of edge-detect filter is applied along the y -axis of the image, with the consequences of the image losing its quantitiveness. However, by using the proposed method, this kind of operation is no longer necessary since the structure of the skin can directly be observed from the result of the acoustic impedance image.

When the reflection coefficient of the skin is interpreted into the acoustic impedance, the trend of the acoustic impedance distribution sometimes tends to increase or decrease from its normal value. This phenomenon may appear as a form of stripes in the image. In order to deal with this, the average along the scan area (x -axis) is taken on the dermis and the epidermis area, these values are then used as the reference to align some stripes that appear in the image back to their normal distribution value.

Since the transducer used transmits a high-focused ultrasound beam, during the propagation of the ultrasound beam through the substrate, the direction of the beam will not completely be a plane wave and tend to be slanted to the direction of the skin surface. An angle compensation obtained from the numerical sound field analysis is then used to correct the oblique incidence of the beam^{24),81)}.

3.9. Conclusion

A deconvolution in both time and frequency domain was applied to determine the cross-sectional acoustic impedance profile. The low and high-frequency components were obtained from the result of calculation in the time and frequency domain, respectively. The multiple reflections inside the human skin were also neglected in the calculation since they only contribute by less than 0.01% of the direct reflections in signal intensity. An angle compensation to correct the slanting angle of the ultrasound beam propagation is also applied to the result of the acoustic impedance. As a result, a clear view of the human cheek skin structure was obtained, compared to the result when the deconvolution was performed only in the frequency domain. Unlike the conventional method, the proposed one could maintain the detail of the skin structure in the waveform, as well as the waveform being free from unwanted DC and low-frequency components.

Chapter IV

Optimal Condition for Dual Domain Calculation (Speed and Preciseness Improvement) Applied to Human Skin Observation

Since a single slice of cross-sectional acoustic impedance image does not provide enough information related to the skin properties, three-dimensional analysis becomes a requirement to be carried out. Nevertheless, by performing three-dimensional observation, some optimal conditions in the calculation needs to be taken into account, in order to increase the speed and preciseness of the calculation. This chapter will discuss about the optimum condition for dual domain deconvolution, such as the reduction of samples by down-sampling, the border frequency between time and frequency domain and the compensation by subjecting a DC offset into the calculation. As a result, the calculated images are then correlated with ages to clarify the mechanisms of wrinkle in different generation⁷³⁾. Moreover, the 3D reconstruction of layers in human cheek skin as well as the correlation between the change in acoustic impedance along with ages (young and old) will also be described.

4.1. 3D acoustic impedance observation

In the previous chapter, the cross-sectional acoustic impedance image of the human cheek skin by using dual domain deconvolution had successfully been obtained. However, a single cross-sectional acoustic impedance image does not provide much information because human cheek skin is wide and its structure is not uniform (almost rough). In addition, each cross-sectional image contains different information about the skin properties.

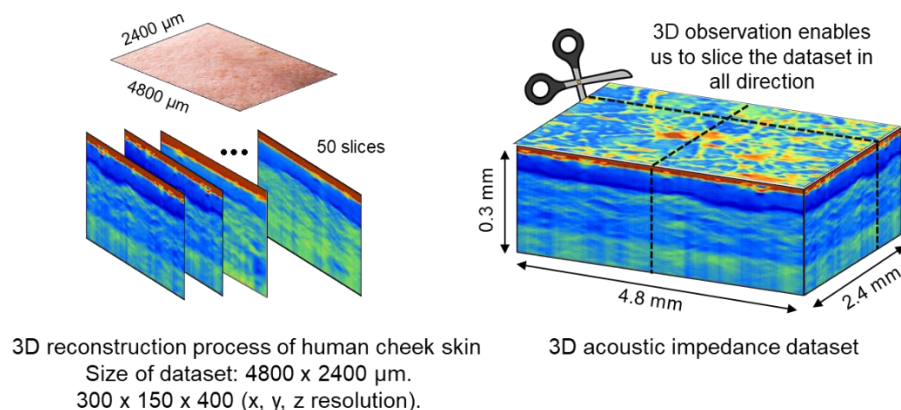


Figure 4.1. The skin dataset that is created by stacking all calculated cross-sectional acoustic impedance images.

In conjunction with that, a three-dimensional acoustic impedance observation is proposed because three-dimensional acoustic impedance data will enable us to observe the human cheek skin from all cross-sectional direction. All the cross-sectional slices along the scan direction will be converted into the acoustic impedance distribution and three-dimensional analysis will be performed. As much as 50 slices of cross-sectional acoustic impedance images will be stacked together. This will create a 3D acoustic impedance data with area measurement of $300 \times 150 \times 400$ (x , y , and z resolution), with area size of $4800 \times 2400 \mu\text{m}$, as illustrated by Figure 4.1.

By performing 3D analysis, the reconstruction of some layers in the skin can be carried out by utilizing its calculated acoustic impedance value. Moreover, the quantitative observation based on the skin condition and its correlation with ages (young/ old) can be carried out.

4.2. Down-sampling and its effect to calculation time

During time domain deconvolution, the target signal is deconvoluted by a transfer matrix generated from the shifted reference signal. Because time-domain calculation does not take into account all the frequency components of the signal, the resulting waveform will have a maintained low-frequency component. The calculated spectrum in both time and frequency domain are then combined by using a threshold value. However, the computation speed in time domain deconvolution will strongly dependent on the size of the transfer matrix used in the calculation. In order to deal with this, both signals are reduced by down-sampling before the time domain deconvolution in order to speed up the calculation time.

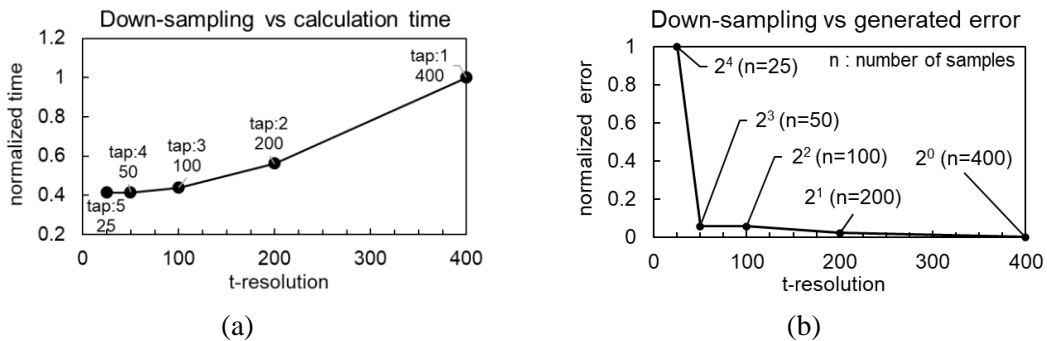


Figure 4.2. The down-sampling operation and its effect to (a). Calculation time and (b). calculation error.

Figure 4.2 (a) shows the result of performing several levels of down-sampling and its consequence to the calculation time. Since the number of samples is always the same for each dataset (400 samples), only one dataset is used for this assessment of calculation time. Firstly, the dual-domain deconvolution is performed without down-sampling (400 samples) and the time required for calculating one slice of image is taken. It takes approximately 0.14 seconds to calculate a single slice of image without down-sampling. The down-sampling with different taps number (levels) is then performed and result is shown in Table 4.1. As shown in Figure 4.2 (a) and Table 4.1, the required time for calculation reduces to almost half when the level of down-sampling is increased. This may suggest that the sample reduction by down-sampling in calculation does help to speed up the calculation time. There is almost no significant difference

in the calculation time for the down-sampling level of 2, 3 and 4, which is caused the number of samples in the signal that has become small. If the selected taps number (down-sampling level) is too high, the signal will lose most of its high-frequency components and aliasing will occur. In addition to that, the signal will also lose its original profile because the number of samples is limited.

Table 4.1. The calculation time required for each down-sampling level

Down-sampling level	Number of samples	All 50 slices		Single slice	
		Execution time (s)	Normalized time (s)	Execution time (s)	Normalized time (s)
0 (no down-sampling)	400	7.30	1	0.145	1
1	200	4.13	0.560	0.082	0.561
2	100	3.23	0.430	0.064	0.438
3	50	3.05	0.410	0.061	0.417
4	25	3.03	0.401	0.060	0.410

4.3. Down-sampling and its effect to calculation error

Figure 4.2 (b) shows the different levels of down-sampling and the generated error calculated from several slices of acoustic impedance image. Firstly, the calculation is performed without down-sampling (full resolution signal; 400 samples) and the calculated acoustic impedance image is used as the reference (ideal condition). Secondly, several levels of down-sampling are performed and the difference (error) between the calculated image before and after down-sampling is calculated, as expressed by

$$\Delta e = |p_{\text{ideal}} - p_{\text{down-sampled}}| \quad (4.1)$$

With Δe is the absolute difference or error between the ideal condition (p_{ideal}) and after down-sampling ($p_{\text{down-sampled}}$). The average of error for each down-sampling level ($E_{DL(m)}$) is taken from 15 different slices (N) of B-mode image in the same dataset, as shown by equation 4.2. $\Delta e_{DL(m,N)}$ is absolute difference at down-sampling level m and number of slices n , with $m = 0, 1, 2, 3, 4$:

$$E_{DL(m)} = \frac{\sum_{n=1}^N \Delta e_{DL(m,N)}}{N} \quad (4.2)$$

with m and N are the level of down-sampling and the number of averaged slices, respectively. All the calculated error are then normalized and the result is shown by Figure 4.2 (b). As the level of down-sampling is increased (smaller number of samples), the difference (error) of the image before and after down-sampling also increases. There is almost no significant error when 2¹ down-sampling level ($m = 1$; 200 samples) is applied to the signal. In other words, in this study,

reducing half of the sample number in the dual-domain calculation is considered to be acceptable and this will result in approximately 3.5 seconds when calculating all the 50 slices.

4.4. Frequency border of dual domain

Figure 4.3 shows the result of appending some number of low-frequency components from the result of time-domain deconvolution into the dual-domain calculation. The high-frequency components of the frequency domain deconvolution were reduced by a lowpass filter while the high-frequency components of the time-domain deconvolution depends on the level of down-sampling.

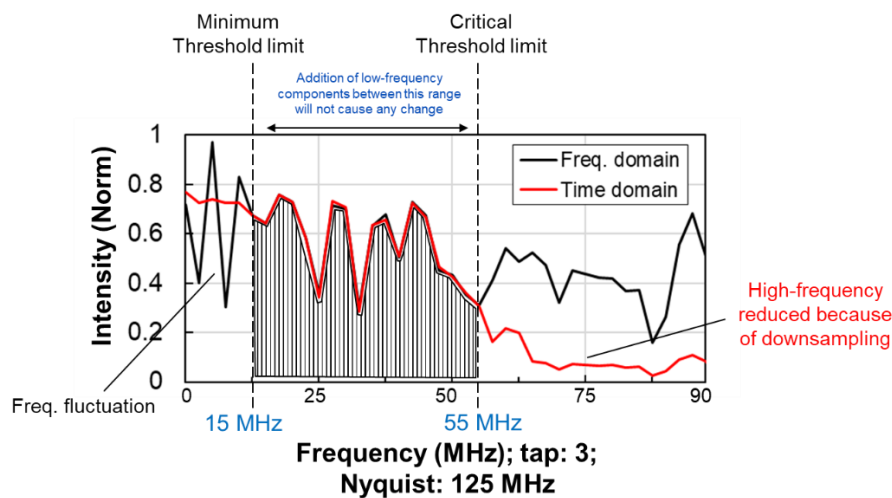


Figure 4.3. The amount of appended low-frequency components into the dual domain calculation.

As shown by Figure 4.3, the fluctuation in low-frequency parts of frequency domain deconvolution appears up to the frequency of approximately 15 MHz. This value is used as minimum threshold limit for low-frequency components of time domain deconvolution to be appended into the spectrum of frequency domain deconvolution. The frequency range of 15 – 55 MHz is the safe zone, which means that the spectrum generated by both time and frequency domain is similar and appending low-frequency components inside this range of frequency will not result any significant change in the signal. The frequency limit of 55 MHz is considered as critical threshold limit, since the high-frequency components of time domain deconvolution will be reduced because of down-sampling. Appending frequency components from time domain deconvolution exceeding this critical threshold limit will cause an error similar to aliasing.

If down-sampling operation (with the level indicated by m) is applied to the signal during time-domain deconvolution, the sampling frequency will be reduced by a factor of m . In time domain deconvolution with 1 ns of sampling interval and full resolution signal (400 samples), the folding frequency (Nyquist) of the spectrum can be calculated by equation 4.3.

$$f_s = \frac{1}{1 \text{ ns}} = 1 \text{ GHz}$$

$$f_{\text{fold}} = \frac{f_s}{2} = 500 \text{ MHz}$$
(4.3)

With f_s is sampling frequency and f_{fold} is the Nyquist frequency. If the signal is down-sampled by factor of 1 ($m = 1$; 200 samples), the new Nyquist frequency of the spectrum will be decreased m times, as shown by equation 4.4, with m is the level of down-sampling:

$$f_{s-m} / 2 = \frac{f_s}{2 \cdot 2^m}$$

$$= \frac{1 \text{ GHz}}{2 \cdot 2^1} = 250 \text{ MHz}$$
(4.4)

Since the transducer has a central frequency of approximately 70 MHz, the aliasing will not occur. However, if the selected down-sampling level is too high, aliasing will occur because the number of samples are too limited and this will cause an error in the acoustic impedance calculation.

4.5. The appearance of offset in the signal

In practice, the baseline of the raw-signal (as acquired) suffers from a small offset that is caused by some factors during the measurement, such as the movement of the subject, the vibration caused by the scanning motor, or even the offset that comes from the measurement system itself. Figure 4.4 illustrates the view of the scanned area.

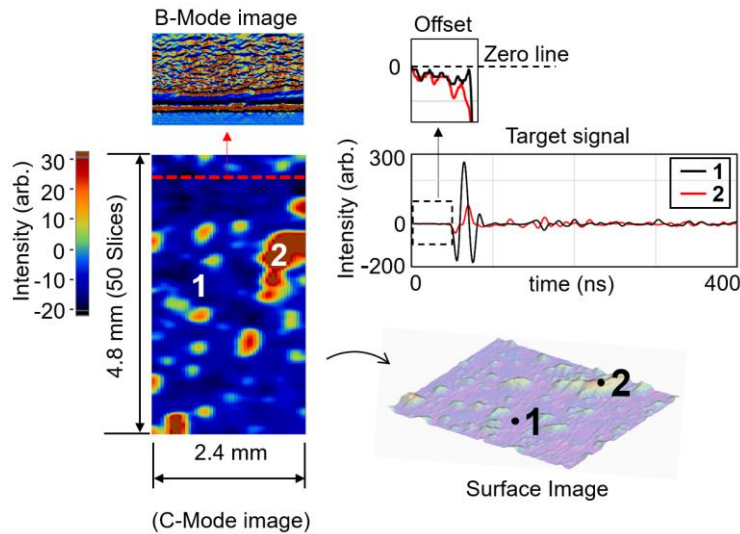


Figure 4.4. The measurement area of the skin and the existence of offset in the signal.

The C-Mode image represents the intensity of the signal by means of root mean square (RMS) on the interface between the surface and the skin, with an area size of $4.8 \times 2.4 \text{ mm}^2$. The C-Mode image contains as many as 50 cross-sectional slices where the view of the slice is represented by the B-Mode image. When the intensity in the C-Mode image is plotted into a surface graph (right image), it appears that the intensity of the reflected waveform varies, and some area with a high intensity also appears in the image that is caused by several factors, such as air bubble that gets trapped on the interface between the substrate and the skin or because the surface of the human skin itself is originally rough.

The area marked by 1 and 2 in Figure 4.4 shows the reflection coming from the skin and the reflection coming from the area with high intensity, respectively. The signals from these areas are plotted in the time domain graph on the upper right image. When the signal is zoomed in, it appears that there is a drift of offset in the signal which becomes stronger as it moves to the area with high intensity (shown by number 2 on the time domain graph). When the signal that contains offset is deconvoluted, the deconvolution result will be unreliable. In order to deal with this problem, a small amount of DC component is added into the transfer matrix in the time domain calculation.

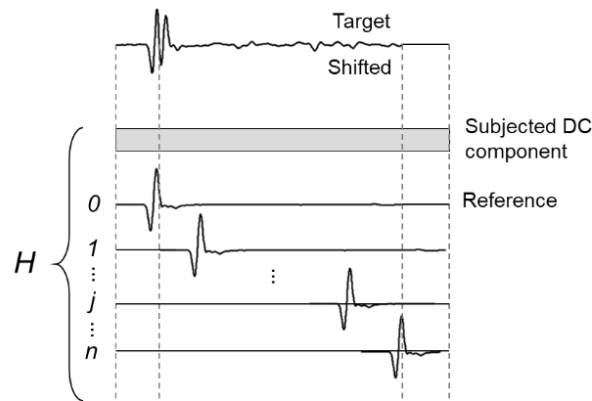


Figure 4.5. The transfer matrix with DC component subjected.

A small constant (DC component) with the same length of the reference signal is then appended to the two-dimensional transfer matrix, as illustrated by Figure 4.5. The relation between the appended offset and the transfer matrix is expressed by equation 4.5.

$$\begin{aligned}
 & \begin{matrix} h_0(t_0) & \cdots & h_0(t_i) & \cdots & h_0(t_m) \\ \vdots & \ddots & \vdots & & \vdots \\ H \equiv h_j(t_0) & \cdots & h_j(t_i) & \cdots & h_j(t_m), \\ \vdots & & \vdots & \ddots & \vdots \\ h_n(t_0) & \cdots & h_n(t_i) & \cdots & h_n(t_m) \end{matrix} \\
 & \vec{s} = [s_1, s_2, \cdots, s_n] \\
 & H' = \begin{bmatrix} H \\ \vec{s} \end{bmatrix}
 \end{aligned} \tag{4.5}$$

With \vec{s} is a row vector with the same element and its intensity is equivalent to the root mean square (RMS) of the reference signal. H' is the concatenation between H and \vec{s} . The intensity of the appended DC component into the transfer matrix was chosen to be equivalent to the RMS of the reference signal in order to maintain the weight of all components inside the matrix to be the same. In general, time domain deconvolution is performed so that the output waveform can be reproduced by the linear combination of the elements of the transfer matrix. As long as the appended DC component has a finite value, the appropriate coefficient q_n can be obtained by Least square method. Changing the intensity of the appended DC component is equivalent to changing the weight of each element in the transfer matrix. In fact, the result was not sensitive to the intensity of the DC component unless the difference from the strength of the reference signal was in many orders of magnitude.

4.6. The comparison of the deconvoluted signal

Figure 4.6 shows the result of the deconvolution performed in the frequency domain and dual-domain deconvolution (with and without the addition of DC components in the transfer matrix). The red dotted line indicates the area shown in time domain graph on the right side of the intensity image.

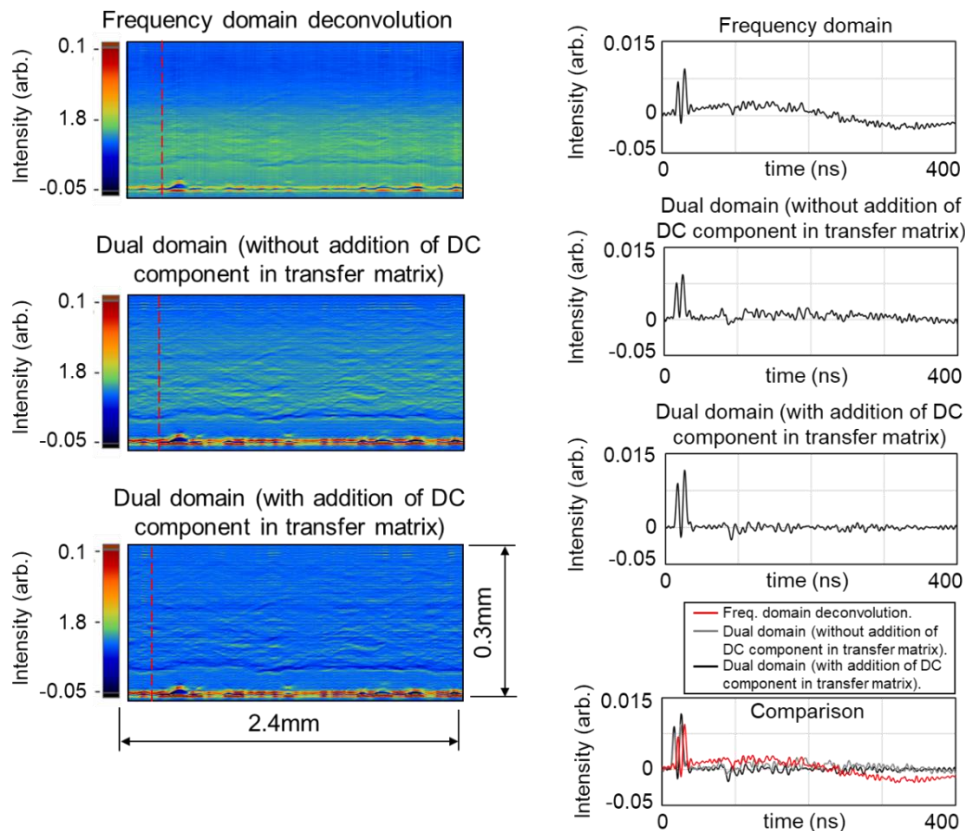


Figure 4.6. (Intensity image) The effect of adding a DC component to the result of the deconvoluted waveform.

A strong drift appears in the result of the frequency domain deconvolution because most of the low-frequency components are disturbed. This drift appears as an area with strong and low intensity in the intensity image.

On the other hand, the result of the dual-domain without the addition of DC component in the transfer matrix is much more stable compared with the result of the frequency domain deconvolution. However, there is still some drift left in the signal. When a small number of DC component is added into the calculation, it will stabilize the trend of the deconvoluted signal as it appears straight without any influence of drift in the waveform.

4.7. Kurtosis calculation

In order to validate the stability of the waveforms generated from different types of deconvolutions, a kurtosis calculation is applied to the baseline area of each waveform. Kurtosis is a statistical parameter that indicate how the distribution (histogram) is concentrated at a certain value of variable.

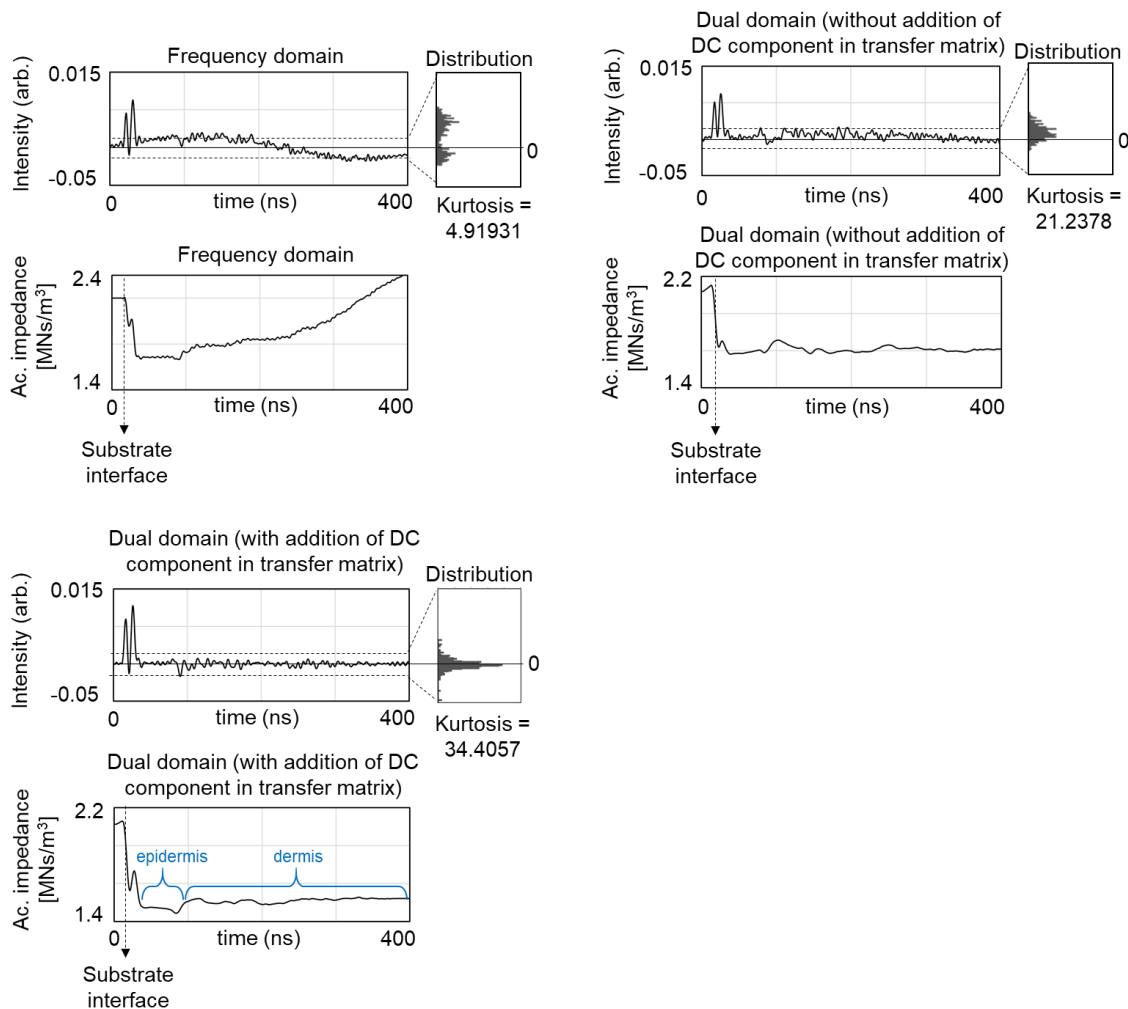


Figure 4.7. The result of the kurtosis calculation on each deconvoluted waveform.

As the intensity distribution is considered to be concentrated at the baseline, this parameter will be suitable to indicate the stability of the baseline, where a small number of kurtosis indicates a flatter histogram distribution or when the signal distribution is not centered at zero line (indicating the existence of strong drift in the waveform). On the other hand, when the distribution is perfectly centered at zero, it will result in a high kurtosis value. Figure 4.7 shows the result of the kurtosis calculation of each waveform started from the substrate interface (marked by the vertical dotted line).

Table 4.2. The kurtosis calculation of 10 different skin datasets with different types of deconvolutions.

Subject	Kurtosis		
	Frequency Domain Deconvolution	Dual-Domain Deconvolution (Without DC component in transfer matrix)	Dual-Domain Deconvolution (With DC component in transfer matrix)
1	4.92	21.2	34.4
2	2.89	18.8	31.6
3	5.78	24.9	28.9
4	9.64	19.9	31.9
5	5.78	28.7	35.9
6	10.0	12.6	40.9
7	12.8	21.9	41.1
8	11.0	23.8	25.1
9	12.9	28.0	32.9
10	14.8	25.9	30.0
Mean	9.06	22.6	33.3

On frequency domain deconvolution, since the baseline is unstable, the histogram distribution of the waveform tends to be flat and it has the smallest kurtosis value, that is 4.92. On the other hand, the dual-domain deconvolution without the addition of DC component in the transfer matrix has a narrower histogram distribution, however, since there is still some DC components in the baseline, its distribution is still not well centered on zero line, with the kurtosis value of 21.2. On the result of dual-domain deconvolution with added DC component in the transfer matrix, the waveform has a distribution that is centered at zero. In addition to that, it has the highest kurtosis value among all, which is 34.4.

In order to test the robustness of the addition of DC component in the dual-domain deconvolution, the kurtosis calculation was performed on 10 different datasets that were taken from 10 different person and the result is shown in Table 4.2. Based on the calculated result on the table, it shows that the dual-domain deconvolution with the addition of DC component has the highest kurtosis value among all, with the mean value of 33.3.

Figure 4.8 shows the result of several types of deconvolutions when being converted into the acoustic impedance distribution. Since the drift in the frequency domain deconvolution is

strong, it will generate a strong artifact in the acoustic impedance image. This is because the drift that appears in the signal will cause an instability when the waveform is integrated by using the TDR algorithm.

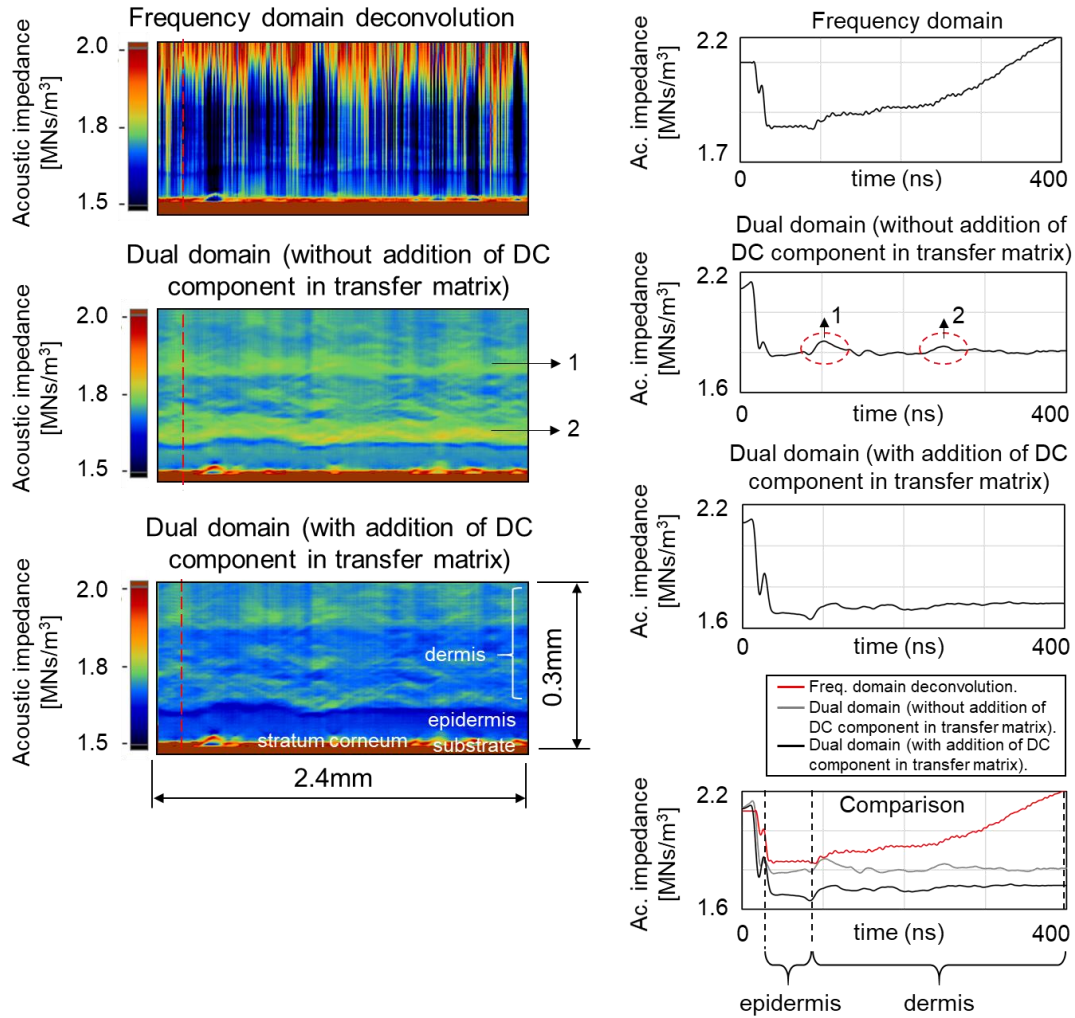


Figure 4.8. The effect of adding DC component and its improvement to the acoustic impedance image.

On the other hand, on the result of dual-domain algorithm without the addition of DC component in the transfer matrix, the waveform becomes much stable compared with the result of the frequency domain deconvolution, however, it still contains a high acoustic impedance value, especially on epidermis and dermis area. Moreover, there are two additional peaks on the dermis area, shown by the area 1 and 2 on the image. These peaks appear as strong stripes on the acoustic impedance image.

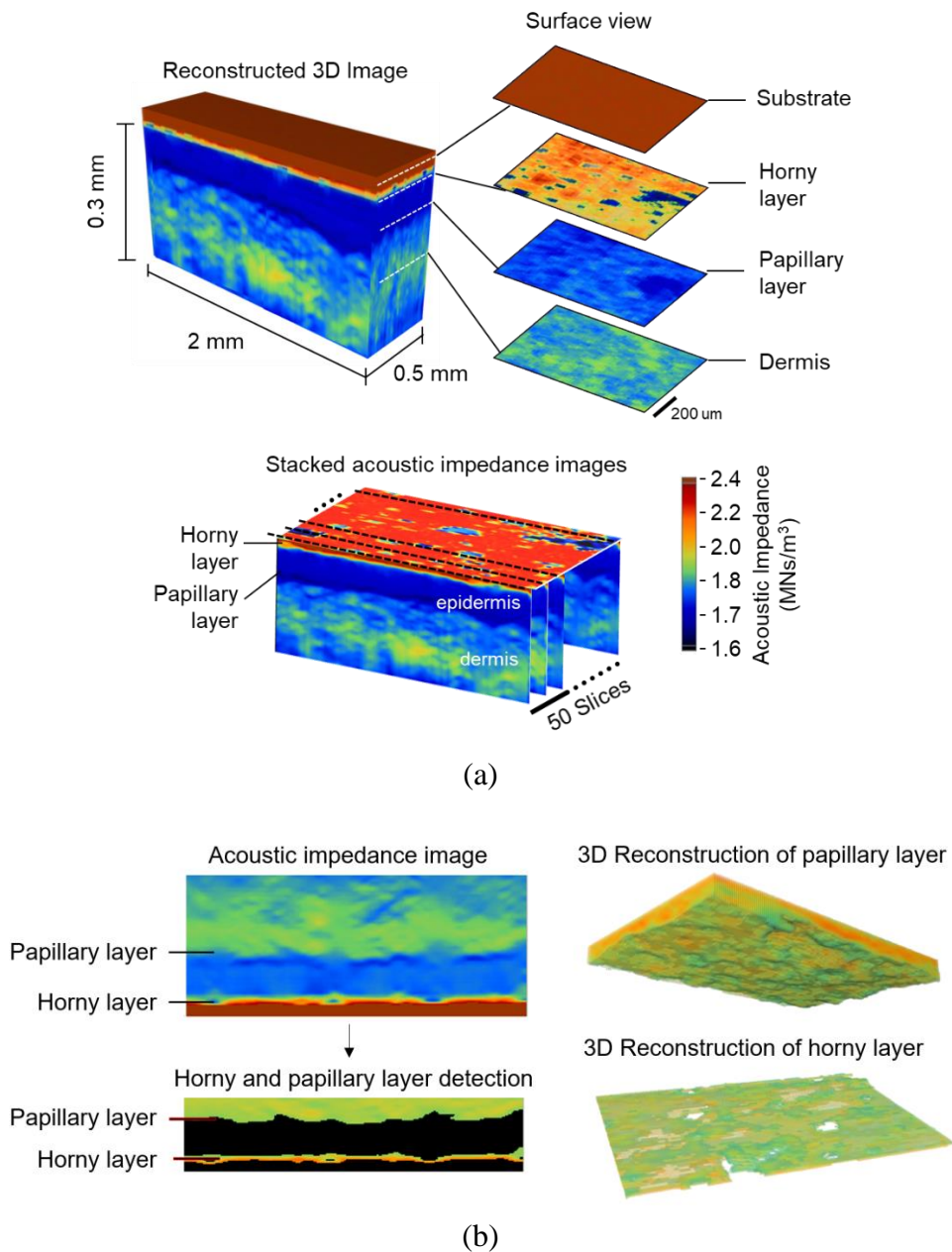
In contrast, the result of the dual-domain deconvolution with the added DC component in the transfer matrix has a much more stable and flatter trend. The difference between the dermis and the epidermis can also clearly be seen in the acoustic impedance image. It can be concluded that the addition of small amount of DC component into the time domain calculation could

stabilize the trend of the deconvoluted signal.

In this calculation, the existence of multiple reflections inside the tissue are not taken into the calculation because its intensity will be really small. An angle compensation calculated from numerical sound field analysis is also applied to compensate the oblique incidence of the ultrasonic beam when propagating through the substrate^{24),81)}.

4.8. 3D skin reconstruction from the calculated acoustic impedance images

Figure 4.9 (a) shows the 3D reconstruction of the human cheek skin calculated from as much as 50 cross-sectional slices. Figure 4.9 (b) shows the process of reconstructing the horny and papillary layers from the acoustic impedance image.



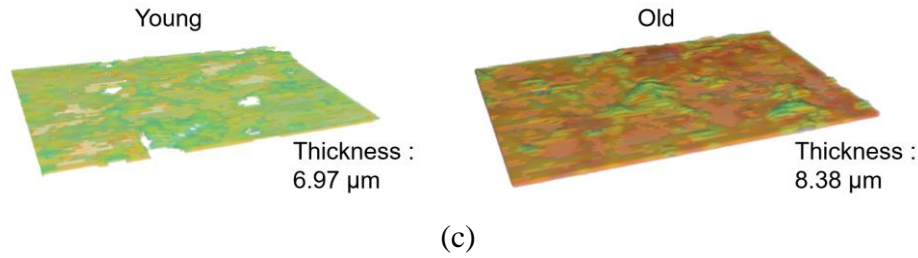


Figure 4.9. (a). The 3D reconstruction of human cheek skin (the shown result was taken from a woman at her 20s); (b). The process of detecting the horny and papillary layer; (c). The horny layer reconstructed from young and old women.

Normally, the horny and papillary layers are detected by specifying a threshold value on the acoustic impedance image before the reconstruction process. In this study, the detection is performed by using a neural network with pixel location and acoustic impedance value used as the input of the network with three hidden layers. Figure 4.9 (b) (right) shows the reconstruction process of the horny and papillary layers.

Figure 4.9 (c) shows the difference of horny layer calculated from the young subject (a 20 years old woman) and old subject (50 years old woman). It appears that the horny layer calculated from the older woman is slightly thicker and rougher than the younger one. This is confirmed with the result of the thickness calculation, with older woman has an average thickness of 8.38 μm while the younger one has an average thickness of 6.97 μm. However, at this moment, only two data from different subjects (person) were reconstructed. In order to increase the confidence of this result, a lot of skin data from a lot of people are required for further observation.

4.9. The relation between the depth-specific elastic properties and the generation of wrinkles in the skin

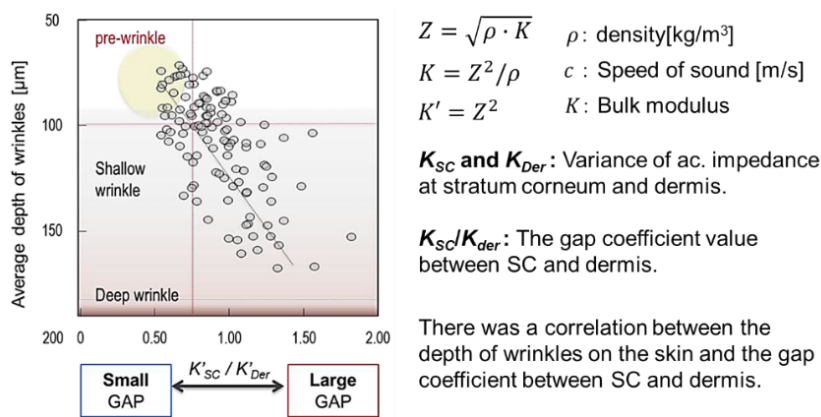


Figure 4.10. The depth of fixed wrinkles correlated with the gap coefficient value⁷³⁾.

As stack of cross-sectional acoustic impedance images could successfully be obtained, the correlation between the age and formation of wrinkle in the skin in different generation was

performed⁷³). The wrinkles easily appear during the facial expressions and based on the simulation result; it also shows that the viable epidermis only contributes a little in the formation of wrinkles. On the other hand, the stratum corneum and the dermis affect wrinkle formation as they become stiffer and softer, respectively. The gap coefficient between the relative elastic properties of the stratum corneum (K'_{SC}) and dermis (K'_{Der}) which is defined as K'_{SC} / K'_{Der} . As the coefficient gets larger, the wrinkles will easily to appear.

Figure 4.10 shows the significant correlation between the depth of the wrinkles and the gap coefficient value (K'_{SC} / K'_{Der}). The wrinkles whose depth is less than 100 μm which is almost invisible is defined as pre-wrinkles with gap coefficient value that is less than 0.75.

4.10. Discussion

Since the error remains stable when increasing the level of frequency bin (number of subjected low-frequency components) above the threshold limit in the dual-domain calculation, this means that the deconvolution in the frequency domain is actually not necessary and that the calculation can all be performed only in the time domain. This is equivalent to setting the border frequency at the Nyquist frequency. However, in such a case, the time of calculation increases and the processing time becomes long, so down-sampling is performed prior to the time-domain deconvolution in order to reduce calculation time. This (down-sampling) will limit the frequency band after time domain deconvolution. The reduced frequency components can be recovered by performing the calculation of the frequency band higher than the limit frequency (in the frequency domain) and then complementing the result. When the S/N ratio of the low-frequency component of the signal becomes small, low-frequency spurious (artifact) occurs after the deconvolution process, but in the pulse response measured here, the frequency at which this occurs is far from the center frequency (70 MHz, in this particular experiment), and is equivalent to a few cycles along the time window. In this experiment, this criterion was as low as 15 MHz. If the threshold frequency is set slightly higher or lower than the above-mentioned limit frequency, almost the same result will be obtained. Therefore, the result is very insensitive to the threshold frequency and does not require critical tuning.

During the process of acoustic impedance conversion, the sound speed inside the tissue is assumed to be uniform, that is 1600 m/s ^{(42), (43), (71)}. This assumption will not significantly affect the acoustic impedance value because it will only affect the scale of the pixel along the beam direction by around 10%. On the generated acoustic impedance image, only 65% area of the dermis is reliable, in terms of its acoustic impedance value. The precision of the acoustic impedance will be less reliable when it goes deeper from the dermis. This phenomenon can be caused by the integration of error when the calculation goes deeper. However, since the difference between the horny layer, papillary layer, and some part of the dermis could successfully be seen, at this moment, this condition is considered to be acceptable.

On the reconstructed horny layer from two different subjects (young and old), it is shown that the older subject has a slightly thicker and rougher horny layer compared with the younger ones. In order to support this statement, many datasets from many subjects with various ages (from 20 – 50 years) need to be observed. In addition to that, the parameters such as the application of cosmetics and the living area of the subjects need to be taken into account, which can be the continuation of this study in the future.

4.11. Conclusions

Three-dimensional acoustic impedance microscopy was proposed and applied to human cheek skin. A newly proposed dual-domain deconvolution was applied for estimating the reflection coefficient in time domain that comes back from each internal layer in skin structure. In order to perform the 3D analysis, all the cross-sectional slices in the measurement area need to be calculated. In that case, the parameters such as the calculation time and the number of appended low-frequency components into the calculation was discussed.

There was an optimal condition in the down-sampling level that is corresponded to the border between time-domain and frequency-domain deconvolution. If the border frequency is high, it may need a long calculation time. On the other hand, if the border frequency is low, the baseline may be unstable because of low-frequency spurious that derives from the frequency domain deconvolution.

In addition to that, in order to improve the robustness of the dual-domain algorithm when calculating the stack of acoustic impedance images, a small number of DC component is subjected into the transfer matrix that is created from the reference signal. This insertion of DC component in reference signal will cancel the offset that originally exists in the target signal, which can be caused by several factors during the measurement, such as the movement of the subject or the vibration generated by the scanning motor. As the result, the stability of the reconstructed waveform could be maintained. Statistical analysis using the kurtosis calculation of the reflection coefficient waveform was performed in order to evaluate the stability of the baseline. It was found that the dual-domain deconvolution process with subjected DC component in the transfer matrix led to the best result in comparison with two different ways of deconvolution processes.

As the result, a 3D reconstruction of the human cheek skin could be generated, and the shape estimation of the horny and papillary layer, as well as the thickness estimation of the horny layer could be estimated. This series of studies is believed to be useful for skin observation and analysis through its acoustic parameters, although in the future, the quantitiveness of the result may need to be improved.

Chapter V

Precise Cellular-sized Observation by Acoustic Impedance Microscope

This chapter of the study will discuss about the application of the proposed dual domain deconvolution to observe the dynamism of cultured cell. The observation target are Glial cell and Fibroblast cell. The chapter begins with the discussion about the system setup, the additional components for the measurement and the signal processing. As the result, the comparison between the conventional frequency domain deconvolution method and the proposed time and frequency (dual) domain deconvolution in terms of cross-sectional view of the cell will be presented. Moreover, the position of nucleus and the change in the properties of the cell such as height and shape after some treatment (fixation) will also be discussed.

5.1. Ultrasound imaging for cultured cell observation

In terms of biological cell observation, the acoustic microscope had been utilized to extract some acoustic parameters of the cell such as sound speed, thickness, attenuation and also acoustic impedance^{3),27),28),38)}. The change of those parameters after some treatment performed to the cell such the addition of drugs became the main concern of why this field of study is becoming popular^{29)–31)}. Most of the observation utilized the C-mode view of the cell which normally provides information such as shape and also the position of some specific parts of the cell such as nucleus or cytoskeleton.

The number of researches that utilizes ultrasound microscope to observe the cross-sectional view of the cell along the beam direction (B-mode) is still very limited. This is mainly because the structure of the cell that is too thin and this will complicate the signal processing process. However, although the cell is thin, it still has a three-dimensional structure. The evaluation is normally terminated at displaying the RF signals along the scanning direction. This view does not provide meaningful information except the position of the cell. In addition, the image is only contrasted by the intensity of the reflected waveform (not quantitative). It is similar with the problem in skin observation where the reflected waveform captured from the measurement system is a natural convolution between the reflection coefficient coming from the cell and the signal components that comes from the system transfer function. In order to extract the cell information from the naturally convoluted waveform, the deconvolution process is required. In 2018, Hozumi et al. proposed a three-dimensional observation of Glial cell^{42),43)}. The internal reflection of the cell is reconstructed by deconvoluting the target signal (signal coming from the interface between the substrate and the cell) by reference signal (signal coming from the interface between the substrate and water) in frequency domain. The result was then quantified by converting each reflection coefficient into the distribution of acoustic impedance and cross-sectional acoustic impedance image of the cell could be obtained, as shown by Figure 5.2.

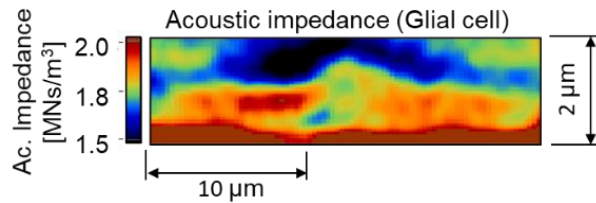


Figure 5.1. The cross-sectional acoustic impedance image of Glial cell; Hozumi et al.

However, as previously described in the skin observation, frequency domain deconvolution will result in an unstable waveform and lead to the generation of artifact when it is converted into the acoustic impedance distribution. As shown by Figure 5.1, some artifact still appears in the upper left and right of the image. This study will propose the solution to above problem by performing deconvolution in both time and frequency (dual domain). In addition, since the stability of the calculation is improved, the three-dimensional analysis of the cell can be performed and the change in cell properties after some treatment (cell fixation) such as the change in height and morphology of the cell will also be provided.

5.2. The objective of cell observation

During the cell monitoring process, some specific drugs are introduced into the cell. These drugs have various purpose such as to stimulate the cell to be more active so that it can easily be tracked or even to slow down the internal process inside the cell (cell becomes inactive). In addition, some cells will die after the addition of specific drugs. The observation by using light microscope cannot track the change in the cell properties after a drug is added. Normally, it can only be used to see the condition of the cell before and after the drug is added.

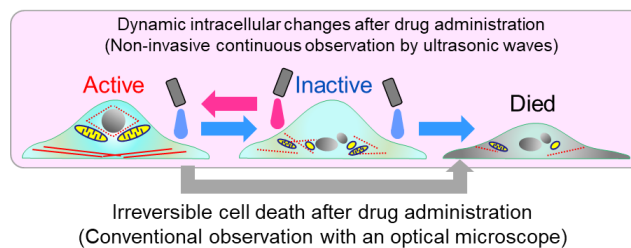


Figure 5.2. The change in cell after the addition of drug.

As illustrated by Figure 5.2, the condition of the cell as it will become more active, inactive or die depends on the types of drugs that is added. The transition phase of the cell from active to inactive (and vice versa) or from inactive to die cannot be tracked by using light microscope. On the other hand, by using ultrasound imaging, this transition phase can be tracked by means of the change in its acoustic properties (such as acoustic impedance). In addition, by performing cross-sectional observation, the change in height and shape of the cell after the addition of drug can also be tracked. This type of observation will help us to understand more about the dynamism of cultured cell.

5.3. System setup

Figure 5.3 shows the system setup for the cultured cell observation. The cultured cells were placed on a thin polypropylene film substrate with a thickness of approximately $75\ \mu\text{m}$. Pure water (with speed of sound of $1480\ \text{m/s}$) was employed as coupling medium between transducer and the substrate. The transducer transmits a focused ultrasound beam with the frequency of $320\ \text{MHz}$. The reflection from the object was then received by the same transducer. The transducer was controlled by the piezoelectric stage to scan the object along the x - and y -axes. The size of the scanned area was approximately $65\ \mu\text{m}$ and consisted of 200×200 points (x and y resolution) with a waveform size (t resolution) of 200 samples with a sampling interval of 200 ps.

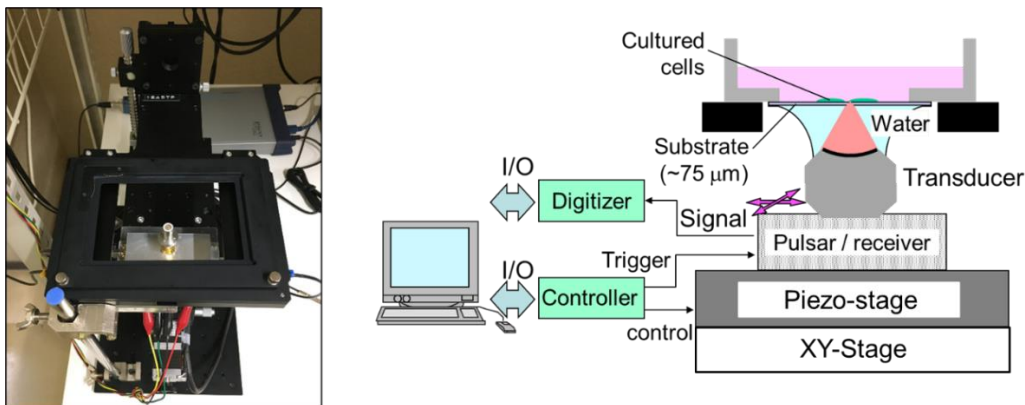


Figure 5.3. The setup of the system for cultured cell observation.

Since cultured cell is very thin, normal mechanical stage will not provide a good lateral resolution during the scanning process. In order to solve that problem, a high-resolution stage (Piezosystem PXY200SG) is employed in the system, as shown by Figure 5.5 (a). Piezo stage provides scanning resolution up to $4\ \text{nm}$ and it also has high dynamic range. Moreover, since it does not rely on mechanical action, the scanning process can be made much smoother compared to the normal mechanical stage.

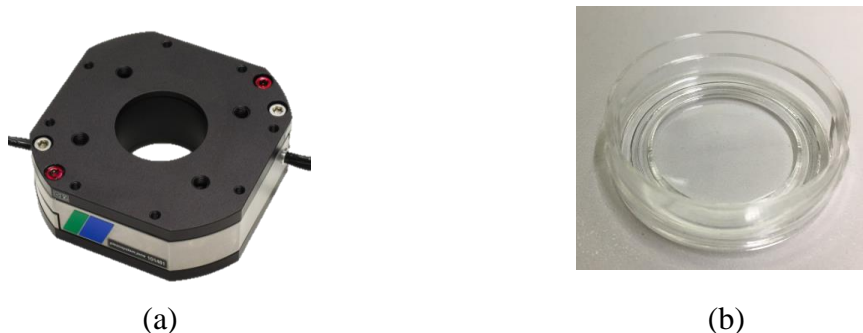


Figure 5.4. (a). Piezo stage for high accuracy scanning and (b). the culture dish.

As a media to culture the cell, a culture dish made of polypropylene film substrate is employed in the measurement. The substrate dish has a center thickness of approximately $75\ \mu\text{m}$

and the diameter of 2 cm, as shown by Figure 5.5 (b). There are two types of cells that are used for the observation. Glial cell and Fibroblast cell are chosen to be the experiment target because they have a rigid cytoskeleton and they also attach well on the film substrate. The Glial cells were cultivated from the neonatal rat cerebellum. In brief, anesthetized neonatal rats were dissected, and the cerebellum was removed. Approximately 100–150- μm -thick slices of the cerebellum were placed into a polypropylene dish.

On the other hand, the Fibroblast cells were purchased commercially (DS Pharma Biomedical, Japan). The cells are then placed into a polystyrene dish and cultured with phosphate buffered saline (PBS) solution. After the first observation by using the ultrasound microscope, the cells are then fixed by using Formaldehyde solution and the second observation is performed. The experimental procedures had been approved by the committees for the use of animals in Toyohashi University of Technology, Japan.

5.4. Transducer specification

Figure 5.4 shows the transducer employed in the ultrasonic microscope for cell observation. The transducer transmits a focused ultrasound beam with a center frequency of approximately 320 MHz. A sapphire lens of half curvature of approximately 60° is attached to the transducer, with radius and aperture diameter of 0.25 mm and 0.41 mm, respectively.

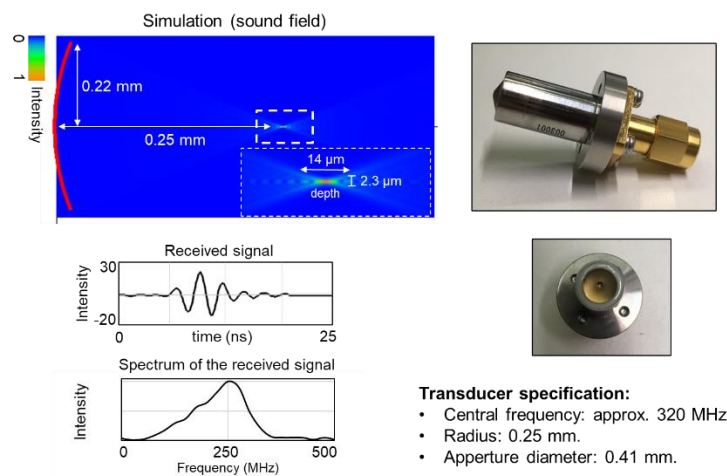


Figure 5.5. The specification of the transducer.

In the calculated sound field distribution of the transducer, the axial and lateral resolution of the transducer are calculated as approximately 14 μm and 2.3 μm , respectively.

5.5. Acoustic impedance interpretation

In order to interpret the obtained impulses (as a result of deconvolution) into the distribution of acoustic impedance, the reflection coefficient was assumed to be a lossless transmission line, and a time-domain algorithm inspired by the method to analyze the reflection waveforms in a transmission line, i.e., Time Domain Reflectometry, was applied and the border of the

transmission line is assumed to be water^{42),43),71),72)}. The algorithm works by calculating each frame of the impulses signal into the acoustic impedance by making use of its previous frame value.

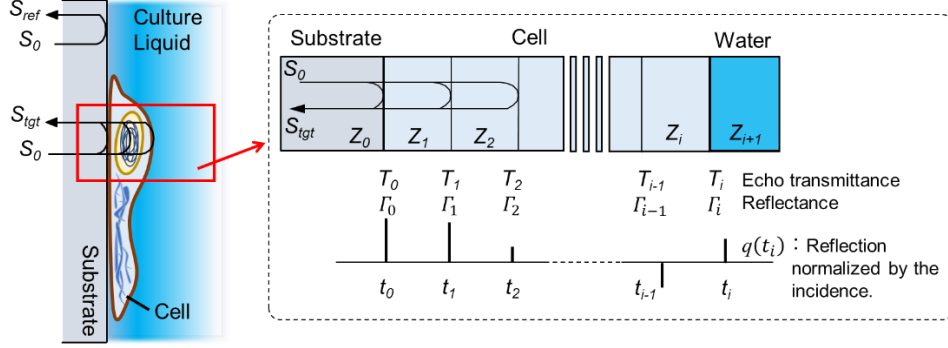


Figure 5.6. The acoustic impedance interpretation when multiple reflections are neglected.

In this study, the calculation for the acoustic impedance interpretation is simplified by neglecting the multiple reflections that occur inside the cell, since their intensity is <1% of the second strongest signal or the signal coming from the interface between the outer part of the cell and water I_{i-1} . As illustrated by Figure 5.6, the cell is located between the substrate and the water, where t_i represents the sampling interval between each sample and I_i represents each fragment of the reflection coefficient previously calculated by using time and frequency domain deconvolution.

5.6. Dual domain deconvolution (cell)

The theoretical explanation and the calculation sequence for dual domain is similar to that in skin observation. After performing both calculations in the different domains, a specific threshold is used as a splitting value for both results of deconvolution in the frequency domain. The high-frequency components of the frequency domain deconvolution are combined with the low-frequency components of the time domain deconvolution, as expressed by equation 5.1, with $S_{deconv(\omega)}^{TD}$, $S_{deconv(\omega)}^{FD}$, and $S_{deconv(\omega)}^{TFD}$ are the Fourier transform of the signal calculated by time domain deconvolution ($S_{deconv(t)}^{TD}$), the result of the frequency domain deconvolution and the combined signal, respectively. Where ω and ω_c is the spectrum components and boundary limit (threshold).

$$\begin{aligned}
 S_{deconv(\omega)}^{TD} &= FT(S_{deconv(t)}^{TD}) \\
 S_{deconv(\omega)}^{FD} &= \frac{S_{tgt(\omega)}}{S_{ref(\omega)}} \\
 S_{deconv(\omega)}^{TFD} &= \begin{cases} S_{deconv(\omega)}^{TD} \rightarrow \omega < \omega_c \\ S_{deconv(\omega)}^{FD} \rightarrow \omega \geq \omega_c \end{cases}
 \end{aligned} \tag{5.1}$$

Since the disturbed low-frequency components are replaced with the ones calculated from time domain deconvolution, this will generate an output signal that has a maintained low and high-frequency component without any interference of unwanted DC components.

5.7. The signal processing result (Glial cell)

5.7.1. Waveform comparison between frequency domain deconvolution and dual domain deconvolution

Figure 5.7 shows the waveform calculated by using the frequency domain and time-frequency domain deconvolution method. Figure 5.7 (a) displays the result of the full frequency domain deconvolution method. An unnecessary DC component appears in the signal as the result of improper division in the frequency domain, forming an unstable baseline that disturbs the resulting signal. Figure 5.7 (b) displays the result of the proposed time and frequency deconvolution method. Since the disturbed low-frequency components from the frequency domain deconvolution are restored by the ones from the time domain deconvolution, the resulting signal does not contain unnecessary DC components.

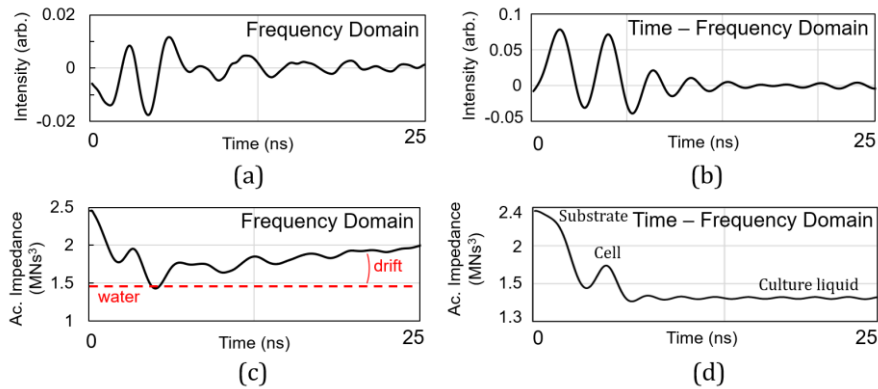


Figure 5.7. The comparison of waveforms as the result of both deconvolution methods.

Figure 5.7 (c) is the result of the waveform after being converted into the distribution of the acoustic impedance. As the frequency domain deconvolution also generates unnecessary DC components in the resulting signal, this creates a significant drift into the acoustic impedance distribution. As shown in Figure 5.7 (c), the value of acoustic impedance increases as more samples are calculated because the next acoustic impedance value depends on the acoustic impedance value of the previous sample, especially in the area outside the cell, i.e., the culture liquid, which should have an acoustic impedance value of approximately 1.52 MN/m^3 . Figure 5.8 (d) is the result of the proposed time-frequency domain deconvolution after being converted into the acoustic impedance distribution. Since the output waveform of the calculation is free from unwanted DC components, no drift in the acoustic impedance result caused by error integration appears in the waveform. In addition, since the acoustic impedance calculation is simplified by ignoring the multiple reflections inside the cell, the resulting waveform exhibits a stable distribution of acoustic impedance. The acoustic impedance of culture liquid, as shown in the

graph of Figure 5.7 (d), also has a similar value with the acoustic impedance of water taken from the reference^(24),78),81). The distribution starts with the acoustic impedance of the substrate dish (approximately 2.46 MNs/m^3) and culture liquid, which has a similar value as that of water (approximately 1.5 MNs/m^3).

5.7.2. Acoustic impedance comparison between frequency domain deconvolution and dual domain deconvolution

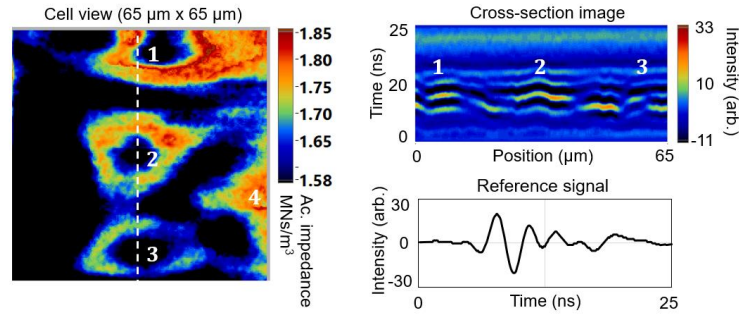


Figure 5.8. The top view of the cell being measured, shown in acoustic impedance and its cross-sectional view on the area sliced by the white cursor.

Figure 5.8 shows the C-mode acoustic impedance image of the scanning area with a size of $65 \times 65 \mu\text{m}$ that consists of 200×200 scanning points. As the result can only display the cell shape and the corresponding acoustic impedance value, it does not provide much information related to the internal structure of the cell. The field of view captured four cells, and the analysis focused on three cells (numbers 1 – 3 in Figure 5.8) because only a small part of the fourth cell is visible.

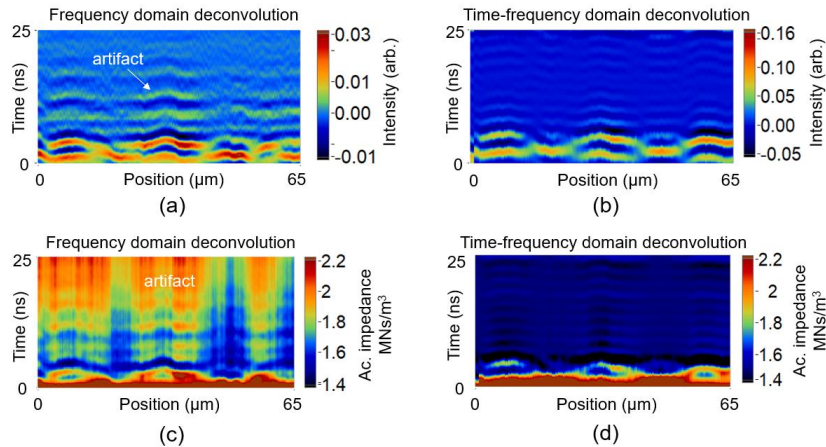


Figure 5.9. The comparison results of the deconvolution and acoustic impedance image. 5.9 (a) and 5.9 (b) are the resulting image from the frequency domain and time-frequency domain deconvolution, respectively. Figure 5.9 (c) and 5.9 (d) are the result of the acoustic impedance image from the frequency domain and time-frequency domain deconvolution, respectively.

Figure 5.9 (a) is a deconvolution image resulting from full frequency domain deconvolution. Since the waveform is disturbed by the baseline, it appears as a strong intensity shown by the wavy green color in the culture liquid area in the image. Figure 5.9 (b) is a deconvolution image resulting from the proposed time-frequency deconvolution method. Some artifacts caused by the DC components in the signal do not appear in this result, as the area above the cell is represented by almost a uniform distribution.

Figure 5.9 (c) shows the result of the frequency domain deconvolution after conversion into an acoustic impedance image. The baseline that appears in the signal (the green color in the deconvoluted image) becomes a very robust artifact in the acoustic impedance image, especially in the area of the culture liquid. This result also shows that the value of acoustic impedance becomes less reliable with increasing distances from the substrate, and is mainly caused by the error integration during the calculation. In contrast, Figure 5.9 (d) is the result of the proposed time-frequency deconvolution after conversion into an acoustic impedance image. Since the deconvolution result is free from unwanted DC components, the acoustic impedance value is well distributed. Unlike the result of the full frequency domain deconvolution method, the area above the cell is free from artifacts and corresponds to the acoustic impedance of the culture liquid, which is approximately 1.52 MNs/m^3 . In addition, the proposed method can also maintain a stable acoustic impedance distribution along the distance from the substrate.

5.7.3. Analysis of cell structure based on the acoustic impedance image

Although three cells were observed in the scanning area (Figure 5.8), the clearest view of the nucleus position in terms of depth was located on cell number 2, which was thus selected for further analysis. Cell number 2 was cropped into an area of $25 \times 25 \mu\text{m}$ (Figure 5.10).

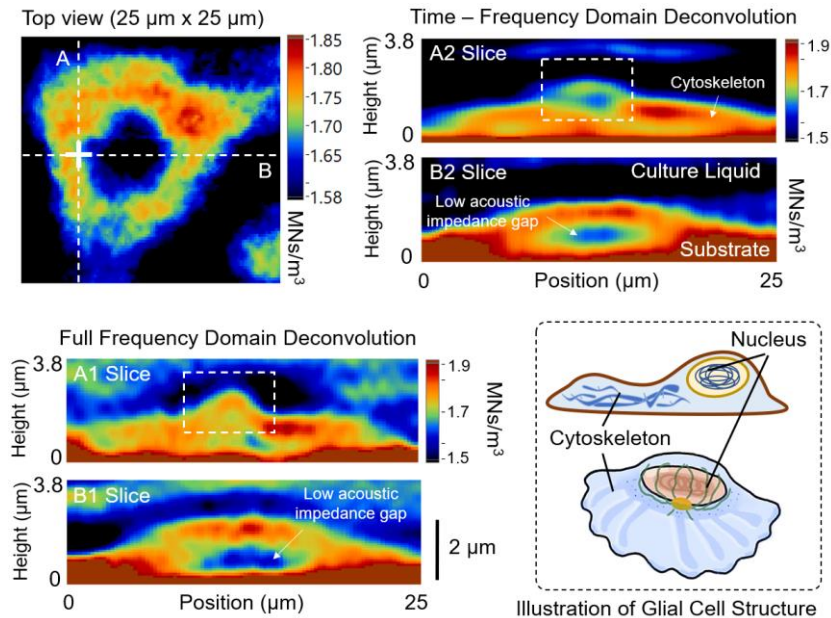


Figure 5.10. The result of acoustic impedance profile as well as the estimation of the Nucleus position based on the cross-sectional view of the cell by using the frequency domain and time-frequency domain deconvolution.

The radius of the cell was approximately 10 μm , and since the sound speed inside the tissue is assumed to be constant (at 1600 m/s), the height of the cell was estimated at $\sim 2 \mu\text{m}$. Cursors A and B correspond to the vertical and horizontal view of the cell, respectively. The plus sign between the two cursors represents the estimated location of the nucleus. Examination of the A1 slice as the result of the full frequency domain deconvolution revealed that the bottom of the cell, especially at the substrate, exhibits a wavy pattern and that the relief of the substrate is not flat. The artifact on the top of the cell can also still be seen with an acoustic impedance value higher than that of the culture medium. The white square represents the estimated location of the nucleus. The nucleus exhibits a similar value of acoustic impedance as other parts of the cell, i.e., the cytoskeleton.

Unlike the result of full frequency domain deconvolution, the A2 slice calculated by using the proposed time-frequency domain deconvolution exhibited a different structure. The cell was rounder and the substrate appeared smoother; thus, the cell appeared to be in perfect contact with the substrate. In addition, the artifact on top of the cell was not as visible and strong as the one from frequency domain deconvolution (A1 slice). The area inside the white square (estimation of the nucleus position) exhibited a lower acoustic impedance distribution (at 1.5–1.6 MN/m^3) compared to that of the other parts of the cell. This suggests that the proposed method can distinguish between the nucleus and other parts of the cell, not only in terms of acoustic impedance value but also in terms of cell shape. The B1 and B2 slices calculated by using the full frequency domain and proposed time-frequency deconvolution, respectively, however, do not exhibit significant difference in terms of the shape or acoustic impedance distribution. The similarity of both results is that there appears to be a gap with low acoustic impedance on the bottom part of the cell. However, unlike the B2 slice, the B1 slice calculated by full frequency domain deconvolution still exhibits clear artifacts on the top of the cell that disturbs the distribution of the culture liquid area.

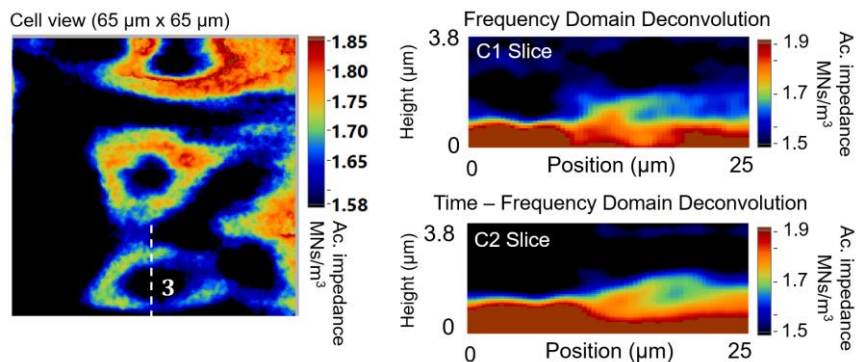


Figure 5.11. The cross-sectional view of the cell 3 sliced at vertical direction and its corresponding result calculated by the fully frequency domain and the time-frequency domain deconvolution.

Cell number 3 was also sliced in the vertical direction (Figure 5.11). The C1 slice reveals that the frequency domain deconvolution is unable to retain the shape of the cell as it gradually spread and mixed with the area of culture medium. The artifact on the top of the cell can also still be seen (light blue color). Unlike the C1 slice, the C2 slice resulting from the proposed time-

frequency deconvolution can maintain the shape of the cell without any artifacts on the top of the cell. Furthermore, a substance with a low acoustic impedance on the top of the cell was observed with properties that were very similar to the nucleus, as previously discussed (Figure 5.10).

5.8. The signal processing result (Fibroblast cell)

5.8.1. 3D analysis of Fibroblast cell

Figure 5.12 shows the result of the proposed dual domain deconvolution to the dataset of Fibroblast cell. The area marked by yellow-dashed line is shown on the one-dimensional graph on the right. On the RF b-mode image, the position of the cell is hardly recognizable. This is because the reflection coming from the cell is convoluted naturally with the reflection coming from the system transfer function.

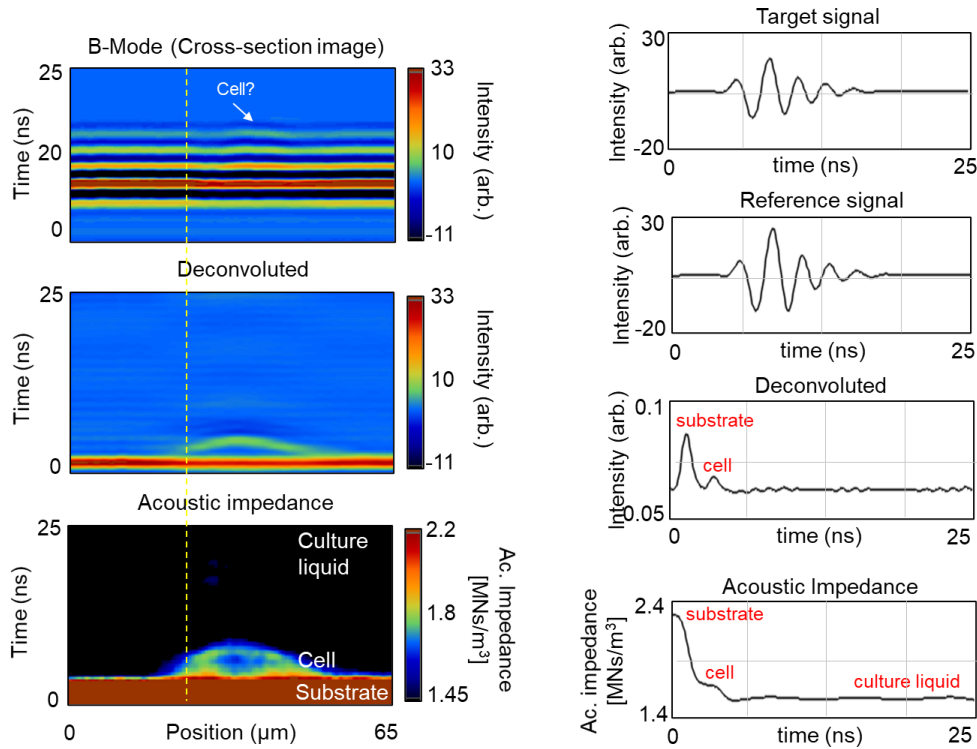


Figure 5.12. The signal processing result (dual domain deconvolution) of Fibroblast cell.

By deconvoluting each signal in the RF b-mode image with the reference signal (signal coming from the interface between substrate and water), the location and shape of the cell becomes visible, as shown by the deconvoluted image. Since the baseline is stable the distribution of acoustic impedance between substrate, cell and culture liquid becomes distinguishable. Since the cell is located between substrate and culture liquid which acoustic impedance are known, its acoustic impedance can be verified.

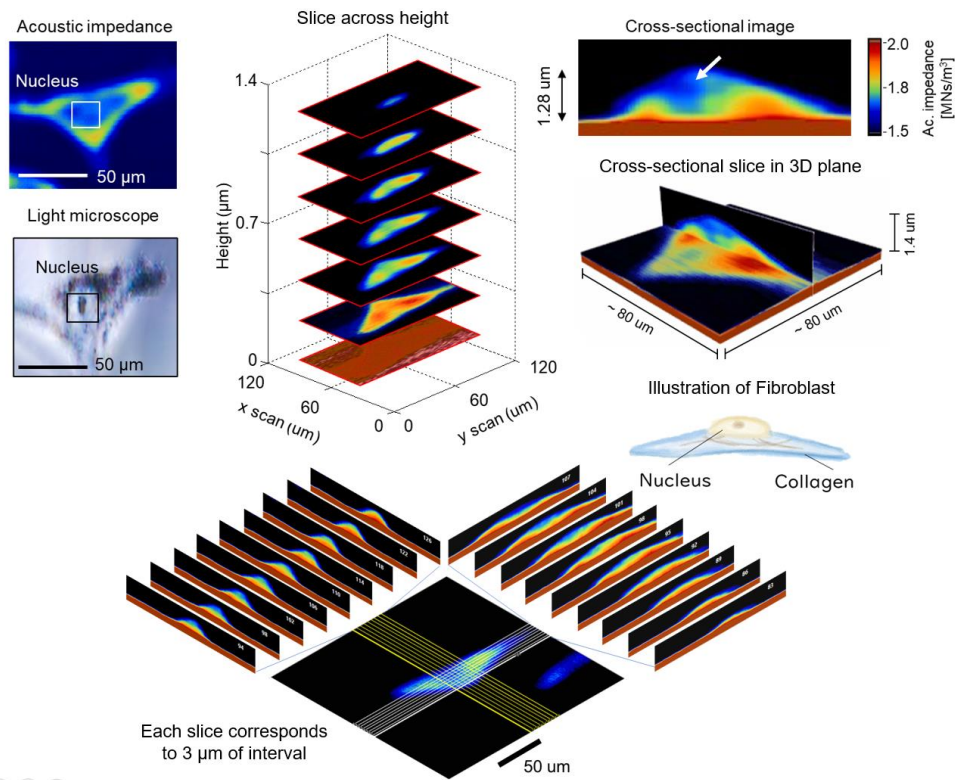


Figure 5.13. Three-dimensional analysis of Fibroblast cell (fresh).

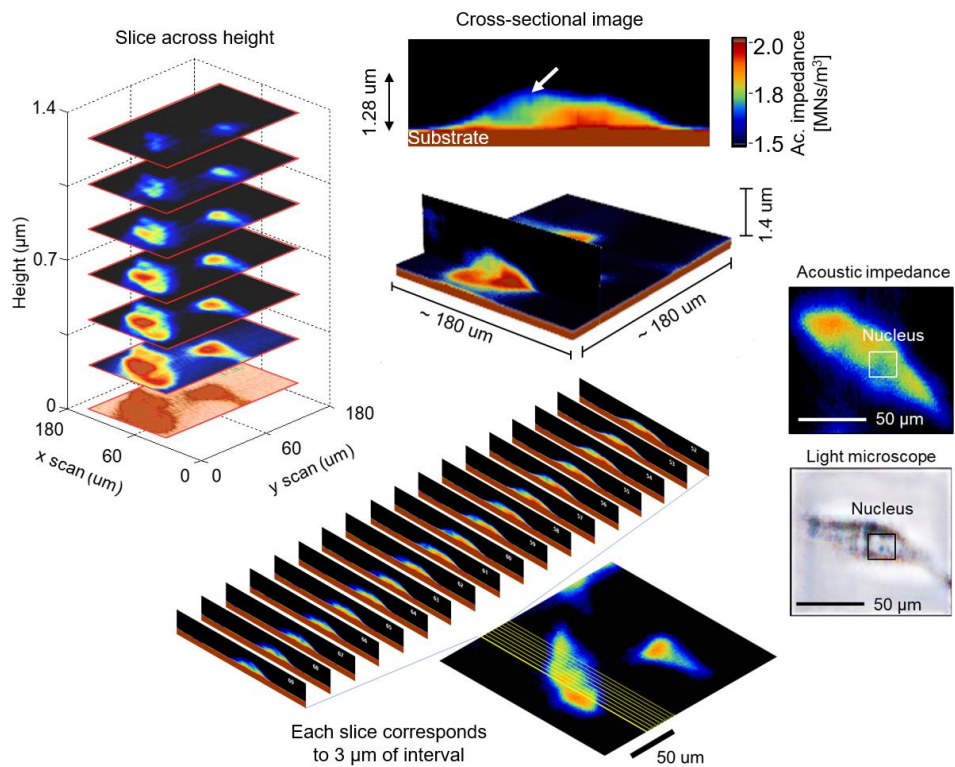


Figure 5.14. Another three-dimensional analysis of Fibroblast cell (fresh).

Figure 5.13 shows the result of performing 3D analysis to the Fibroblast cell. Since the proposed acoustic impedance microscope can perform a measurement without introducing any contaminants, a living observation of the cell could be performed. As all cross-sectional acoustic impedance images are stacked, the view of the cell that is reconstructed from calculated acoustic impedance distribution in the 3D plane can be observed. In addition, the cell can also be sliced from all cross-sectional directions, enabling us to see some specific part of the cell.

In the calculated cross-sectional acoustic impedance image, there is an area with low acoustic impedance on the center part of the cell that is believed to be where the nucleus is located (indicated by white arrow). Although it is not easy to locate the position of the nucleus in the cross-sectional image, the corresponding area in light microscope image (as indicated by black-rectangle) and C-mode acoustic impedance image shows where the nucleus is located.

Figure 5.14 shows another 3D observation for another Fibroblast dataset. This view captured as many as two Fibroblast cells in the measurement area. Similar with the result shown by Figure 5.14, there is an area that is believed to be the nucleus that is indicated with low acoustic impedance (shown by white arrow).

In addition, by using the 3D analysis, specific parts of the cell can freely be observed because we have the freedom to slice the cell in all directions. However, since the resolution of the image taken by light microscope is poor, it is quite difficult to locate the precise location of some specific parts of the cell and in conjunction with that, it may be required to stain the cell by staining solution such as DAPI, which process will be described in the next sub-chapter.

5.8.2. Cell dyeing (staining by DAPI)

Dyeing or staining cell is a process to contrast the internal structure of the cell such as nucleus to be visible by injecting a dyeing solution DAPI (4',6-diamidino-2-phenylindole) which is a fluorescent stain that binds strongly to adenine–thymine-rich regions in DNA into the cell, as the process is shown by Figure 5.15. Because even after 3D acoustic impedance analysis was successfully performed, it is still hard to compare the position of the nucleus inside the cell because the resolution of the image taken by light microscope is poor.

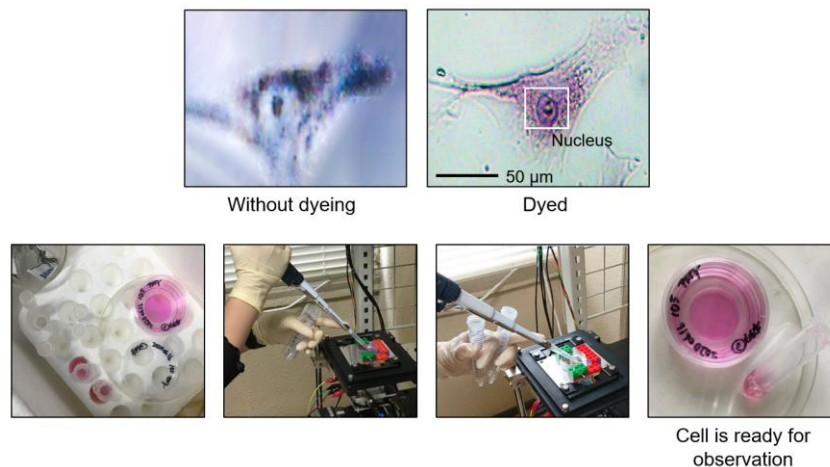


Figure 5.15. The difference between the cell before and after dyeing process.

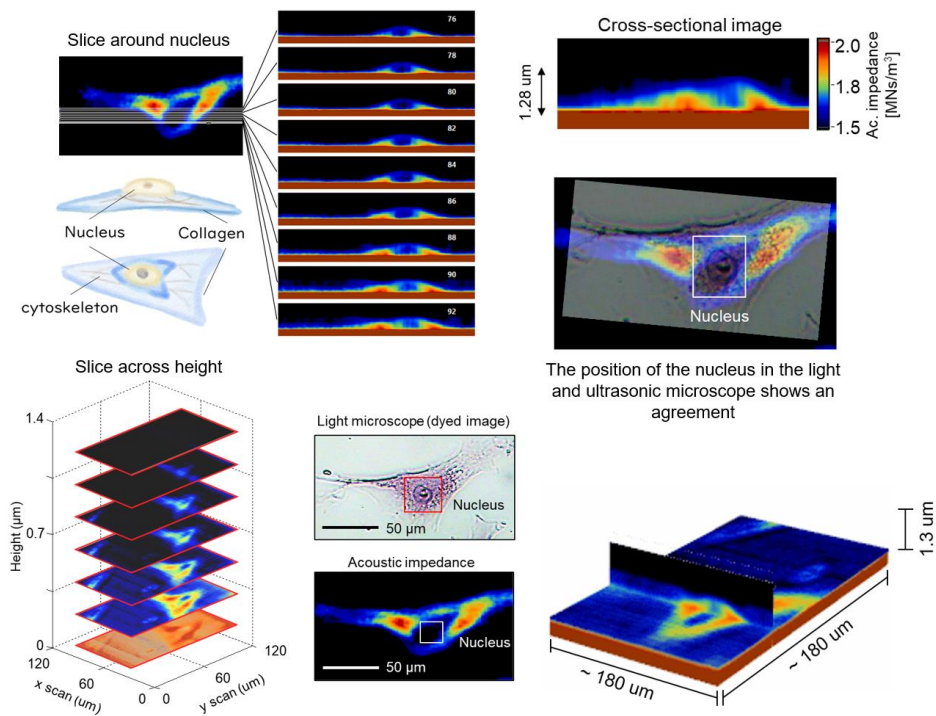


Figure 5.16. Three-dimensional analysis of Fibroblast cell after staining is performed; The nucleus in light microscope image becomes clearly visible after staining.

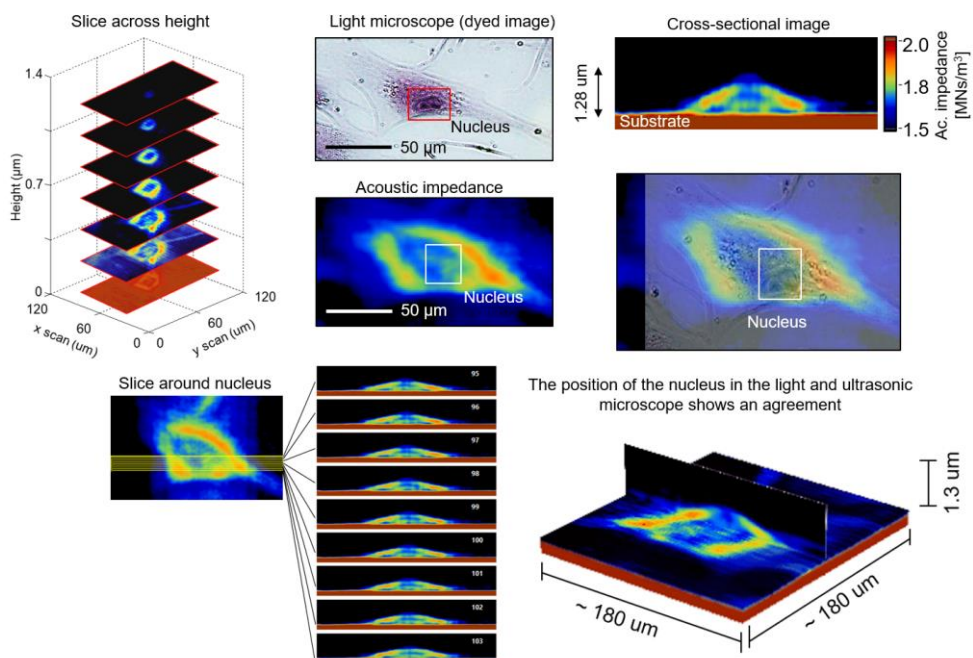


Figure 5.17. Another three-dimensional analysis of Fibroblast cell (another cell dataset) after staining is performed; The nucleus in the light microscope image becomes clearly visible after staining.

As shown by Figure 5.15, the nucleus and other parts of the cell in the light microscope image becomes clearly visible after staining is performed. However, since staining process will kill the cell, it will make a living observation of the cell is no longer possible to carry out.

However, this process is done in order to confirm the parameter that had previously been found in the 3D analysis, such as if the area that is believed to be the nucleus really is located near the center part of the cell. Figure 5.16 shows the Fibroblast cell after staining process is carried out. When all the calculated cross-sectional acoustic impedance images are stacked, the 3D analysis of the cell could be performed. The cell shown in Figure 5.16 is the same cell used in the observation in the Figure 5.13, however, this time, the cell is dead because of the staining process. As shown by Figure 5.16, the position and shape of the nucleus in the optical image becomes clearly possible after staining process. The result of another stained cell is also shown in Figure 5.17.

Since the cell is dead during observation (because of DAPI injection into the cell) some acoustic parameters inside the cell may slightly change. However, this method is at least able to help to confirm the position of some specific parts of the cell such as nucleus when observed by both light microscope and acoustic impedance microscope.

5.8.3. The change in properties of the cell (height and shape) after some treatment to the cell (fixation)

5.8.3.1. The change in height

Since the stability of the calculation has been retained by the proposed method, the change in properties of the cell after some treatment such as fixation is carried out to the cell can also be monitored. Generally, fixation is performed in order to lock the position of the cell during observation. This enables us to move the cell during observation by using various microscopes. 4% of Paraformaldehyde or better known as PFA solution is normally used as the fixation medium. However, similar with the staining process, the cell will no longer live after fixation process is performed. The procedure for cell fixation is described as follows:

- a. The fresh cell is observed by using acoustic impedance microscope and at the same time, same position of the cell is also captured by using light microscope. Extra care may be required because when the cell is fresh, a strong movement when moving the dish by hand may change the position of the cell.
- b. The cell is then fixed by using the PFA solution. It may be required to wait for some time (approximately 40 minutes – up to 1 hour) until the cell is perfectly fixed.
- c. The cell is observed again by using ultrasound microscope and light microscope. The image and data and then analyzed and compared.

Figure 5.18 shows the process of estimating the height of the cell from the deconvoluted signal. After the deconvolution process, two peaks appear in the deconvoluted waveform. One indicates the reflection from the substrate (shown by strongest peak) and the other indicates the reflection coming from the cell. Sometimes, the gap between these two peaks is not clearly indicated, so peak strengthening method is sometimes required. Conventional peak detection is

then performed to the waveform and since the goal is to extract the shape of the cell, only the second peak is taken into account (first peak is neglected). The comparison of height in the graph shows that there is some reduction in the cell after fixation is carried out. Based on the reference, the cell will lose its mass density by 10% after 17 mins of fixation in 4% of PFA solution⁷⁹⁾, this may become the reason of the reduction in the height of the cell after fixation. When the height in all cross-sectional images along the scan direction are calculated, the result is shown in the 2D mapping of the height (bottom graph). It shows that the height after fixation undergoes a reduction by approximately 0.1 – 0.2 μm .

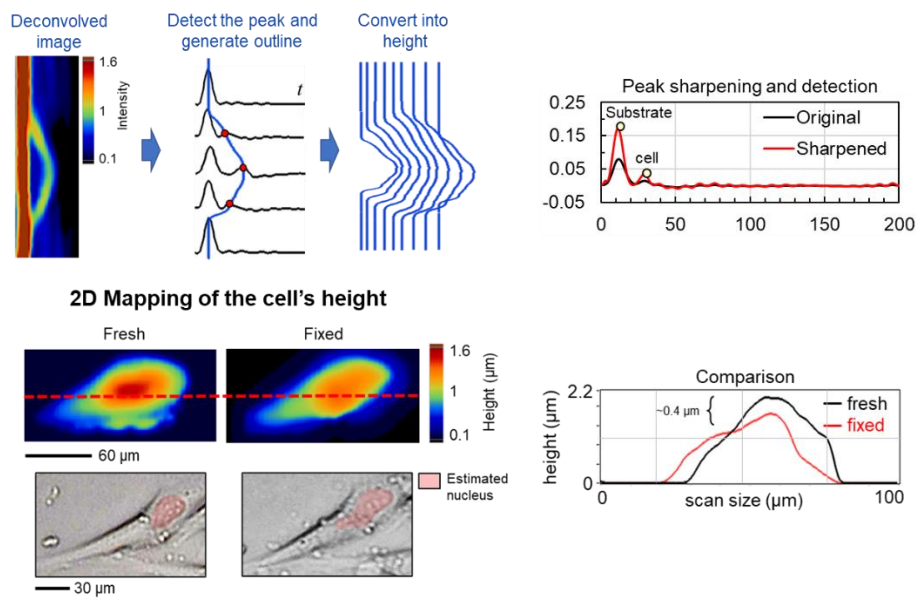


Figure 5.18. The height analysis of the cell calculated from the deconvolved image.

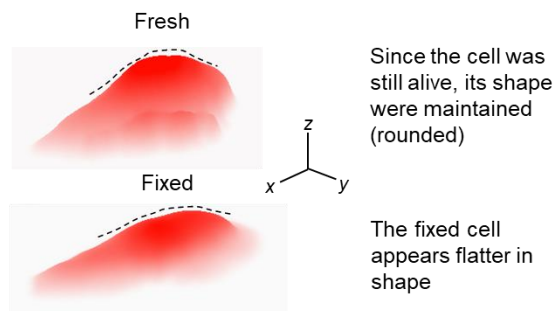


Figure 5.19. The surface graph created from the 2D mapping of the calculated height.

Figure 5.19 shows the surface graph created from the calculated 2D maps of height. As shown by the Figure, the fresh cell tends to have a round shape whereas the cell after fixation tends to have a flatter shape. This may suggest that the track in the cell height can be monitored by using the calculated deconvolution image.

In addition to the change in height, the change in the shape of the cell after fixation can also be monitored. The analysis procedure is similar to the one described in the previous sub-

chapter. Figure 5.20 shows the Fibroblast cell from another measurement dataset. The C-mode and light microscope view capture as much as two cells in the measurement area, as shown by Figure 5.20 (a). The white-dashed line (marked by number 1 and 2) on the C-mode image indicates the location of the cross-section.

Figure 5.20 (b) and (c) show the cross-section acoustic impedance images marked by each white-dashed line before and after the fixation process is carried out. The comparison between the outline of each cell is shown by the bottom graph in Figure 5.20 (b) and (c). Some reduction and changes appear in terms of height and shape of the cells. The cells after fixation also tend to be flatter and their height also decreased.

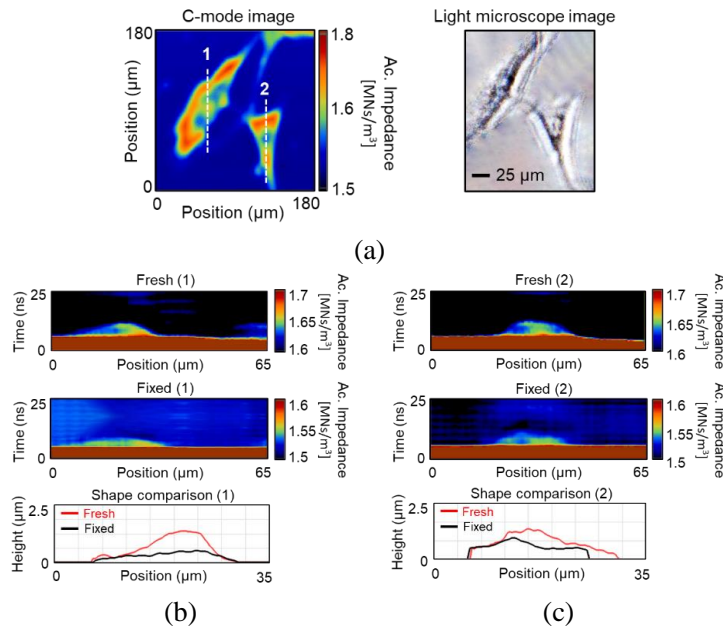


Figure 5.20. The change in Fibroblast cell before and after the fixation process in another dataset: (a). Light microscope image and (b). The comparison of cross-sectional acoustic impedance image and its change in shape.

5.9. Discussion

5.9.1. Dual domain deconvolution for cultured cell observation

During the calculation, the sound speed inside the cell is assumed to be constant at 1600 m/s. In reality, the sound speed inside soft tissue is in the range of 1500–1800 m/s, although this variation of sound speed will not drastically affect the result of the image, it may be considered that the length of each pixel in the acoustic impedance image will be distorted by approximately 10 – 15% because the length of each pixel corresponds to different sound speed c .

Before time-domain deconvolution, both target and reference signals are down-sampled by a factor of n . This process reduces the amount of high frequency components in the signal. If the down-sampling operation is not performed, it is probably not necessary to perform deconvolution in the frequency domain. However, the calculation will take a long time, especially if the sample

length of the signal is large, because the size of the transfer matrix (H) will become large. In this study, the sample length of the signal was not more than 200 samples; thus, the effect of dual domain deconvolution in terms of calculation speed was insignificant. However, the number of samples should be increased in the future to increase the resolution of the signal.

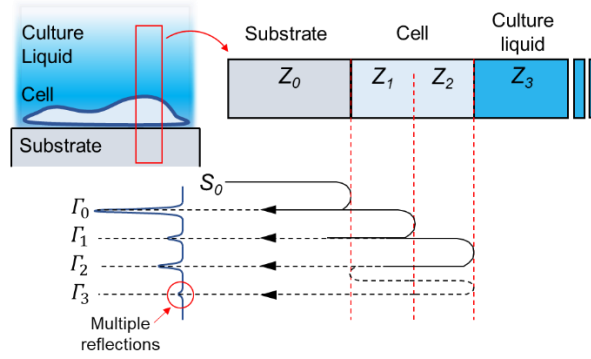


Figure 5. 21. The generation of reflection inside the cell.

Figure 5.21 illustrates the generation of reflections coming from the interfaces between the substrate, cell and culture liquid. Γ_0 is the reflection coefficient coming from the interface between the substrate and the cell. Since the difference of acoustic impedance between the substrate and the cell is high, it will make Γ_0 has the strongest reflection intensity. On the other hand, there are two types of reflections coming from the cell. The first reflection is the one coming from the internal part of the cell (Γ_1) while the second reflection is the one coming from the interface between the outer part of the cell and the culture liquid (Γ_2). The reflection exists in the top of the cell is considered as multiple reflection which intensity is really small (Γ_3). By assuming that the acoustic impedance of the cell is constant, that is 1.8 MNs/m^3 , and by using the acoustic impedance of substrate and water (2.46 MNs/m^3 and 1.52 MNs/m^3 , respectively), the strongest intensity of the multiple reflection (Γ_3) can be calculated by equation 5.2.

$$\begin{aligned} \Gamma_3 &= \left(\frac{Z_{\text{cell}} - Z_{\text{water}}}{Z_{\text{cell}} + Z_{\text{water}}} \right)^2 \cdot \left(\frac{Z_{\text{substrate}} - Z_{\text{cell}}}{Z_{\text{substrate}} + Z_{\text{cell}}} \right) \\ &= \left(\frac{1.8 - 1.5}{1.8 + 1.5} \right)^2 \cdot \left(\frac{2.4 - 1.8}{2.4 + 1.8} \right) \\ \Gamma_3 &\leq 0.0011502 \end{aligned} \quad (5.2)$$

The maximum dynamic range of the multiple reflection in the acoustic impedance image can thus be calculated by utilizing the intensity of the reflection coming from the interface between the outer part of the cell and water (Γ_2), as expressed by equation 5.3. In the result of acoustic impedance image, the acoustic impedance of the cell spreads from the range of $1.5 - 1.8 \text{ MNs/m}^3$, which means that the required dynamic range is approximately 0.3 MNs/m^3 , as shown by Figure 5.22, while the multiple reflection itself is estimated as 0.004.

$$\begin{aligned} \left(\frac{Z_{cell} - Z_{water}}{Z_{cell} + Z_{water}} \right) &= \Gamma_3 \\ &= \left(\frac{1.5 - x}{1.5 + x} \right) = 0.000168 \\ x &= 1.496 \\ range &= 1.5 - 1.496 = 0.004 \end{aligned} \quad (5.3)$$

This means that the intensity of the multiple reflection is really small compared with the reflection coming from the interface between the cell and culture liquid (Γ_2) and its existence can be neglected. In addition to that, even if multiple reflection appears in time domain after the deconvolution process, it will appear as a sequence of gaussian pulse located on the top area of the cell that can be rejected by a window function.

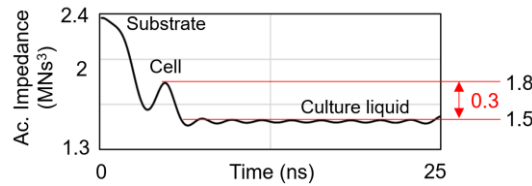


Figure 5.22. The estimation of dynamic range between the cell and culture liquid.

In the acoustic impedance image, it is considered that cytoplasm (indicated with its acoustic impedance that is slightly higher than culture liquid) fills up the whole parts of the cell. The nucleus appears to have a higher acoustic impedance than the cytoplasm is probably because the nucleus has a higher mass density. The acoustic impedance of the nucleus appears to be lower than cytoskeleton is probably because of the high elasticity of the fibres occupying the cytoskeleton (although the boundary between the nucleus and cytoskeleton is not as clear as the optical image after staining).

At the moment, the use of a phantom is considered in order to validate the result of the proposed method. However, since the cell is very thin, it was not easy to produce a well-controlled phantom. Instead, the validity was verified by using the buffer liquid that exists on the top of the cell. After the periodical acoustic impedance conversion along the depth that starts from the substrate, the estimated acoustic impedance should finally reach 1.52 MNs/m³ that is for the buffer liquid (that was verified by the measurement on different content of saline solution^{24),82)} as the result of the repetitive calculation.

In this paper, the internal observation of the cell could be performed because the axial resolution was as thin as 0.2 μm . However, because of the diffraction limit, the lateral resolution was slightly longer than 1 μm . In order to increase the lateral resolution, a transducer with a higher frequency is required, followed by a thinner polystyrene substrate as the focal distance will become shorter. Since a focused high-frequency beam is generated by the transducer, the direction of the beam will no longer be a plane wave and the beam will spread as it propagates through the specimen. In fact, some reflections from the area around the measured point will also be generated. If these reflections are taken into the calculation, and by using an algorithm similar to

a Synthetic-aperture radar (SAR)⁸³⁾, the spatial resolution of the image can be improved. In order to realize it, a robust error correction and precise acoustic field analysis⁸¹⁾ are required.

5.9.2. 3D analysis and the change in cell properties

In the assessment of the cell properties by means of its acoustic impedance distribution, the cell tends to become flatter and has some reduction on its height after the fixation is done. This is because during the fixation process, the culture medium is extracted from the dish and at this stage, the dehydrated cell will lose most of water content inside its body including the cytoplasm and slowly dies. The fixation liquid is then injected into the dish and some penetrates through the cell membrane and at this stage, the cell is already dead, causing the cell to be flatter in shape.

5.10. Conclusion

5.10.1. Dual domain deconvolution for cultured cell observation

A method of deconvolution in the time and frequency domain is proposed to estimate the reflection coefficient that comes only from the cell by using the target and reference signal. Glial cells that were cultured on a substrate dish were the object of measurement. The low-frequency components that were disturbed during deconvolution in the frequency domain were restored and replaced by using the low-frequency components obtained from time domain deconvolution. The combination of the high-frequency components from frequency domain deconvolution and the low-frequency components from time domain deconvolution resulted in a signal with good resolution and without unnecessary low-frequency components. The obtained reflection coefficient was then interpreted into the distribution of the acoustic impedance by using the algorithm inspired by Time Domain Reflectometry. However, in this study, the existence of multiple reflections inside the cells was neglected, and the calculation was simplified.

The results of both frequency domain deconvolution and proposed time-frequency deconvolution were compared and discussed. The distribution of acoustic impedance calculated from the reflection coefficient of the proposed time-frequency deconvolution method remained stable with the distance from the substrate, especially on the area of the cultured liquid, whereas the full frequency deconvolution method generated artifacts on the acoustic impedance image that were caused by error integration during the calculation. Furthermore, the proposed time-frequency deconvolution method could distinguish between the nucleus and other parts of the cell, not only in terms of shape but also in terms of acoustic impedance distribution. The nucleus calculated by the proposed method exhibited a lower acoustic impedance value than other parts inside the cell and is estimated to be located toward the center of the cell.

As the internal structure of the cell has been successfully interpreted regarding its acoustic properties, which may be related to elasticity, this study may be useful to see a large or small relationship of adjacent parts inside the cultured cell.

5.10.2. 3D analysis and the change in cell properties

Since stability of the calculation in dual domain deconvolution could be maintained, a 3D analysis of the cell could be performed and by using the 3D data, the properties of the cell by means of its acoustic properties in the plane direction could be observed. This will enable us to assess the parameter that relates to the cell dynamism, such as the change in height and shape after a specific treatment is performed to the cell (in this study is fixation process).

In addition, by using the 3D acoustic impedance analysis, the position of the nucleus could be confirmed. The result of analysis showed that the nucleus was located near the center of the cell. This was confirmed with the result after staining because the internal parts of the cell became clearly visible (in the light microscope image).

It also shows that the cell underwent some reduction in height by approximately 0.1 – 0.2 μm after fixation process. The cell also tended to be flatter in shape after fixation process was performed. This may suggest that the proposed method is useful to track the change in the cell properties after some specific treatment is carried out and to locate some parts in the cell internal structure such as nucleus and its position along the depth direction.

Chapter VI

The Application of Acoustic Property Imaging for Industrial Applications

This chapter of study will discuss about the application of the proposed dual domain deconvolution signal processing to other ultrasound-based measurement (non-biomedical related research field) such as the coating film monitoring in the automotive industry and the observation of the existence of space charge in the XLPE cable by means of pulse electroacoustic (PEA) method. This chapter will be divided into two independent sub-chapter, started with the coating film monitoring and followed by the space charge measurement.

6.1. Coating film monitoring

The proposed signal processing in this study is also applied to other ultrasound-based measurement system. In the coating film (paint protection) monitoring especially in automotive industry, in order to prevent corrosion and scratches in the car's body. The coating normally consists of several layers, as shown by Figure 6.1. The outermost layer is normally a clear coat which thickness is around 38 – 102 μm and followed by base coat and primer coat.

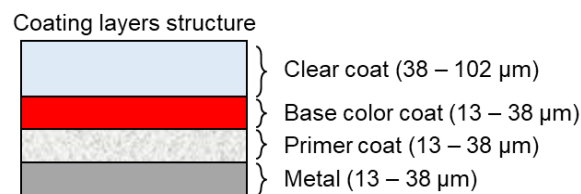


Figure 6.1. The structure of coating film in car.

The conventional method to assess these layers was carried out by emitting a terahertz light into the layers and the reflection from each layer will then be detected. The peaks generated from the interfaces between each layer are then separated and parameter such as thickness of each layer can be calculated, as illustrated by Figure 6.2.

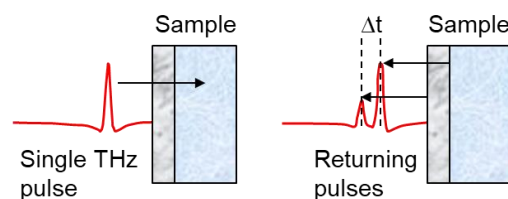


Figure 6.2. The coating film assessment by using terahertz light.

However, this way of measurement has a deficiency that it is quite expensive because terahertz light which requires a laser with high voltage is used. In conjunction with that, this study proposes another alternative method for coating film monitoring by using ultrasound microscope. By emitting ultrasound into the coating layers, the reflection from each layer can be obtained similar to the measurement by using terahertz light. Each individual peak is then separated by performing deconvolution in time and frequency (dual) domain and the parameter such as thickness of each layer can be calculated. Moreover, the result can be quantified by converting each reflection coefficient into the distribution of acoustic impedance and by scanning the object, the two-dimensional view (cross-section) of the layers that is contrasted by acoustic parameter can be obtained. This proposed alternative measurement is believed to be more quantitative and cheaper compared with the conventional one.

6.1.1. System setup

Figure 6.3 shows the system for coating film monitoring in our laboratory. The sample is placed under a mechanical stage. An 80 MHz transducer then transmits a focused ultrasonic beam through the sample and the reflection is captured by the same transducer and by scanning the object, the two-dimensional view of the object can be obtained.

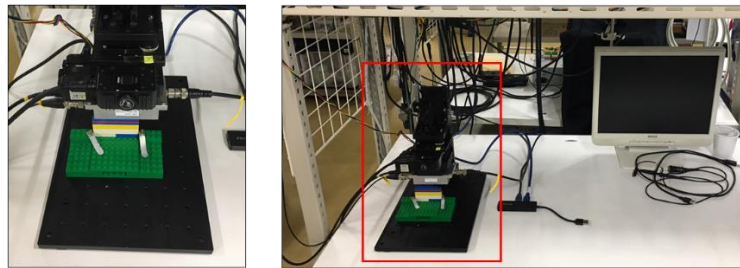


Figure 6.3. The system setup of the coating film monitoring.

6.1.2. Sample

The sample for the measurement is created from layer of several materials such as Acrylonitrile Butadiene Styrene (ABS) as the substrate and coated with several layers of acrylic with colors on it, as shown by Figure 6.4. The created sample imitates the coating layers used in the automotive industry.

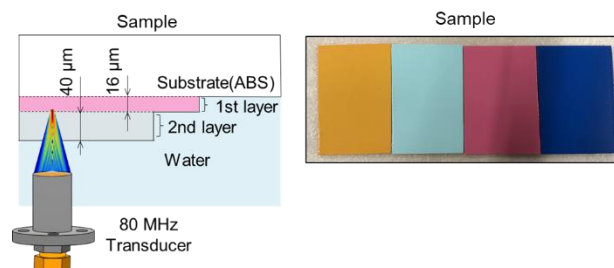


Figure 6.4. The created sample for the purpose of measurement.

The difference in impedance between each layer will create reflections that will be acquired by the transducer. The specification of the transducer is similar with that used in the skin observation (80 MHz focused transducer).

6.1.3. Dual domain deconvolution (coating film)

Since several peaks that comes from the interface between each layer are obtained during the measurement, the deconvolution process can then be performed. The deconvolution is necessary because sometimes the reflection coming from the interface of one layer is overlapped (natural convolution) with other reflections especially if the sample thickness is so thin. In addition, since the depth of the measurement area is deeper than that from the skin measurement, the baseline will be more likely to be unstable if the deconvolution process is carried out in frequency domain. In conjunction with that, the dual domain deconvolution method is proposed for deconvoluting the signal received from the coating layers. The reference signal for the calculation is taken from the interface between the substrate and the first layer and by using a specific window function the reflection from other interfaces is rejected.

In order to increase the quantitiveness of the result, each calculated reflection coefficient is converted into the distribution of acoustic impedance and by aligning all the calculated acoustic impedance waveforms, the 2D acoustic impedance mapping of each layer can be obtained.

6.1.4. The calculation of time-dependent reflection coefficient

The result of waveform after deconvolution process is shown by Figure 6.4. When the waveforms (target and reference) are deconvoluted by using conventional frequency domain deconvolution, the instability of the baseline appears in the result of the deconvoluted signal. This instability in the baseline will become stronger as the measurement area is deeper. In addition, the peaks that appears after deconvolution are still distorted by the instability of the baseline.

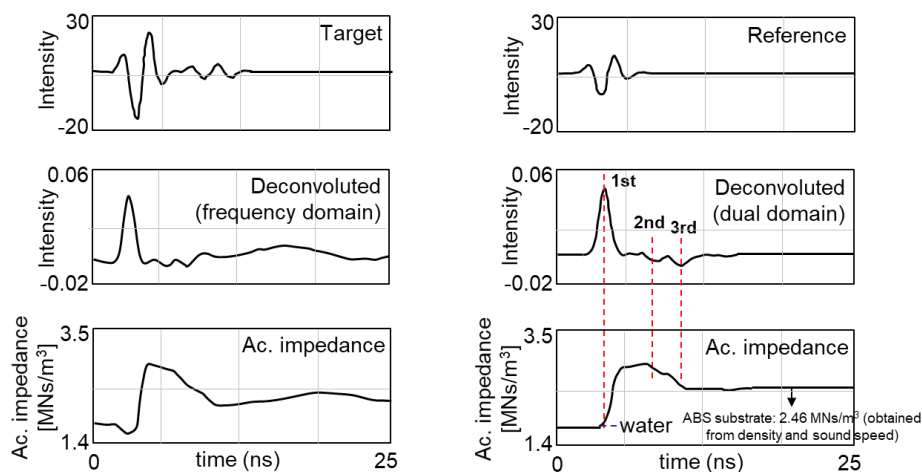


Figure 6.5. The time dependent reflection coefficient calculated by dual domain deconvolution.

When this wavy waveform is converted into the acoustic impedance distribution, the accumulation of error occurs during the integration process. This will lead to the resulting acoustic impedance distribution having an unreliable result (wavy).

On the other hand, the reflection coefficient calculated by the proposed dual domain deconvolution shows better result. Since the fluctuation in low frequency component is restored by the time domain calculation, the resulting waveform becomes free from the instability of the baseline. In addition, the peaks that comes from the reflection between interfaces of the layers can clearly be distinguished. The thickness of each layer can then be calculated by measuring the distance between these peaks. When the waveform is converted into the acoustic impedance, the distribution of acoustic impedance in each layer becomes clearly visible.

In this acoustic impedance calculation, the sound speed along the fragment is assumed to be uniform in all layers. This assumption may deform the scale of the calculated acoustic impedance image and needs to be revised in the future, however, at this moment, this assumption is considered to be acceptable.

6.1.5. The deconvoluted waveform and layers distribution

Figure 6.6 shows the result when all the waveforms along the scan direction is converted into the distribution of acoustic impedance. By looking at the B-mode image, the border between each layer is almost undistinguishable, this is because the reflection that comes from the interfaces of the layers is overlapped with the components from the system transfer function.

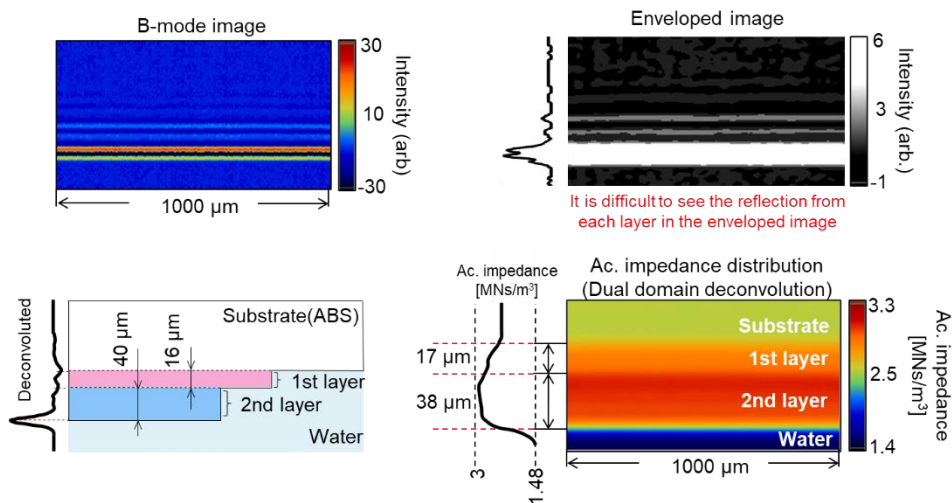


Figure 6.6. The calculated 2D acoustic impedance image of the layers.

The distribution of acoustic impedance in the result of frequency domain deconvolution is almost unreliable, mainly because the distribution of acoustic impedance of each layer cannot be distinguished, which may be caused by the improper deconvolution that leads to the accumulation of error during acoustic impedance conversion. On the other hand, in the result of dual domain deconvolution, the distribution of acoustic impedance in each layer is visible and well distributed.

6.1.6. Discussion

During the interpretation into the acoustic impedance distribution, the sound speed of each layer is assumed to be constant (uniform) in all along the fragments. This assumption may lead to the deformation in the scale of the calculated acoustic impedance image. However, since it will not affect the calculated acoustic impedance value of each layer and that the thickness parameter could directly be calculated from the deconvolution result, this condition is considered to be acceptable because at the moment, the goal is to quantify the result by calculating the acoustic impedance of each layer. It may be required to perform the acoustic impedance calculation by taking account the difference value of sound speed of the layers and this will be the continuation of this research in the future.

6.1.7. Conclusion

The application of dual domain deconvolution signal processing to evaluate the coating film which consists of several layers was performed. Since the observation depth is deeper than that from the skin observation, the baseline will likely be more unstable if the deconvolution process is carried out in the frequency domain, which will result in the accumulation of error when the waveform is integrated in order to calculate the acoustic impedance distribution. As a result, the waveform after the deconvolution by using dual domain can retain the stability of the baseline, resulting in the acoustic impedance distribution of each layer becomes visible. From this observation, two parameters of the coating film (sample) could be obtained: first is the thickness of each layer that can be calculated directly from the deconvolution result and the second is the uniformity of each layer that can be observed by means of their acoustic impedance distribution.

6.2. Space charge measurement by means of pulse electroacoustic (PEA) method

The proposed signal processing can also be applied to detect the existence of space charge in the XLPE cable. In the recent years, the technique to measure the space charge in the solid dielectric materials has been improved not only in terms of measurement technique but also in the way of data analysis. Such improvements will give a better understanding about the phenomena that occurs in the dielectrics in order to minimize the risk of breakdown in high voltage applications^{(68),(84)–86)}.

However, since a natural convolution occurs between the space charge that exists inside the insulation and the system transfer function, a reverse process in order to separate the space charge from the system transfer function or normally called deconvolution is required. Since the separation process is equal to the division in the frequency domain, the conventional deconvolution process is done thoroughly in frequency domain.

The PEA measurement was conducted with several level of high-DC voltage applied to the insulation. The lock-in calibration process is done by means of subtracting two signals, in order to calculate the initial space charge condition. There are two signals that are used as the input of the deconvolution process, target signal or the signal acquired from the insulation as it is and the reference signal that is obtained after the subtraction of the main signal.

In the conventional method to calculate the space charge distribution, both target and reference signals are brought into the frequency domain after being multiplied by a proper window function. In some applications, the spectrum of the window function especially on its low-frequency part will disturb the low-frequency of the main signal. The target signal is then divided by the reference signal and the output is directly converted back into the time domain by making use of the inverse Fourier transform.

However, since the target signal originally has a disturbed low-frequency component, the spectrum division in the frequency domain sometimes leads to the uncontrolled result, especially when the low-frequency components of the reference signal is really small. This will lead to a noisy waveform accompanied with a strong DC component in the form of a baseline if the result is brought back to the time domain.

In conjunction with that, another type of deconvolution that is performed in both time and frequency domain is proposed. The disturbed low-frequency components will be replaced with the ones from time-domain deconvolution by specifying a threshold value. The result is a signal that is free from the generation of unnecessary DC components.

As the stability of the waveform is improved, the distributions of charge and field intensity, and also potential can be calculated based on the deconvolution result. In addition, by scanning the cable (joint) the distribution of charge along the cable can be obtained.

6.2.1. System setup

Figure 6.7. illustrates the space charge measurement system on the cross-linked polyethylene (XLPE) cable by using the new proposed Pulses Electro-Acoustic (PEA) device which is able to capture the space charge signal on a 6 mm thick model cable with a good sensitivity^{(68), (84), (87), (88)}.

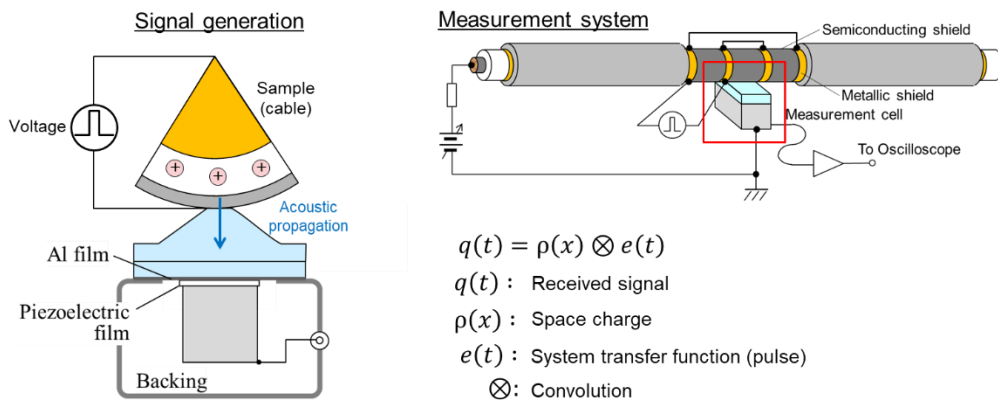


Figure 6.7. The measurement system and the PEA measurement cell.

The inner and outer radius of the cable are 27.5 mm and 47.5 mm, respectively. The DC voltage is applied with 4 μ s of sampling interval, where each waveform consists of 500 samples. The space charge signal acquired from the DC 10 kV is used as subtractor in the lock-in calibration process. The resulting signal is then used as the reference signal for the deconvolution process.

6.2.2. Acquired signal

The stream of the signal processing begins with the target signal or the signal acquired from the 40 kV and 50 kV of applied DC voltage, whereas the reference signal is obtained after subtracting the target signals with the 10 kV signal as the assumption of initial space charge condition, this process is called lock-in calibration process. After the signal is subtracted, the waveform is convolved with a time-domain Tukey window. During this process, only the first peak of the signal is used while the rest of the signal samples are set to zero with a small amount of noise because the original waveform contains a low amount of noise.

6.2.3. Dual domain deconvolution (space charge measurement by PEA)

In order to be able to evaluate the charge distribution inside the cable, the dual domain deconvolution is proposed to obtain the reflection coefficient containing space charge. In addition, since the deconvoluted waveform will be utilized as a parameter to calculate the charge distribution, the stability of the waveform especially baseline needs to be maintained, because the calculation for calculating the charge distribution is similar to the integration along the time axis and any instability in the deconvoluted waveform will lead to the accumulation of error. The stream and the sequence of the dual domain deconvolution is similar as previously described in the previous chapter.

6.2.4. The result of time dependent reflection coefficient by dual domain deconvolution

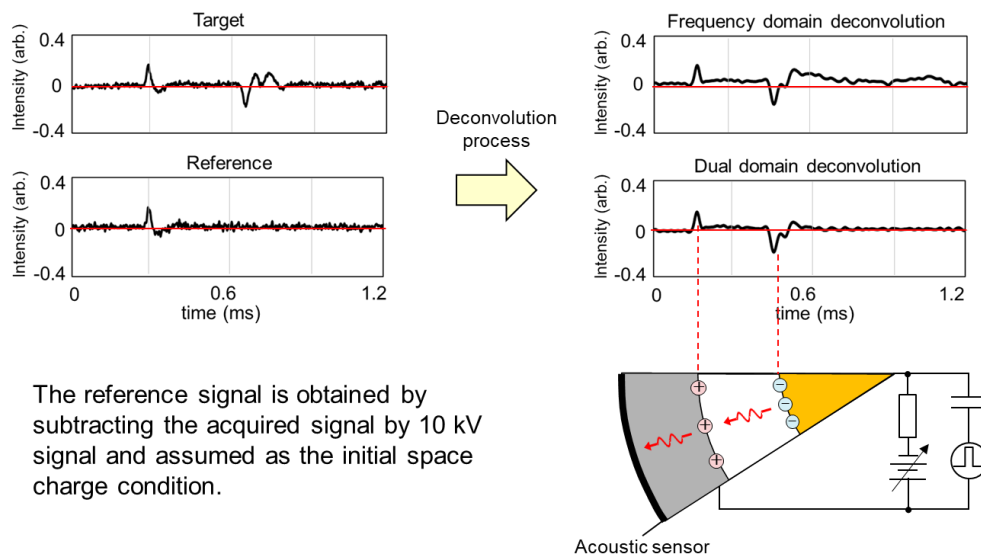


Figure 6.8. The comparison of the calculated time dependent reflection coefficient.

Figure 6.8 shows the result of the proposed time and frequency deconvolution method after being applied to the 40 kV and 50 kV space charge signal. As shown in the figure, on the 50 kV result, a slope appears on the second peak of the full frequency domain deconvolution result. The

baseline is also wavy and some offset exist in the waveform. Unlike the frequency domain deconvolution, the waveform generated by the time-frequency domain deconvolution method is free from unnecessary DC components. The shape of the waveform is also clear and flat.

As the voltage applied to the cable is smaller, that is 40 kV, the baseline that distorts the waveform is also stronger, as shown by the result calculated by using frequency domain deconvolution. This appearance of baseline will lead to the misinterpretation when evaluating the existence of space charge in the deconvoluted signal because the unstable baseline in the signal appears as if space charge signal exists in the waveform. On the other hand, the dual domain deconvolution could still retain the stability of the waveform, as shown by baseline in the deconvoluted waveform which remains stable even when smaller voltage is applied to the cable.

6.2.5. 2D charge distribution along the cable

When the stability of the deconvoluted waveform was successfully retained, the distribution of charge along the cable can be obtained by performing a scanning process along the length of the cable. Figure 6.9 shows the result of charge distribution at cable joint. The response is obtained by scanning the cable by using array scanner device⁶⁹.

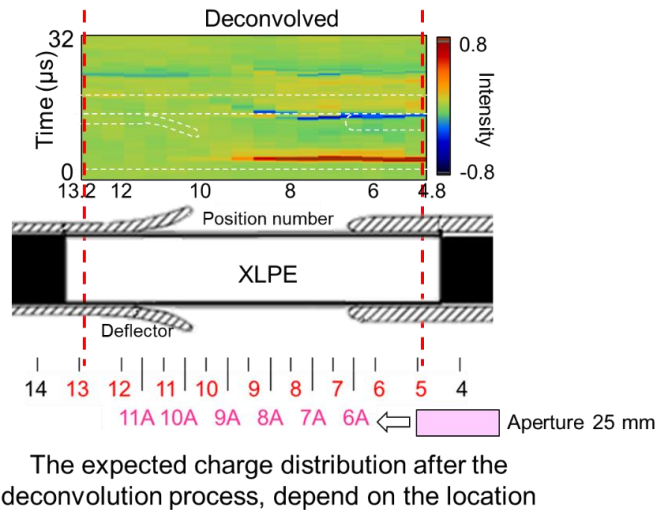


Figure 6.9. The comparison of the calculated time dependent reflection coefficient.

From this result, it can be concluded that the proposed method can be extended to two-dimensional observation, in terms of space charge measurement by using the newly created PEA device.

6.2.6. Field analysis

Figure 6.10 shows the result of the distribution of charge intensity, electric field and potential calculated from the 50 kV result of time and frequency deconvolution after some adjustment. In this particular case, there was no significant space charge, as shown by Figure 6.10,

However, by using the new PEA device^(67),68), even with a small voltage, a good proportion of waveform could be acquired.

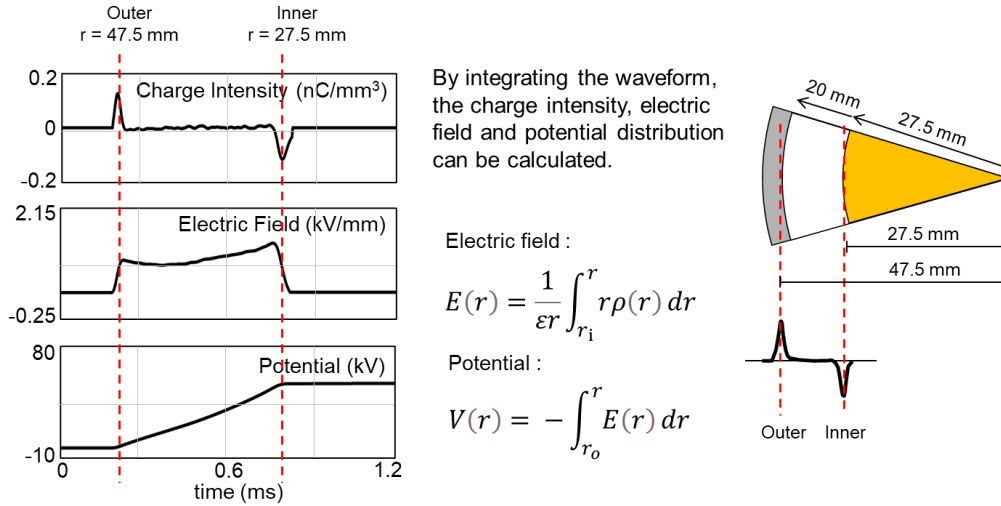


Figure 6. 10. The field calculated by using the result of the proposed method.

6.2.7. Discussion

By examining the deconvoluted result, it shows that good proportion of signal could be obtained even when the applied voltage was small (around 50 kV). This may suggest that the newly created PEA device could acquire a signal with good proportion. In addition, by combining it with the analysis by using dual domain deconvolution, the distribution of charge and also field distribution could be calculated.

6.2.8. Conclusion

The deconvolution process in both time and frequency domain for space charge signals are proposed. By using the new created PEA device, even with low voltage applied in the system, a good waveform could still be acquired. The reference signal is obtained by subtracting the acquired signal by 10 kV signal. The result shows that the distribution of space charge calculated by the proposed time and frequency domain deconvolution method could maintain the proportion such as the shape and the trend of the waveform while the waveform itself is free from unnecessary low-frequency DC components, compared with the result of the full frequency domain deconvolution with its deficiency in terms of maintaining the low-frequency components that is disturbed after an improper division in frequency domain. In addition, by scanning the cable using the PEA array scanner, the distribution of charge along the cable could be obtained. This may suggest that the time-frequency deconvolution method is quite robust and suitable to be applied to the cable measurement. Since a good waveform is obtained by the proposed method, the distribution of charge intensity, electric field and potential could be calculated.

Chapter VII

Conclusion and Future Applications

The application of the proposed signal processing to several field of ultrasound-related study had previously described in the previous chapter of this thesis and as much as four achievements had been achieved. This chapter of study will describe about the conclusion of each achievement, which is as follow:

7.1. Conclusion

7.1.1. Acoustic impedance mapping for human cheek skin observation

The first achievement of this study was previously described in chapter III. We proposed the application of deconvolution performed in both time and frequency (dual) domain in order to reconstruct the reflection coefficient that comes from the skin because normally, the acquired signal contains reflection from the target and the system transfer function that are convoluted naturally. The conventional frequency domain deconvolution will lead to the instability in the baseline of the signal because of the improper spectral division that will distort the low frequency part of the resulting spectrum. By using the proposed method, this distorted spectrum will be replaced by that calculated from time domain deconvolution. However, since the calculation speed of time domain deconvolution is directly proportional to the number of samples in the signal, down-sampling operation is performed, which will result in the reduction of high frequency components in the signal. By specifying a threshold value, the result of time domain deconvolution is combined with that from frequency deconvolution, resulting in a signal with maintained both low and high frequency components. In terms of human cheek skin observation, the following is the result of the achievements:

1. We proposed the human cheek skin observation by means of acoustic impedance microscope. Since the human cheek skin consists of several layers along the depth direction, performing assessment based on the cross-sectional (B-mode) view will provide more information related to the skin properties. In addition, by using the proposed acoustic impedance microscope, a non-invasive (living) skin observation could be performed, without the need to slice the specimen.
2. Deconvolution process is essential because the reflection that comes from the skin is overlapped (convoluted) naturally with the components from the system transfer function. By utilizing the proposed dual domain deconvolution method, a good proportion of signal with stable baseline could successfully be obtained, representing the reflection coefficient from the human cheek skin.
3. Unlike the conventional B-mode imaging, the result is quantified by converting each calculated reflection coefficient into the distribution of acoustic impedance. This will add

more information to the skin evaluation because now each layer of the skin is contrasted by elastic parameters (acoustic impedance), which related to the elasticity.

4. After calculating all the cross-sectional acoustic impedance images, the 3D reconstruction of skin layers could successfully be performed. Moreover, by observing the distribution of acoustic impedance in the layers of the skin, the correlation between ages (young and old) and the generation process of wrinkles (wrinkle parameters) could be calculated.

7.1.2. Optimal condition for dual domain calculation (speed and preciseness improvement) applied to human skin observation

The second achievement of this study was previously described in chapter IV. Since a single cross-sectional acoustic impedance view of the skin was successfully obtained, the requirement increases from 2D to 3D skin analysis. This is because human skin is wide and its surface is not uniform, so a single cross-sectional acoustic impedance image will not provide sufficient information. In addition, performing 3D calculation will increase our freedom to observe the skin from all cross-sectional directions. In conjunction with that, the optimal condition of dual domain deconvolution for calculating all cross-sectional slices in the scan direction was performed in order to increase the speed and preciseness of the calculation. The optimal condition includes the discussion about reduction of samples by down-sampling; the addition of DC offset in the transfer matrix during time domain calculation; and the frequency border between two domains. The achievements are as follows:

1. The optimal condition for dual domain deconvolution had been performed, which means that the stability and preciseness of the calculation when generating all cross-sectional slices was also improved and that calculation could be made as efficient as possible.
2. Since the stack of cross-sectional acoustic impedance images had been obtained, various quantitative skin analysis can be performed, such as the change of acoustic impedance and its correlation with ages (young, old); the generation of wrinkles in the layers of the skin; and the effect of applying some cosmetics to the layers of the skin in order to prevent aging can all be performed. These attempts can be useful for cosmetics manufacturer in order to produce the most suitable skin product for different skin condition, because the observation is non-invasive and does not require much time.

7.1.3. Precise cellular-sized observation by acoustic impedance microscope

The third achievement of this study was described previously in chapter V. Biological cell observation by using ultrasound microscope was carried out. Since the cultured cell is very thin, the number of cross-sectional cell observation-related research by means of acoustic microscope was still very limited. Even if B-mode view of the cell is available, it still does not represent any useful meaning because the displayed RF signal still contains the components from a system transfer function and still not quantitative. In conjunction with that, the signal processing for cultured cell analysis was performed. The target signal was deconvoluted by using reference signal (water) in order to reconstruct the reflection coefficient from the interface of cell. However, since frequency domain deconvolution would cause instability in the deconvoluted waveform (similar to skin observation), the dual domain deconvolution is then proposed. Since the baseline

in the deconvoluted waveform could be stabilized, each reflection coefficient is then quantified by converting it into the distribution of acoustic impedance. After the analysis, several achievements could be achieved, which are as follows:

1. We proposed acoustic impedance microscope which enable us to perform a cultured cell observation without introducing any contaminants and in addition, the living observation of cell can be performed. This will enable us to see and track some changes (stages) in the property of cell after some treatment is done, such as addition of medicine, etc.
2. Since a cross-sectional view of the cell was successfully produced, some parts of the cell such as nucleus, cytoskeleton and also their position and size along the beam direction could be estimated. In addition, since the image is contrasted by acoustic parameters such as acoustic impedance which is related to the elasticity, more quantitative result could be obtained.
3. After the 3D observation was done by calculating all the cross-sectional slices along the scan direction, the flexibility of the calculation increased because now the cell can be observed by slicing it from all cross-sectional direction. The position of the cell in the three-dimensional plane could also be observed.
4. After the stability of each calculated cross-sectional slices were retained, the change in the morphology of the cell such as height and shape after a specific treatment was done such as fixation could be assessed and reconstructed in 2D view, which will provide us a more interactive way to assess the dynamism of the biological cell.

7.1.4. The application of the proposed signal processing to other ultrasound-based measurements (industrial applications)

Other than biological and medical field, the application of ultrasound microscope combined with the proposed signal processing technique can broadly applied to other ultrasound-based measurement field such as coating film monitoring and the evaluation of space charge in the XLPE cable by using pulse electroacoustic device. This is because these applications required an integration process along the time axis after the deconvolution process in order to quantify the result. In addition, in one of the applications (space charge in the cable), the observation ranges are much deeper than previously described application (skin and cell), which means that the instability of the baseline will become stronger. In order to deal with that, the dual domain deconvolution is performed to each signal and the result is then quantified by deeper calculation. From these applications, several achievements could successfully be achieved, which are as described below:

7.1.5. Coating film monitoring

1. We proposed a measurement method to evaluate the layers in the coating film similar to the one utilized in the automotive industry. Since the coating film consists of several layers with different thickness and material properties, assessing them by means of ultrasound microscope will provide us a cheaper and more quantitative result because the way of observation is similar to the conventional method by using high intensity (Terahertz) light (laser). However, the conventional observation tends to be expensive because a high intensity

laser is utilized in the system. Our proposed method can then be a cheaper (but quantitative) alternative for coating film evaluation.

2. After the deconvolution, the peaks from all interface of the layers became visible, the thickness could then be calculated by measuring the distance of each peak.
3. The uniformity distribution of each layer in the coating film could also be assessed by looking at the generated reflection coefficient image (after deconvolution).
4. Moreover, by converting each reflection coefficient into the acoustic impedance distribution, each property of the layers could then be assessed by means of their acoustic properties, which is more quantitative than a normal B-mode image acquired by the conventional measurement.

7.1.6. Space charge measurement by means of pulse electroacoustic (PEA) method

1. By utilizing the pulse electroacoustic (PEA) device, the signal acquired from the XLPE cable was successfully obtained. A deconvolution is then performed in order to reconstruct the space charge distribution because normally the space charge signal is convoluted naturally with the transfer function of the system. Misinterpretation may occur if frequency domain deconvolution is performed, because an instable baseline may appear as if space charge exists in the cable. In conjunction with that, the deconvolution by dual domain was performed because it will retain the stability of the baseline because the observation target (cable) is deeper than that in biological observation.
2. When the stability of the baseline in the signal is maintained, the distribution of charge intensity, electric field and potential could then be calculated. In addition, by scanning the cable, two-dimensional map of the charge distribution along the cable could be obtained which will provide us much information about the space charge phenomenon inside the cable.

7.2. Future application

Figure 7.1. shows the target of acoustic property imaging that has been proposed in this study and also the plan for future application, in both biological and industrial field. Starting from cultured cell observation as the smallest target (Glial cell and Fibroblast cell), the 3D acoustic property imaging of single cell had been carried out. Since each image was contrasted by elastic parameter (acoustic impedance), the change in cell acoustic property after addition of drug (which is corresponded to the dynamism of the cell) that cannot be seen under the light microscope could be observed. As for the future application, the observation will be expanded to the group of cells (colonized cells) in order to assess more parameters about cultured cell such as the interaction of one cell with another.

As for the human skin observation, by observing the generated 3D cross-sectional acoustic impedance image of the skin, the acoustic property of skin layer such as horny layer and papillary layer could be assessed. In addition, the generation process of wrinkle in the skin layer and its correlation to ages could also be monitored. As the quantitiveness will reduce when the target gets deeper, at this moment (as this thesis book is written), only some parts of skin layers that can quantitatively be observed such as horny and papillary layer and little part of dermis. For future

applications, our plan is to perform an assessment of deeper part of human skin (especially in dermis area). This needs to be followed by robust error correction and some modifications in terms of hardware.

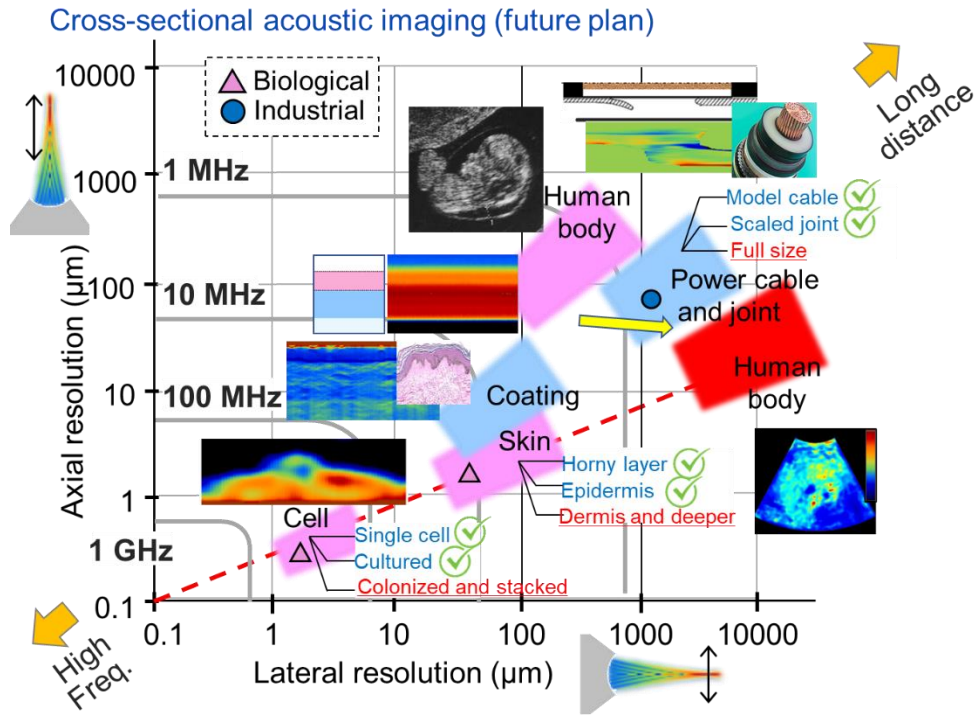


Figure 7.1. The achieved and the future plan of the quantitative acoustic imaging applications^{89),90)}.

In power cable measurement, the space charge distribution in model cable (XLPE) and scaled joint cable could successfully be calculated. As for the future plan, the observation of full-size cable will be carried out in order to assess the space charge distribution under the actual condition.

In addition of the already mentioned measurement target above, we also plan to carry out an observation of human body. Since the previous target (cell and skin) shows an improvement in both quantitiveness and axial resolution after signal processing, we believe that human skin observation is also possible to be performed. However, since human skin is much deeper than cell or skin, it will become more challenging to maintain the stability of the baseline as well as minimize the error of calculation when the target gets deeper. However, since lower frequency of ultrasound is used, we may have a benefit because the hardware of the measurement will not be as complicated as those observation for thin object (such as cell).

References

1. P. G. Newman, G. S. Rozycki, “The History of Ultrasound”, *Surgical Clinic of North America*, 78, pp. 179 – 195 (1998).
2. H. Azhari, “Basics of Biomedical Ultrasound for Engineers”, John Wiley & Sons, Inc., Hoboken, NJ, USA, pp. 1 – 7 (2010).
3. Y. Saijo, “Acoustic Microscopy: Latest Developments and Applications”, *Imaging Med*, pp. 47 – 63 (2009).
4. IEEE International Committee on Electromagnetic Safety “IEEE Standard for Safety Levels with Respect to Human Exposure to Radio Frequency Electromagnetic Fields, 3 kHz to 300 GHz”, International Committee on Electromagnetic Safety (IEEE) (2006).
5. L. V. Titova, A. K. Ayesheshim, A. Golubov, D. Fogen, R. Rodriguez-Juarez, F. A. Hegmann and O. Kovalchuk, “Intense THz pulses cause H2AX phosphorylation and activate DNA damage response in human skin tissue”, *Biomed. Opt. Express*, 4, pp. 559 – 568 (2013).
6. S. Semenov, “Microwave tomography: review of the progress towards clinical applications”, *Philosophical Transactions of the Royal Society A*, pp. 3021 – 3042 (2009).
7. M. A. Haidekker, “Medical Imaging Technology”, *Springer Briefs in Physics*, pp. 13 – 25 (2013)
8. D. N. White, “Neurosonology Pioneers” *Ultrasound in Medical and Biology*, 14, pp. 541 – 561 (1988).
9. J. M. Reid, “Diagnostic Applications of Ultrasound”, *Proceedings of the IRE*, 47, pp. 1963 – 1967 (1959).
10. J. Mamou, M. L. Oelze, “Quantitative Ultrasound in Soft Tissues”, *Springer Netherlands, Dordrecht*, pp. 291 – 315 (2013).
11. X-Ray Radiology, Pixabay, URL: <https://pixabay.com/photos/xray-x-ray-radiology-scan-4832140/> (accessed on January, 2021).
12. What’s the Difference Between Simple and Compound Microscopes, URL: <https://www.pathwooded.com/post/whats-the-difference-between-simple-and-compound-microscopes> (accessed on January, 2021).
13. Terahertz Imaging and Sources, URL: <https://www.nist.gov/programs-projects/terahertz-imaging-and-sources> (accessed on January, 2021).
14. Microwave Imaging System, URL: <https://allwave.site/products/microwave-imaging-systems/#1540231915510-65d20436-1f92> (accessed on January, 2021).
15. Wikipedia, Ultrasound, URL: <https://en.wikipedia.org/wiki/Ultrasound> (accessed on January, 2021).
16. D. Zimmerman, “‘A more creditable way’: The discovery of active sonar, the Langevin–Chilowsky patent dispute and the Royal Commission on Awards to Inventors”, *War in History*, pp. 1 – 22 (2018).
17. W. D. Hackmann, “Sonar Research and Naval Warfare 1914-1954: A Case Study of a Twentieth-century Establishment Science”, *University of California Press, Historical Studies*, 83, pp. 83 – 110 (2011).

18. C. C. Beuglet, R. A. Beique, “Continuous Ultrasound B-Scanning of Palpable Breast Masses”, *Radiology*, pp. 123 – 128 (1975).
19. B. D. Doust and N. F. Maklad, “Ultrasonic B-Mode Examination of the Gallbladder”, *Radiology*, pp. 643 – 647 (1974).
20. R. O. Friday, P. Barriga, A. B. Crummy, “Detection and Localization of Intra-abdominal Abscesses by Diagnostic Ultrasound”, *Archives of Surgery*, 110, pp. 335 – 337 (1975).
21. G. R. Leopold and J. Sokoloff, “Ultrasonic Scanning in the Diagnosis of Biliary Disease”, *Surgical Clinic of North America*, 53, pp. 1043 – 1052 (1973).
22. Y. Saijo, N. Hozumi, K. Kobayashi, N. Okada, T. Ishiguro, Y. Hagiwara, E. Dos Santos Filho, T. Yambe, “Ultrasound Speed and Impedance Microscopy for in vivo Imaging”, *Annual International Conference of IEEE Engineering in Medical and Biology – Proceedings*, pp. 1350 – 1353 (2007).
23. K. Miura, K. Yamashita, “Evaluation of aging, diabetes mellitus, and skin wounds by scanning acoustic microscopy with protease digestion”, *Pathobiology of Aging and Age-related Diseases*, 8, pp. 1 – 12 (2018).
24. N. Hozumi, S. Kajima, A. I. Gunawan, S. Yoshida, K. Kobayashi, Y. Saijo, S. Yamamoto, “Viscoelastic Imaging Using Acoustic Impedance Microscope and Its Application to Biological Tissue”, *IEEE International Ultrasonics Symposium (IUS)*, pp. 1 – 4 (2015).
25. A. I. Gunawan, Y. Saijo, N. Hozumi, S. Yoshida, K. Kobayashi, S. Yamamoto, “Acoustic Impedance Estimation Using Calibration Curve for Scanning Acoustic Impedance Microscope” *IEEE International Conference on Knowledge Creation and Intelligent Computing (KCIC)*, pp. 240 – 245 (2016).
26. H. Okawai, M. Tanaka, N. Chubachi and J. Kushibiki, “Non-contact Simultaneous Measurement of Thickness and Acoustic Properties of a Biological Tissue Using Focused Wave in a Scanning Acoustic Microscope”, *Japanese Journal of Applied Physics*, 26, pp. 52 – 54 (1987).
27. N. Hozumi, R. Yamashita, C. K. Lee, M. Nagao, K. Kobayashi, Y. Saijo, M. Tanaka, N. Tanaka, S. Ohtsuki, “Time–frequency analysis for pulse driven ultrasonic microscopy for biological tissue characterization”, *Ultrasonics*, 42, pp. 717 – 722 (2004).
28. Y. Saijo, H. Sasaki, T. Yambe, M. Tanaka, N. Hozumi, K. Kobayashi and N. Okada, “Speed of Sound Microscopy for Biomedical Applications”, *Proceedings of IEEE Ultrasonics Symposium*, pp. 419 – 422 (2005).
29. K. Takanashi, M. Washiya, K. Ota, S. Yoshida, N. Hozumi, K. Kobayashi, “Quantitative evaluation method for differentiation of C2C12 myoblasts by ultrasonic microscopy”, *Japanese Journal of Applied Physics*, 56, pp. 07JF11 - 07JF16 (2017).
30. T. T. K. Soon, T. W. Chean, H. Yamada, K. Takahashi, N. Hozumi, K. Kobayashi, S. Yoshida, “Effects of anticancer drugs on glia–glioma brain tumor model characterized by acoustic impedance microscopy”, *Japanese Journal of Applied Physics*, 56, pp. 07JF15-1 - 07JF15-5 (2017).
31. R. H. Rahayu, K. Takanashi, T. T. K. Soon, I. Seviaryna, R. Maev, K. Kobayashi, N. Hozumi, S. Yoshida, “Reaction assessment of cultured breast cancer cells exposed to anticancer agents using microscale acoustic impedance profile”, *Japanese Journal of Applied Physics*, 57, pp. 07LF26-1 - 07LF26-7 (2018).

32. T. Matsui, N. Hozumi, A. Otaka and T. Matsumoto, “Non-destructive fault localization of IC interconnection by using ultrasonic heating”, *Japanese Journal of Applied Physics*, pp. 07JC11-1 - 07JC11-6 (2018).
33. T. Matsumoto and N. Hozumi, “Resistance change observation of wiring in semiconductor device using ultrasonic stimulation”, *Proceedings of the International Symposium on the Physical and Failure Analysis of Integrated Circuits, IPFA*, pp. 1 – 5 (2017).
34. A. Korpel, L. W. Kessler, P. R. Palermo, “Acoustic Microscope operating at 100 MHz”, *Nature*, 232, pp. 110–111 (1971).
35. R. A. Lemons, C. F. Quate, “A Scanning Acoustic Microscope”, *Ultrasonics Symposium (IEEE)* pp. 18 – 21 (1973).
36. R. N. Johnston, A. Atalar, J. Heiserman, V. Jipson, C. F. Quate, “Acoustic microscopy: Resolution of subcellular detail”, *Proceedings of the National Academy of Sciences of the United States of America*, 76, pp. 3325 – 3329 (1979).
37. J. A. Hildebrand, D. Rugar, R. N. Johnston, C. F. Quate, “Acoustic microscopy of living cell”, *Proceedings of the National Academy of Sciences of the United States of America*, 78, pp. 1656 – 1660 (1981).
38. Y. Saijo, M. Tanaka, H. Okawai, F. Dunn, “The ultrasonic properties of Gastric Cancer Tissues Obtained with a Scanning Acoustic Microscope System”, *Ultrasound in Medicine and Biology*, 17, pp. 709 – 714 (1991).
39. N. Hozumi, A. Kimura, S. Terauchi, M. Nagao, S. Yoshida, K. Kobayashi, Y. Saijo, “Acoustic Impedance Micro-imaging for Biological Tissue Using a Focused Acoustic Pulse with a Frequency Range up to 100 MHz”, *Proceedings - IEEE Ultrasonics Symposium*, pp. 170 – 173 (2005).
40. K. Kobayashi, S. Yoshida, Y. Saijo, N. Hozumi, “Acoustic impedance microscopy for biological tissue characterization”, *Ultrasonics*, 54, pp. 1922 – 1928 (2014).
41. K. Takanashi, M. Washiya, K. Ota, S. Yoshida, N. Hozumi, K. Kobayashi, “Quantitative evaluation method for differentiation of C2C12 myoblasts by ultrasonic microscopy”, *Japanese Journal of Applied Physics*, 56, pp. 07JF11 - 07JF16 (2017).
42. N. Hozumi, N. Dalila Binti Jalaluddin, T. T. K. Soon, T. Kawashima, Y. Murakami, S. Yoshida, K. Kobayashi, “Three-dimensional Acoustic Impedance Imaging for Cultured Biological Cells”, *IEEE International Ultrasonics Symposium (IUS)*, pp. 1 – 9 (2018).
43. N. Hozumi, S. Yoshida, K. Kobayashi, “Three-dimensional acoustic impedance mapping of cultured biological cells”, *Ultrasonics*, 99, pp. 1 – 4 (2019).
44. J. E. Aldrich, “Basic physics of ultrasound imaging”, *Critical Care Medicine*, 35, pp. 131 – 137 (2007).
45. N. F. Law, R. G. Lane, “Blind deconvolution using least squares minimisation”, *Optics Communications, Elsevier*, 128, pp. 341 – 352 (1996).
46. K. Kamada, O. Oshiro, K. Chihara, W. Secomski, A. Nowicki, “Three-Dimensional (3D) High-Frequency Ultrasound Images of Skin and an Eye”, *Japanese Journal of Applied Physics, Part 1: Regular Papers and Short Notes and Review Papers*, 40, pp. 3931-3932 (2001).
47. Y. Takema, Y. Yorimoto, M. Kawai, G. Imokawa, “Age-related changes in the elastic properties and thickness of human facial skin”, *British Journal of Dermatology*, 131, pp. 641 – 648 (1994).

48. Y. Saijo, Y. Hagiwara, K. Kobayashi, N. Okada, A. Tanaka, N. Hozumi, T. Iwamoto, “Three-dimensional Ultrasound Imaging of Regenerated Skin with High Frequency Ultrasound”, 5th IEEE International Symposium on Biomedical Imaging: From Nano to Macro, pp. 1231-1234 (2008).
49. E. B. Prastika, A. Imori, T. Kawashima, Y. Murakami, S. Yoshida, N. Hozumi, R. Nagaoka, K. Kobayashi, “Acoustic impedance interpretation of cross-sectional human skin by using time and frequency domain deconvolution”, The 41th Symposium on Ultrasonic Electronics (USE 2020), 59, pp. SKKB06-1 - SKKB06-7 (2020).
50. Y. Saijo, K. Kobayashi, N. Hozumi, A. Tanaka, S. Sakai, “Visualization of Micro vessels in Skin by Three-Dimensional Ultrasound Microscope – Acoustical Imaging”, Springer, Dordrecht, 30, pp. 107 – 112 (2011).
51. T. Iwamoto, Y. Saijo, N. Hozumi, K. Kobayashi, N. Okada, A. Tanaka, M. Yoshizawa, “High Frequency Ultrasound Characterization of Artificial Skin”, Proceedings of the 30th Annual International Conference of the IEEE Engineering in Medicine and Biology Society, EMBS’08 - ‘Personalized Healthcare through Technology’, pp. 2185 – 2188 (2008).
52. Y. Birnbaum, H. Luo, M. C. Fishbein, B. Samuels, R. J. Siegel, “Documentation by Intravascular Ultrasound of Thrombus Overlying a Small Atheromatous Plaque in a Coronary Artery in Unstable Angina Pectoris and in Acute Myocardial Infarction”, The American Journal of Cardiology, 79, pp. 1568-1570 (1997).
53. E. de O. Barcaui, A. C. P. Carvalho, F. P. P. L. Lopes, J. Piñeiro-Maceira, C. B. Barcaui, “High frequency ultrasound with color Doppler in dermatology”, Anais Brasileiros de Dermatologia, 91, pp. 262 – 273 (2016).
54. Samsung Medison, Thyroid, mass, B and C - mode, URL: <https://www.medison.ru/ultrasound/gal323.htm>. (Accessed on February, 2021).
55. Ultrasonography, URL: <https://www.drshraddhathakur.com/ultrasonography/> (accessed on January, 2021).
56. A. Perperidis, D. Cusack, A. White, N. McDicken, T. MacGillivray, T. Anderson, “Dynamic Enhancement of B-Mode Cardiac Ultrasound Image Sequences, Ultrasound in Medicine and Biology, 43, pp. 1533 – 1548 (2017).
57. R. Dass, “Speckle Noise Reduction of Ultrasound Images Using BFO Cascaded with Wiener Filter and Discrete Wavelet Transform in Homomorphic Region”, Procedia Computer Science, 132, pp. 1543 – 1551 (2018).
58. E. Vicenzini, M. F. Giannoni, G. Sirimarco, M. C. Ricciardi, M. Toscano, G. L. Lenzi, V. Di Piero, “Imaging of Plaque Perfusion Using Contrast-Enhanced Ultrasound - Clinical significance”, Perspectives in Medicine, pp. 44 – 50 (2012).
59. J. Y. Lu, H. Zou, J. F. Greenleaf, “Biomedical ultrasound beam forming”, Ultrasound in Medicine and Biology, 20, pp. 403 – 428 (1994).
60. R. Nagaoka, S. Yoshizawa, S. I. Umemura, Y. Saijo, “Basic study of improvement of axial resolution and suppression of time side lobe by phase-corrected Wiener filtering in photoacoustic tomography”, Japanese Journal of Applied Physics, 57, pp. 07LD11-1 - 07LD11-7 (2018).
61. R. Nagaoka, K. Kobayashi, M. Arakawa, H. Hasegawa, Y. Saijo, “Correction of phase rotation in pulse spectrum method for scanning acoustic microscopy and its application to measurements of cells”, 99, pp. 1 – 12 (2019).

62. C. Yu, C. Zhang, L. Xie, “An envelope signal-based deconvolution algorithm for ultrasound imaging”, *Signal Processing* 92, pp. 793 – 800 (2012).
63. G. Matrone, A. Ramalli, P. Tortoli, “Ultrasound B - Mode Imaging: Beamforming and Image Formation Techniques”, *Applied Sciences*, 9, pp. 1 – 4 (2019).
64. M. S. Uddin, M. Tahtali, A. J. Lambert, M. R. Pickering, M. Marchese, I. Stuart, “Speckle-reduction algorithm for ultrasound images in complex wavelet domain using genetic algorithm-based mixture model”, *Applied Optics*, 55, pp. 4024 – 4035 (2016).
65. L. Demi, “Practical Guide to Ultrasound Beam Forming: Beam Pattern and Image Reconstruction Analysis”, *Applied Sciences*, 8, pp. 1 – 15 (2018).
66. X. Li, S. Zahra, T. Kawashima, Y. Murakami, N. Hozumi, “Lock-in Calibration for Space Charge Measurement”, *2020 IEEE 3rd International Conference on Dielectrics (ICD)*, p. 391 – 394 (2020).
67. E. B. Prastika, S. Zahra, X. Li, Y. Murakami, T. Kawashima, N. Hozumi, Y. Kim, “The application of signal processing using dual domain deconvolution for new space charge measurement method in HVDC full-size cables”, *Proceedings of the International Symposium on Electrical Insulating Materials*, pp. 277 – 280 (2020).
68. N. Hozumi, E. B. Prastika, S. Zahra, T. Kawashima and Y. Murakami, “Dual-domain Deconvolution Process Applied to Time-resolved Quantitative Dielectric Measurement”, *2020 IEEE 3rd International Conference on Dielectrics (ICD)*, pp. 347 – 350 (2020).
69. S. Zahra, M. Utagawa, T. Kawashima, Y. Murakami, N. Hozumi, P. Morshuis, Y. Cho, Y. Kim, “Two-dimensional space charge measurement of scaled cable joint model using scanning acoustic sensors and electrically insulating acoustic coupler”, *日誘電・絶縁材料/電線・ケーブル合同研究会*, pp. 13 – 16 (2021).
70. High Voltage Cable, URL: <https://global-sei.com/power-cable-business/> (2021).
71. T. W. Chean, N. Hozumi, S. Yoshida, K. Kobayashi, Y. Ogura, “Mutual conversion between B-mode image and acoustic impedance image”, *Japanese Journal of Applied Physics*, 56, 07JF18-1 - 07JF18-6 (2017).
72. E. B. Prastika, A. Imori, T. Kawashima, Y. Murakami, N. Hozumi, S. Yoshida, R. Nagaoka and K. Kobayashi, “Three-dimensional acoustic impedance mapping of human skin by improved time–frequency domain analysis”, *Japanese Journal of Applied Physics*, 60, pp. SDDE22-1 - SDDE22-12 (2021).
73. Y. Ogura, Y. Hara, M. Ninomiya, T. Yamashita, C. Katagiri, K. Kobayashi, Y. Shiihara, N. Hozumi, “Emergence of Eye Wrinkles Can Be Controlled by Balancing the Elasticity of the Stratum Corneum and the Dermis”, *The IFSCC Congress 2020 Yokohama*, pp. 1 – 10 (2020).
74. W. Montagna, A. M. Kligman, K. S. Carlisle, “Atlas of Normal Human Skin”, Springer New York, pp. 3 – 5 (1992).
75. Optical coherence tomography, URL: <https://dermnetnz.org/topics/optical-coherence-tomography> (accessed on January, 2021).
76. Cutometer® Dual MPA 580, URL: <https://www.enviroderm.co.uk/products/cutometer-dual-mpa-580> (accessed on January, 2021).
77. Cutometer® in general, URL: <https://www.courage-khazaka.de/en/16-wissenschaftliche-produkte/alle-produkte/178-cutometer-e> (accessed on January, 2021).

78. A. I. Gunawan, N. Hozumi, S. Yoshida, Y. Saijo, K. Kobayashi, S. Yamamoto, “Numerical analysis of ultrasound propagation and reflection intensity for biological acoustic impedance microscope”, *Ultrasonics*, 61, pp. 79 – 87 (2015).
79. R. Cheng, F. Zhang, M. Li, X. Wo, Y. W. Su, W. Wang, “Influence of Fixation and Permeabilization on the Mass Density of Single Cells: A Surface Plasmon Resonance Imaging Study”, *Frontiers in Chemistry*, 7, pp. 1 – 7 (2019).
80. F. Gruber, C. Kremslehner, L. Eckhart, E. Tschachler, “Cell aging and cellular senescence in skin aging - Recent advances in fibroblast and keratinocyte biology”, *Experimental Gerontology*, 180, pp. 1 – 13 (2020).
81. N. Hozumi, A. I. Gunawan, S. Kajima, S. Yoshida, Y. Saijo, K. Kobayashi, S. Yamamoto, “Sound field analysis for biological acoustic impedance microscope for its precise calibration”, *IEEE International Ultrasonics Symposium (IUS)*, pp. 1212 – 1215 (2013).
82. A. I. Gunawan, N. Hozumi, S. Yoshida, Y. Saijo, K. Kobayashi, S. Yamamoto, “Numerical analysis of acoustic impedance microscope utilizing acoustic lens transducer to examine cultured cells”, *Ultrasonics*, 61, pp. 102 – 110 (2015).
83. Q. Tang, J. Hu, T. Yu, “Electromagnetic evaluation of brick specimens using synthetic aperture radar imaging”, *NDT & E International*, 104, pp. 98 – 107 (2019).
84. Y. Li, M. Yasuda, T. Takada, “Pulsed Electroacoustic Method for Measurement Of Charge Accumulation In Solid Dielectrics”, *IEEE Transactions on Dielectrics and Electrical Insulation*, 1, pp. 188 – 195 (1994).
85. B. Vissouvanadin, C. Laurent, S. Le Roy, G. Teyssèdre, I. Denizet, M. Mammeri, B. Poisson, “A deconvolution technique for space charge recovery in lossy and dispersive dielectrics using PEA method”, *Annual Report - Conference on Electrical Insulation and Dielectric Phenomena, CEIDP*, pp. 10 – 13 (2010).
86. J. Castellon, S. Agnel, P. Notingher, “Review of space charge measurements in high voltage DC extruded cables by the thermal step method”, *IEEE Electrical Insulation Magazine*, 33, pp. 34 – 41 (2017).
87. B. Vissouvanadin, T. T. N. Vu, L. Berquez, S. Roy, G. Teyssèdre, C. Laurent, “Deconvolution techniques for space charge recovery using pulsed electroacoustic method in coaxial geometry”, *IEEE Transactions on Dielectrics and Electrical Insulation*, 21, pp. 821-828 (2014).
88. N. Hozumi, R. Yamashita, C. K. Lee, M. Nagao, K. Kobayashi, Y. Saijo, M. Tanaka, N. Tanaka, S. Ohtsuki, “Ultrasonic sound speed microscope for biological tissue characterization driven by nanosecond pulse”, 24, pp. 386-390 (2003).
89. Two- and three-dimensional sonography in early diagnosis of limb-body wall complex, URL: <https://sonoworld.com/fetus/page.aspx?id=1966> (accessed on January, 2021).
90. THED research, URL: <https://www.thelastography.com/functions> (accessed on January, 2021).

Acknowledgements

Alhamdulillah. To Allah, my savior, for being the only light during my dreary days. And also, I would like to express my special gratitude to:

Professor Naohiro Hozumi

For being such a lovely supervisor, and also for the unstoppable support, advice, help and kindness during these three years.

Professor Hirofumi Takikawa, Professor Kazuaki Sawada and Associate Professor Yoshinobu Murakami

For the encouraging comments and advice especially during my first and second doctoral defense.

Dr. Kazuto Kobayashi

For the chance and help so I could finally learn so many things related to the hardware behind the ultrasound measurement.

Dr. Sachiko Yoshida

For the continuous supply of cell samples during my experiments. Studying about living organism is always hard, but you could always have the best way to make me understand every single part of them.

Dr. Ryo Nagaoka

For the contribution and help on my research, especially during my first publication.

Honda Electronics' Team

Especially to Hitoshi Arai-san, Nagaya-Okada-san, Yuki-Kawaguchi-san and Hayato Akiyama-san. We are family. Let us always do our best in the future.

Mom and Dad

For the unstoppable love and everything.

Nathan Kevin

If I could go by a time machine and tell you what I have achieved now, I would not wish for anything else anymore.

Hideyuki Takahagi

For saying "Lets go Karaoke" whenever I felt like having a bad day.

Dr. Kazuki Tamura and Dr. Kazuyo Ito

For the sweet support and help right at the moment when I needed it the most.

Dr. Yuki Ogura from Shiseido

For the research collaboration with our laboratory. And also, for the discussion related to human skin measurement.

Kyoichi Takanashi

For saying "Your Kansai dialect is good" (though I know it is a joke).

Dr. Tomohiro Kawashima and Hozumi Laboratory Members

*Especially for ultrasound team (both skin and cell division: Mai, Isobe and Shintani),
Takeda (Kazama-kun) and Li, fighting!*

Takuto Matsui and Mom

*They said that Japan's winter is cold, but somehow you guys made it warm (December
2018 was great).*

Thank you.

List of publications

Journals

- [1] **E. B. Prastika**, A. Imori, T. Kawashima, Y. Murakami, N. Hozumi, S. Yoshida, R. Nagaoka and K. Kobayashi, “Acoustic impedance interpretation of cross-sectional human skin by using time and frequency domain deconvolution”, Jpn. J. Appl. Phys. 59 [SK], SKKB06, 7 pages (2020).
- [2] **E. B. Prastika**, A. Imori, T. Kawashima, Y. Murakami, N. Hozumi, S. Yoshida, R. Nagaoka and K. Kobayashi, “Three-dimensional acoustic impedance mapping of human skin by improved time-frequency domain analysis”, Jpn. J. Appl. Phys. 60 [SD], SDDE22, 12 pages (2021).
- [3] **E. B. Prastika**, T. Shintani, T. Kawashima, Y. Murakami, N. Hozumi, T. T. Kwong Soon, S. Yoshida, R. Nagaoka, and K. Kobayashi, “Time and frequency domain deconvolution for cross-sectional cultured cell observation by using an acoustic impedance microscope”, Ultrasonics [*under review*].

International Conferences

- [1] **E. B. Prastika**, S. Zahra, X. Li, Y. Murakami, T. Kawashima, N. Hozumi, Y. Kim “The Application of Signal Processing Using Dual Domain Deconvolution for New Space Charge Measurement Method in HVDC Full-Size Cables” 9th International Symposium on Electrical Insulating Materials (ISEIM), VA-5, pp.277-280 (2020).
- [2] N. Hozumi, **E. B. Prastika**, S. Zahra, T. Kawashima, Y. Murakami “Dual-domain Deconvolution Process Applied to Time-resolved Quantitative Dielectric Measurement”, IEEE 3rd International Conference on Dielectrics (ICD), pp.347-350 (2020).

Awards

- [1] Best paper award of 2019 Ultrasonic Symposium (USE 2019), “Acoustic impedance interpretation of cross-sectional human skin by using time and frequency domain deconvolution”, Jpn. J. Appl. Phys. 59 [SK], SKKB06, 7 pages (2020).

Local Conferences

- [1] **Edo Bagus Prastika**, 新谷太地, 川島朋裕, 村上義信, 吉田祥子, 穂積直裕, 小林和人, 超音波顕微鏡を用いた細胞内音響インピーダンスマッピング, 日本超音波医学会第93回学術集会, [3-10(d)-1] (2020).
- [2] 居森厚志, **Edo Bagus Prastika**, 小柴大雅, 川島朋裕, 村上義信, 吉田祥子, 穂積直裕, 小林和人, 超音波顕微鏡を用いた皮膚内部の音響インピーダンス解析の改善, 令和二年電気学会全国大会, 1-051, p. 64 (2020).

- [3] 居森厚志, **Edo Bagus Prastika**, 川島朋裕, 村上義信, 吉田祥子, 穂積直裕, 小林和人, 音響インピーダンスによる色素性母斑の定量観察, 令和 2 年度電気・電子・情報関係学会東海支部連合大会, pp. 16-4 (2020).
- [4] 居森厚志, **Edo Bagus Prastika**, 村上 舞, 川島朋裕, 吉田祥子, 穂積直裕, 長岡 亮, 小林和人, 時間周波数複合領域逆量込を利用した皮膚断層音響インピーダンスマイクロイメージング, 電子情報通信研究会超音波研究, US2020-44, pp. 7-11 (2020).
- [5] 新谷太地, **Edo Bagus Prastika**, 川島朋裕, 村上義信, 吉田祥子, 穂積直裕, 小林和人, 超音波顕微鏡による生体細胞の音響インピーダンス解析の改善, 令和二年電気学会全国大会, 1-050, p. 63 (2020).